FREIE UNIVERSITÄT BERLIN

FACHBEREICH MATHEMATIK UND INFORMATIK

On the Electronic Structure of Nanodiamonds for Photocatalysis

Autor:

Thorren Kirschbaum

Betreuer:

Prof. Dr. Frank Noé

Inaugural-Dissertation

zur Erlangung des akademischen Grades

Doctor rerum naturalium

Berlin, 2023

Statutory Declaration

I declare to the Freie Universität Berlin that I have written this dissertation independently and without the use of any sources or aids other than those indicated. This thesis is free of plagiarism. All statements that are taken verbatim or in content from other writings are marked as such. This dissertation has not been submitted in the same or a similar form in any previous dissertation procedure. The dissertation may be analyzed for plagiarism using suitable software programs in compliance with data protection regulations.

_____

Thorren Kirschbaum

Abstract

Nanodiamond photocatalysis has the potential to replace a range of high-energy industrial processes and provide a green alternative for energy harvesting and the production of chemical feedstocks. This thesis investigates the properties and characteristics of nanodiamonds in the context of photocatalysis with a focus on their diverse electronic structures.

First, we characterize a sample of fluorinated nanodiamonds from hydrogen fluoride synthesis via soft X-ray spectroscopy. X-ray photoelectron spectroscopy reveals a fluorine coverage of about 50 % on the nanodiamonds. The analysis is complemented by X-ray absorption spectroscopy (XAS) and resonant inelastic X-ray scattering spectroscopy (RIXS) experiments and supported by theoretical investigations of the underlying systems. The observed XAS and RIXS signatures are verified and explained by the quantum chemical calculations which show that the XAS signals systematically shift upon increasing the surface fluorine content. On the other hand, the same F K-edge RIXS signature is found for a broad range of fluorinated hydrocarbons, with the main signal originating from a selective excitation of the F 1s electron into an antibonding C-F σ^* orbital in all cases.

Furthermore, we investigate the interaction of nanodiamonds with adsorbates in aqueous dispersion, with a focus on charge transfer doping towards oxidative adsorbates. The observed charge transfer is found to increase with the adsorbates' standard reaction potentials in water and can further be tuned by modifying the nanodiamonds' highest occupied molecular orbital energies. The nanodiamond charge transfer excited states are similarly influenced by aqueous oxidative adsorbates, which capture a large fraction of the excited electrons. Nanodiamond cluster formation results in lowering of their optical gaps and preserves the atomic orbital-like shapes in the clusters' lowest unoccupied orbitals.

Finally, we introduce the ND5k data set which consists of 5,089 structures and frontier orbital energies of nanodiamonds. Based on this data, we suggest to consider the use of phosphorous-doped nanodiamonds for sunlight-driven photocatalysis. Furthermore, modern machine learning algorithms are evaluated for molecular property prediction of the ND5k structures. In this context, we propose an extension of graph neural networks using a set of tailored atomic descriptors which we test for the enn-s2s network architecture. The best results are obtained using the PaiNN graph neural network, the second best from our modified enn-s2s variant.

Overall, this work contributes to a better understanding of the electronic structures of nanodiamonds to aid future research in nanodiamond photocatalysis.

Zusammenfassung

Photokatalyse mit Nanodiamanten hat das Potenzial, eine Reihe energieintensiver industrieller Prozesse zu ersetzen und eine grüne Alternative für die Energiegewinnung und die Herstellung von chemischen Rohstoffen zu bieten. In dieser Arbeit werden die Eigenschaften von Nanodiamanten und insbesondere ihre elektronischen Strukturen im Zusammenhang mit Photokatalyse untersucht.

Zunächst charakterisieren wir eine Probe von mit Fluorwasserstoff fluorierten Nanodiamanten mittels weicher Röntgenspektroskopie. Die Röntgenphotoelektronen-Spektroskopie weist eine Fluorbedeckung von etwa 50 % auf den Proben nach. Die Analyse wird durch Röntgenabsorptions-Spektroskopie (*X-ray absorption spectroscopy*, XAS) und resonante inelastische Röntgenstreuungs-Spektroskopie (*resonant inelastic X-ray scattering spectroscopy*, RIXS) Experimente und Rechnungen ergänzt. Die quantenchemischen Berechnungen zeigen, dass sich die XAS-Signale mit zunehmendem Fluorgehalt der Oberfläche systematisch verschieben. Dagegen wird für mehrere unterschiedliche fluorierte Kohlenwasserstoffe die gleiche F K-Kanten RIXS Signatur gefunden, wobei das Hauptsignal jeweils von einer selektiven Anregung des F 1s-Elektrons in ein antibindendes C-F σ^*-Orbital stammt.

Des Weiteren untersuchen wir die Wechselwirkung von Nanodiamanten mit Adsorbaten in wässriger Dispersion, wobei der Schwerpunkt auf der Ladungstransferdotierung hin zu oxidativen Adsorbaten liegt. Der beobachtete Ladungstransfer steigt mit den Standardreaktionspotentialen der Adsorbate in Wasser an, und ändert sich mit den Energien der höchsten besetzten Molekülorbitale der benachbarten Nanodiamanten. Die angeregten Zustände von Nanodiamanten werden in ähnlicher Weise von oxidativen Adsorbaten beeinflusst, die einen erheblichen Teil der angeregten Elektronen einfangen. Die Bildung von Nanodiamant-Clustern führt zu einer Verringerung ihrer optischen Lücken und bewahrt die atomorbital-ähnlichen Formen der niedrigsten unbesetzten Orbitale.

Zuletzt stellen wir den Datensatz ND5k vor, der aus den Strukturen und Grenzorbitalenergien von 5.089 Nanodiamanten besteht. Auf Grundlage dieser Daten schlagen wir vor, Phosphor-dotierte Nanodiamanten für Sonnenlicht-Photokatalyse zu testen. Des Weiteren evaluieren wir moderne Algorithmen des maschinellen Lernens für die Vorhersage molekularer Eigenschaften von Nanostrukturen. In diesem Zusammenhang schlagen wir eine Erweiterung von Graph-basierten neuronalen Netzen mit atom-zentrierten Deskriptoren vor, die wir für die enn-s2s-Netzwerkarchitektur testen. Die besten Ergebnisse werden mit dem Graph-basierten Netzwerk PaiNN, die zweitbesten mit dem von uns modifizierten enn-s2s-Netzwerk erzielt.

Insgesamt tragen die in dieser Arbeit vorgestellten Ergebnisse zu einem besseren Verständnis der elektronischen Strukturen von Nanodiamanten bei und unterstützen damit die künftige Forschung auf dem Gebiet der Photokatalyse.

Acknowledgments

Throughout my work on this dissertation, I was greatly supported by my fellow colleagues, dedicated supervisors, and good-humored friends. I first and foremost thank my supervisors Annika, Frank and Joe, who have have put together their efforts to support and guide me through this work and to provide a fruitful environment to carry out my research. Much of this research was supported by the works of Dr. Karol Palczynski and Xiangfei Wang, and I thank both of you very much for your continued support. It was always a pleasure for me to discuss and advance our research in a very productive way. Furthermore, I was lucky to have very forthcoming collaboration partners at my side. Our works with Dr. Tristan Petit, Dr. Christoph Merschjann and Dr. Arsène Chemin on experimental aspects of the systems studied here have given me a different perspective and many new insights into the processes we investigated. Furthermore, I would like to thank all members of the Bandiella group, Dr. Hadi Arefi, Ka Hei, Seokhyun Hong, Dr. Pascal Krause, Fabian Langkabel, Sara Marando, Kunal Meshram, Dr. Karol Palczynski, Zhou Qingyuan, Dr. Victor Ruíz, Yannik Schütze, Börries von Seggern, Xiangfei Wang and Shilpa Yadav as well as the members of the AG Browne for their support during my thesis. I am also grateful to the HEIBRiDS doctoral program for funding my project and for welcoming me in the HEIBRiDS community. My special thanks go to Carla Kirschbaum as well as to my family and friends for their encouragement and non-scientific support.

Publications

Publications contained in this thesis

<u>T. Kirschbaum</u>, A. Chemin, M. Bartkowiak, D. Wong, C. Schultz, A. Krueger, T. Petit, A. Bande. Soft X-Ray Spectroscopy Characterization of HF-fluorinated Nanodiamonds. *In preparation. (Chapter 3)*

<u>T. Kirschbaum</u>, X. Wang, A. Bande. Ground and excited state charge transfer at aqueous nanodiamonds. *J. Comput. Chem.* Early View, DOI: https://doi.org/10.1002/jcc.27279. *(Chapter 4)*

<u>T. Kirschbaum</u>, B. von Seggern, J. Dzubiella, A. Bande, F. Noé (2023). Machine Learning Frontier Orbital Energies of Nanodiamonds. *J. Chem. Theory Comput.* 19, 14, 4461–4473. *(Chapter 5)*

F. Buchner, <u>T. Kirschbaum</u>, A. Venerosy, H. Girard, J.-C. Arnault, B. Kiendl, A. Krueger, K. Larsson, A. Bande, T. Petit, C. Merschjann (2022). Early dynamics of the emission of solvated electrons from nanodiamonds in water. *Nanoscale* 14, 46, 17188–17195. *(Chapter 4)*

<u>T. Kirschbaum</u>, T. Petit, J. Dzubiella, A. Bande (2022). Effects of oxidative adsorbates and cluster formation on the electronic structure of nanodiamonds. *J. Comput. Chem.* 43, 13, 923–929. *(Chapter 4)*

Further publications

K. Palczynski, <u>T. Kirschbaum</u>, A. Bande, J. Dzubiella (2023). Hydration Structure of Diamondoids from Reactive Force Fields. *J. Phys. Chem. C* 127, 6, 3217–3227.

C. D. Feldt, <u>T. Kirschbaum</u>, J. L. Low, W. Riedel, T. Risse (2022). Methanol oxidation on Au(332): methyl formate selectivity and surface deactivation under isothermal conditions. *Catal. Sci. Technol.* 12, 5, 1418–1428.

C. D. Feldt, <u>T. Gimm</u>, R. Moreira, W. Riedel, T. Risse (2021). Methanol oxidation on Au(332): an isothermal pulsed molecular beam study. *Phys. Chem. Chem. Phys.* 23, 38, 21599–21605.

J. Ren, L. Lin, K. Lieutenant, C. Schulz, D. Wong, <u>T. Gimm</u>, A. Bande, X. Wang, T. Petit (2020). Role of dopants on the local electronic structure of polymeric carbon nitride photocatalysts. *Small Methods* 5, 2, 2000707.

Abbreviations

CT	Charge transfer
DFT	Density functional theory
DFTB	Tight binding density functional theory
EA	Electron affinity
enn-s2s	Edge-conditioned neural network with set2set operator
EXAFS	Extended X-ray absorption fine structure
F-ND	Fluorinated nanodiamond
FLR	Fullerene-like reconstructions
GGA	Generalized gradient approximation
GNN	Graph neural network
H-ND	Hydrogenated nanodiamond
HOMO	Highest occupied molecular orbital
KRR	Kernel ridge regression
LDA	Local density approximation
LUMO	Lowest unoccupied molecular orbital
MAD	Mean absolute deviation
ML	Machine learning
MO	Molecular orbital
NN	Neural network
PaiNN	Polarizable atom interaction neural network
PCA	Principal component analysis
RIXS	Resonant inelastic X-ray scattering spectroscopy
ROCIS	Restricted open shell configuration interaction singles
SOAP	Smooth overlap of atomic positions
XANES	X-ray absorption near-edge structure
XAS	X-ray absorption spectroscopy
XES	X-ray emission spectroscopy
XPS	X-ray photoelectron spectroscopy
ZPR	Zero-point energy gap normalization

Contents

Chapter 1

Introduction

The properties that define a gem are rarity, durability, and beauty.
Ideas of beauty may [change, but] rarity and hardness have made
diamond a symbol of power, invulnerability, and ultimately love.

Jack Ogden *in* Diamonds : An Early History of the King of Gems

1.1   Motivation

The world is facing an ever-increasing demand for energy and resources as the
scarcity of resources and the environmental pollution are forcing us to redesign the
foundations of our global economies. New methods of producing green energy and
chemical base materials are in high demand. A large volume of research is dedicated
to improving and finding new processes for renewable energy harvesting and storage,
as well as sustainable production of chemical energy carriers and feedstocks.

In all of these fields, substantial improvements have been achieved over the last
decades. The efficiency of solar cells has skyrocketed, reaching new record-breaking
highs time and time again,[1,2] and modern solar-, wind-, water- and bio-power
plants are steadily replacing the old coal- and gas-fired plants worldwide.[3,4] In the
field of energy storage, research on battery materials is promising do deliver new
devices with higher energy and power densities at reduced economic costs in the near
future.[5] Furthermore, the sustainable production of hydrogen from electrolysis or
photocatalysis represents an alternative pathway for chemical energy storage.[6,7]

The production of chemical base materials currently largely relies on the re-
finement of natural oil and gas. In this field, the reduction of carbon dioxide is a
promising approach to synthesize small hydrocarbons, aiming to set up a cyclic carbon
pathway in which the greenhouse gas is captured, reduced and reused. Here, the CO_2
is first reduced to CO, and further to formaldehyde, methanol and methane.[8] These

products can subsequently be fused in catalytic coupling reactions to manufacture higher hydrocarbons.[9–11]

As of today, however, the sustainable production of hydrogen, the efficient reduction of carbon dioxide and many of the promising pathways for the sustainable production of chemical feedstocks that have been proposed over the last decades are still not economically viable on large scales.[7,12] The major obstacles usually consist of intricate catalyst fabrication pathways, low catalytic efficiency and insufficient long-term catalyst stability.[13] In this context, nanodiamond photocatalysis provides a promising pathway for driving high-energy reduction reactions by (sun-)light and replacing a range of energy-intensive industrial processes.[14] Nanodiamonds are small diamond particles that inherit most of their properties from macroscopic diamond, but provide a high surface-to-volume ratio along with a tunable surface structure. Their high stability, low toxicity and cheap synthesis make them ideal candidates for use in sustainable, green energy harvesting processes.[15]

In the catalytic process, the nanodiamonds are dispersed in water and illuminated by light, which causes electrons to escape from the particles and move into the surrounding water. The resulting solvated electrons are highly reactive species that may initiate high-energy reduction reactions in the aqueous phase.[16–22] This includes the generation of hydrogen from water splitting,[16,22] the reduction of carbon dioxide to carbon monoxide,[18,21] but also the reduction of nitrogen gas N_2 to ammonia NH_3[17,19,20] and the reduction of graphene oxide towards pristine graphene.[16] Utilizing these reactions, the production of chemical energy carriers and a wide range of feedstocks could be entirely driven by renewable energy and non-toxic carbonaceous materials.

Within the last decades, a wealth of experimental and theoretical research has been dedicated to the investigation and enhancement of nanodiamond-based photocatalysts.[14,15] This includes the synthesis, characterization and catalytic activity of nanodiamonds modified by nano-structuration, doping and composite materials.[14,15] However, as of today, continued research is required to further improve their properties and realize their full catalytic potential. In this context, this thesis explores the electrical and optical characteristics of nanodiamonds with the aim of understanding and tuning their properties towards highly efficient sunlight-driven photocatalysis on large industrial scales.

1.2 Outline of this Thesis

In the first part of this thesis, we investigate a sample of highly fluorinated nanodiamonds by soft X-ray spectroscopy. Fluorination is an efficient way of cleaning and passivating the nanodiamond surface, at the same time opening up pathways for further modifications. Within this study, combined experiments and quantum-chemical calculations are used to elucidate the electronic structure of the sample to gain a better understanding of the electronic and optical properties of fluorinated nanodiamonds.

The second research objective is the investigation of surface transfer doping of nanodiamonds. Surface transfer doping is an electrochemical phenomenon that alters the electronic structure of diamond surfaces in contact with aqueous adsorbates. In virtually all applications of (nano-)diamond, the material is either in direct contact with an aqueous system or covered by atmospheric moist. The effect is relevant in all applications in which changes of the electronic structure may influence the materials' target properties, *e.g.*, in photocatalysis, energy materials and biomedical applications. For nanodiamonds, their high surface to volume ratio may lead to a strong influence of surface effects on the overall properties, however, the effects of surface transfer doping on the electronic structure of nanodiamonds have hardly been studied before.[23] Therefore, we here present theoretical insights into the interplay between nanodiamonds and the aqueous oxidative adsorbates that initiate surface transfer doping. The electron transfer is quantified and the underlying principles are uncovered using quantum-chemical calculations within density functional theory.

Finally, to leverage nanodiamond design via machine learning, we introduce the new dataset ND5k, consisting of 5089 diamondoid and nanodiamond structures and their frontier orbital energies. The nanodiamond structures are optimized via tight-binding density functional theory, and their frontier orbital energies are obtained from hybrid density functional theory calculations. From this dataset we derive a qualitative design suggestion for nanodiamonds to be used as sunlight-active photocatalysis. We also compare recent machine learning models for predicting frontier orbital energies of similar structures as they have been trained on, and we test their abilities to extrapolate predictions to larger structures. For this task, we propose an extension of message passing neural networks that incorporates atom-centered descriptors into the learning architecture.

Chapter 2

Fundamentals

This thesis uses theories and methods from both theoretical chemistry and data science to investigate the chemical properties and characteristics of nanodiamonds in the context of photocatalysis. This chapter introduces the fundamental concepts that are relevant to this work to provide a basic understanding for all readers.

The first part presents the properties and applications of nanodiamonds, sheds light on the photocatalytic electron emission process, introduces soft X-ray-based spectroscopic techniques for their analysis, and explains the concept of surface transfer doping. The second part covers the basics of quantum chemistry with a focus on density functional theory. Finally, the supervised machine learning techniques used in this work are discussed.

2.1   Nanodiamonds

In the last century, diamond has grown immensely popular thanks to one of the most successful marketing campaigns in history, *A Diamond is Forever*, launched by the DeBeer jewelry company in 1939.[24] Besides its use in jewelry, diamond has found various applications in industry mostly due to its extraordinary hardness and insulating properties. Chemically, diamond is a carbon allotrope in which the carbon atoms are coordinated tetrahedrally in a stiff crystal lattice as shown in figure 2.1a. Beyond that, the physical and chemical properties of diamond can be diversely tuned by nano-structuration, surface modification or the incorporation of lattice dopants, such as boron and nitrogen.

a

b
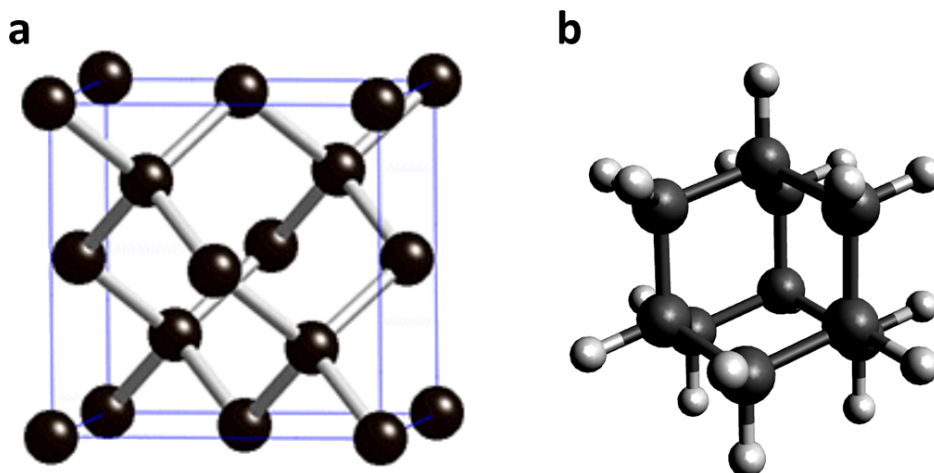
Figure 2.1: (a) Unit cell of the diamond crystal lattice and (b) molecular structure of adamantane. Carbon atoms in black, hydrogen atoms in grey.

In the field of nanoscience, nano-sized diamond particles, better known as nanodiamonds, represent an outstanding material class.[15] Nanodiamonds inherit the stability, biocompatibility and notable electronic properties from macroscopic diamond, and their high surface-to-volume ratio paired with a tunable surface structure make them ideal candidates for use in biomedicine and large-scale industrial applications. Moreover, unlike macroscopic diamond, the production of diamond nanoparticles is both cheap and easily scalable.

The smallest, molecular-scale nanodiamonds are the diamondoids. The most basic structure, adamantane, consists of only one cage of tetrahedrally coordinated carbon atoms saturated by hydrogen (see figure 2.1b). The further diamondoids (diamantane, triamantane, tetramantane, etc.) can be built by fusing multiple of these carbon cages.[25,26] They inherit most of the properties from nanodiamonds, but have increased optical gaps due to the quantum confinement effect.[27] For

modelling the properties of nanodiamonds, one may resort to modelling the smaller diamondoids, because the reduced system sizes enable high-accuracy calculations of their properties.

The most prominent technique for the fabrication of nanodiamonds is the detonation method. Here, a mix of hydrocarbons and explosive organic chemicals, such as TNT and hexogen, is ignited in a closed metallic chamber, and nanodiamonds are collected from the detonation soot.[15] These particles typically contain heteroatoms such as nitrogen from the organic precursors in their cores and are covered by amorphous carbon patches on their surfaces. They are subsequently purified and further modified to obtain specific size distributions, surface terminations and dopant concentrations.[15] To obtain high-purity materials, nanodiamonds can also be fabricated by high-temperature high-pressure techniques[28,29] or collected from meteors on which they occur naturally.[30,31] Diamondoids, in contrast, can either be extracted from natural oil[32] or synthesized from organic precursors.[33]
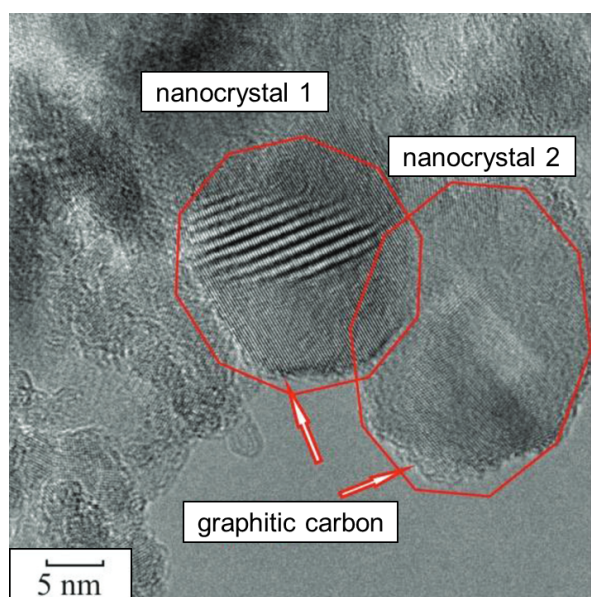
Figure 2.2: Electron microscopy images of nanodiamonds produced from the detonation method. The nanocrystals of about 10 nm diameter are highlighted in red. Reprinted (modified) from Plotnikov *et al.* with permission from AIP publishing.[34]

Figure 2.2 shows a high-resolution electron microscopy image of two nanodiamond crystals produced by the detonation method.[34] The two nanocrystals are highlighted by red circles, and the arrows indicate the presence of amorphous carbon shells on the surfaces. Here, the diamond crystal faces are clearly visible, indicating a high crystallinic purity of the material. The nanodiamonds can then be further purified and different surface species attached according to the needs of the specific application.[15,35–37]

Nanodiamonds have found applications in bio-imaging,[38–40] drug transport,[41–44] sensing,[45–47] tribology,[48–50] catalysis[16–19,21,22] and energy materials.[51] The biomedical applications rely on their low toxicity: Nanodiamonds are highly stable and inert, and therefore hardly interact with any biological system. Utilizing their tunable surface chemistry, they can be used as transportation platforms by mounting biologically active substances on their surfaces. For example, a nanodiamond equipped with a targeting molecule and an active drug will find its way into the targeted site, where the drug molecule can be released. This approach was investigated, *e.g.*, for inflammation and cancer treatments.[41,42,44]

For sensing applications, nitrogen dopants are introduced into the carbon lattice to obtain nitrogen-vacancy centers, in which one carbon atom is replaced by nitrogen and a neighboring lattice site remains unoccupied (vacant). The nitrogen-vacancy centers introduce unpaired electrons into the nanodiamond lattice which are stable even at room temperatures. These electrons may interact with light, enabling applications in quantum information materials, or with unpaired electrons of adjacent systems, as used for applications in bio-sensing.[45]

Finally, nanodiamonds are active photocatalysts for high-energy reduction reactions in the aqueous phase. When illuminated with ultraviolet light, hydrogen- or amine-terminated diamond materials emit electrons into the surrounding medium, *i.e.*, into the surrounding water. Utilizing this process, nanodiamonds have been used to enable the photocatalytic reduction of graphene oxide, carbon dioxide, nitrogen and water molecules.[16–19,21,22] More details on the reaction will be given in the following section.

2.1.1   Photocatalytic Electron Emission

Diamond has a unique electronic structure with a comparatively high valence band maximum and a very high conduction band minimum energy. The energetic positions are illustrated in figure 2.3 alongside the energy levels of other common semiconductors. Most notably, the positive absolute energy of the diamond conduction band minimum with respect to vacuum level (0 eV) renders a negative electron affinity of diamond. This property enables the use of diamond materials as an electron emitter for photocatalytic applications. If electrons are lifted into the conduction band, they are no longer bound to the diamond, allowing them to be liberated into the surrounding medium. In nanodiamond photocatalysis, the electrons are usually transferred into water which can be regarded as an amorphous semiconductor with a conduction band minimum energy at around -1 eV.[20,52,53]

The free electron constitutes both the simplest possible anion and a highly reactive reduction agent. In a range of experimental studies, (nano-)diamond was successfully used to produce solvated electrons for the reduction of graphene oxide to pristine graphene, CO_2 to CO, N_2 to NH_3, and H_2O to H_2 and O_2.[16–19,21,22] In conventional industrial plants, these reduction processes are driven by either high temperatures and pressures or low-efficiency electrolysis, thereby consuming large amounts of energy. The use of non-toxic nanodiamonds in a sunlight-driven process presents a promising green alternative to these techniques. However, owing to diamond's large band gap of 5.5 eV, the promotion of electrons from the valence band into the conduction band requires high-energy photon excitations. For efficient sunlight harvesting, a modification of the material towards having a band gap around the solar energy maximum (2.6 eV) would be highly desirable.

Generally, the introduction of additional surface states has been a promising attempt to facilitate low-energy electron emission from (nano-)diamond. In 1999, Cui *et al.* reported that electrons can be facilely emitted from diamond into vacuum using ultraviolet light.[54] This effect was attributed to small patches of amorphous carbon present on the diamond surface, which provide additional occupied electronic
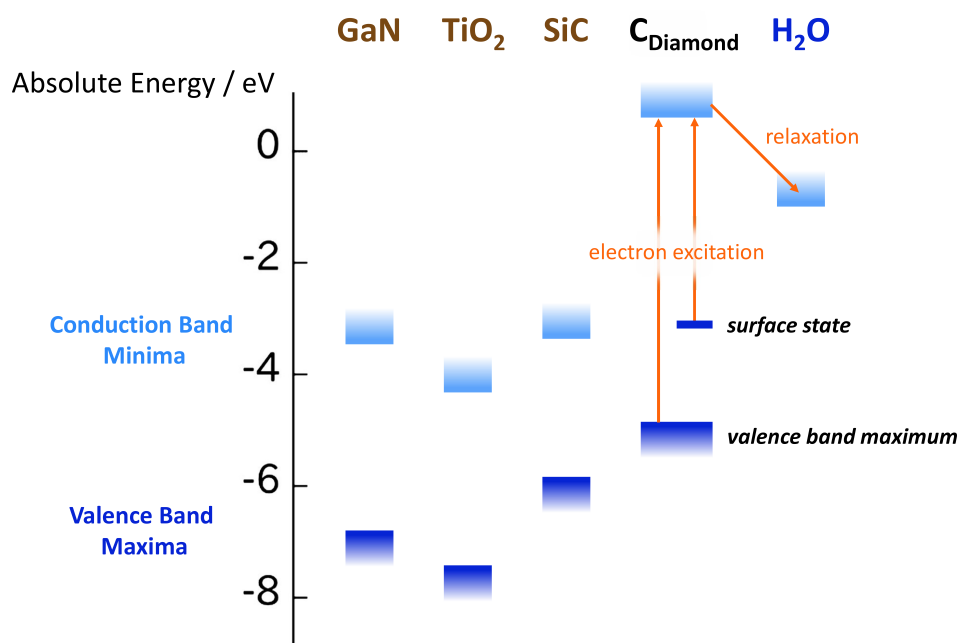
Figure 2.3: Band energy levels of common semiconductors, diamond, and the valence band energy of water. The arrows indicate the excitation of an electron into the diamond conduction band and subsequent relaxation and transfer into the water conduction band. The introduction of occupied surface states into the diamond band gap will lower the energy required for electron excitation into the conduction band. Reprinted (modified) from Zhang and Hamers with permission from Elsevier.[21]

states on the diamond surface from which the electrons can be transferred into the diamond conduction band with a low energy barrier. These surface state are schematically depicted in figure 2.3. A similar effect was recently reported for electron emission from detonation nanodiamonds.[55] Further approaches of introducing additional surface states consist of specific nanostructuration,[56–58] the addition of boron dopants[57,58] or the use of composite materials, *e.g.*, metals.[20,59]

The details of the electron emission process from nanodiamod into water currently remain under debate.[55,60] Generally, the mechanism can be imagined as follows: Upon light excitation, one electron is promoted into the diamond conduction band and moves to the material's surface. Subsequently, it is transferred into the water conduction band[53] where it is initially delocalized among several water molecules.[61,62] Upon formation of a defect in the water hydrogen bond network, the electron starts to move towards the dangling hydrogen and initiates the formation of a cavity in the water structure.[63] The electron then diffuses through the bulk water, encapsulated in the cavity, and finally reacts, *e.g.*, with a water proton.[64] The precise mechanisms, time scales, and influences of structural features remain under investigation as of today.[55,65]

2.1.2   Characterization by Soft X-Ray Spectroscopy

The structures of nanodiamonds can be diversely tuned to modify their chemical and physical properties, as required for the respective application. The analysis of these properties can be accomplished by various spectroscopic methods, physical measurements and imaging techniques. This section introduces a family of spectroscopic methods that are based on soft X-ray excitation and have been used for the investigation of nanodiamonds.[57,66–70] An overview of the electronic processes underlying the techniques discussed here is given in figure 2.4.

Soft X-ray spectroscopies generally target the excitation of core electrons from a material to deduce information on its elemental composition and/or electronic structure. The generation of brilliant and focused high-intensity X-rays requires large-scale devices that are operated at high energies. For example, at synchrotron facilities, electrons are accelerated and undulated in large vacuum tubes, and the emitted bremsstrahlung is used as a light source for spectroscopic measurements.

In X-ray absorption spectroscopy (XAS), the core electrons of the sample are excited by X-ray photons and the energy-dependent absorption of photons by the sample is recorded. The materials are probed at element-specific energies which are named after the principle quantum number from which the excitation occurs, where

Molecular Orbital Picture **Many-Body State Picture**
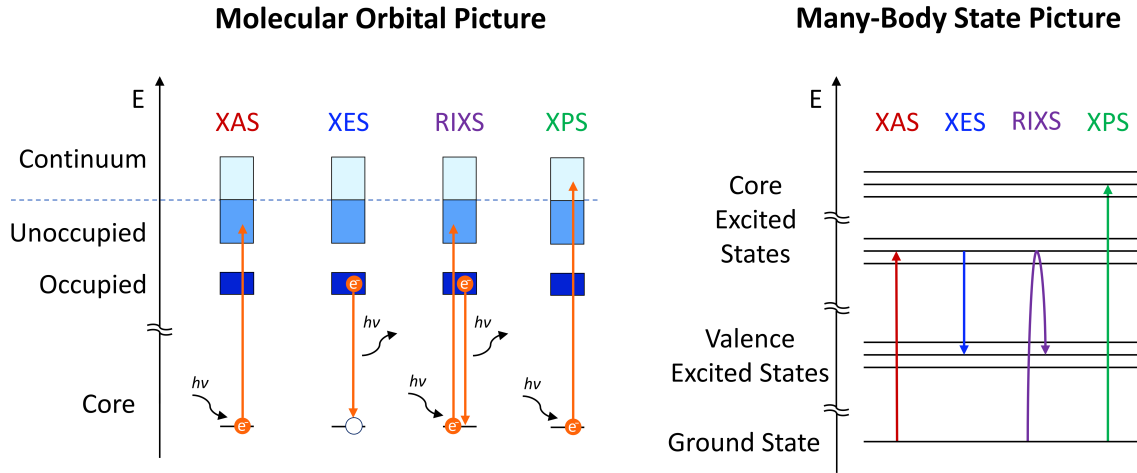
Figure 2.4: Scheme showing one typical process for each type of electronic spectroscopy: XAS, XES, RIXS and XPS. Incident and emitted photons are indicated as $h\nu$. Left: Molecular orbital picture, right: Many-body state picture. In XAS, the absorption of photons upon electronic excitation from a core orbital into an unoccupied orbital is recorded. Non-resonant XES probes the relaxation of a valence electron into a previously created core-hole. In RIXS, the resonant relaxation of a valence electron upon core-excitation is measured. XPS records the kinetic energy of the core-excited electrons that are emitted from the sample.

n = 1, 2 corresponds to the K-, L-edge, respectively. The spectra are composed of the X-ray absorption near-edge structure (XANES) and the extended X-ray absorption fine structure (EXAFS) region, which correspond to different effects occurring upon X-ray excitation.[71] In the XANES region, which comprises the pre-edge and the rising edge, the core electrons are excited into virtual orbitals. The spectral shape of the XANES region is determined by the local electronic structure of the excited atoms. Within this work, we only consider the XANES region for analyzing XAS spectra. At higher incident energies, the core electrons are excited into the continuum. From here, they are scattered at the surrounding atoms, resulting in an interference pattern that is detected in the EXAFS region. This part of the spectrum contains information on the local geometry of a sample and can be used to deduce the number and distances of neighboring atoms in a highly ordered sample.

For the calculation of excitation spectra, the electronic transition rates or oscillator strengths of the underlying signals can be computed. For the quantum-chemical calculation of transition rates Γ, Fermi's golden rule[72] provides a good approximation for the excitation of an initial state $|0\rangle$ into excited states $|n\rangle$ as a result of a weak perturbation:

$$\Gamma_{0\to n} = \frac{2\pi}{\hbar} \left| \langle n|\hat{\vec{\mu}}|0\rangle \right|^2 \rho\left(E_n\right). \tag{2.1}$$

Here, $\hbar$ is the reduced Planck constant, $\langle n|\hat{\vec{\mu}}|0\rangle$ is the respective matrix element of the dipole moment operator $\hat{\vec{\mu}}$, and $\rho\left(E_n\right)$ is the density of states at the energy E_n of the final states (see section 2.2.1 for a short introduction to quantum chemistry).

When a core electron is excited, the resulting core hole will be replenished by the relaxation of a valence electron, which is accompanied by the emission of a photon. This process is monitored by X-ray emission spectroscopy (XES), where the energy of the emitted photons is recorded. If excitation and relaxation occur resonantly, the intensity of the signal can be measured as a function of the incoming photons' energies within resonant inelastic X-ray scattering spectroscopy (RIXS). RIXS is a powerful tool for elucidating the valence electronic structure of materials by probing low lying excited states with element-specific transition orbital character.[73–76] In the past, RIXS has especially been used for probing transition metal complexes, however, its potential applications are much broader.[77,78]

The intensities of the RIXS process can be calculated by the Heisenberg-Dirac equation,[74,77] which describes the probability F of a process starting from the ground state $|g\rangle$ *via* an intermediate core-excited state $|i\rangle$ to a final valence-excited state $|f\rangle$:

$$F\left(E_{in}, E_{out}\right) = \sum_f \left| \sum_i \frac{\langle f|\mu_\rho|i\rangle \langle i|\mu_\lambda|g\rangle}{E_g + E_{in} - E_i - i\Gamma_i} \right|^2 \times \frac{\Gamma_f/2\pi}{\left(E_g - E_f + E_{in} - E_{out}\right)^2 + \Gamma_f^2/4}.$$

(2.2)

Here, E_g, E_i and E_f are the energies of the ground state, the intermediate and the final states, μ_ρ and μ_λ are the dipole moment operators, and Γ_i and Γ_f represent the lifetimes of the intermediate and the final state, respectively.

Finally, X-ray photoelectron spectroscopy (XPS) is used for the nondestructive analysis of elemental compositions. Here, the material's core electrons are excited into the continuum and emitted from the sample, and their kinetic energies are measured to probe their binding energies.[79] Synchrotron-based XPS, using different X-ray energies, is a surface sensitive technique that can precisely characterize the surface moieties on a given sample. Changing the X-ray energy allows for tuning the penetration depth of the photons and allows to selectively analyze either surface or bulk structures.

2.1.3 Surface Transfer Doping

In most applications, the nanodiamonds are exposed to an aqueous or humid environment. In 1989, Landstrass and Ravi demonstrated that hydrogen-terminated diamond in contact with ambient moist displays a huge surface conductivity, a highly atypical property for diamond-based materials.[80] Almost 20 years later, Chakrapani *et al.* established that this increased surface conductivity is induced by a spontaneous rearrangement of electrons that occurs in the thin water layer on the diamond surface.[81] Here, electrons are transferred from the diamond surface towards an oxidative species present in the water, such as O_2 or H_3O^+, thereby creating holes in the diamond surface that act as charge carriers. The phenomenon has become known as carrier hole doping or surface transfer doping and was investigated in many experimental[82–87] and theoretical studies.[23,88–96]
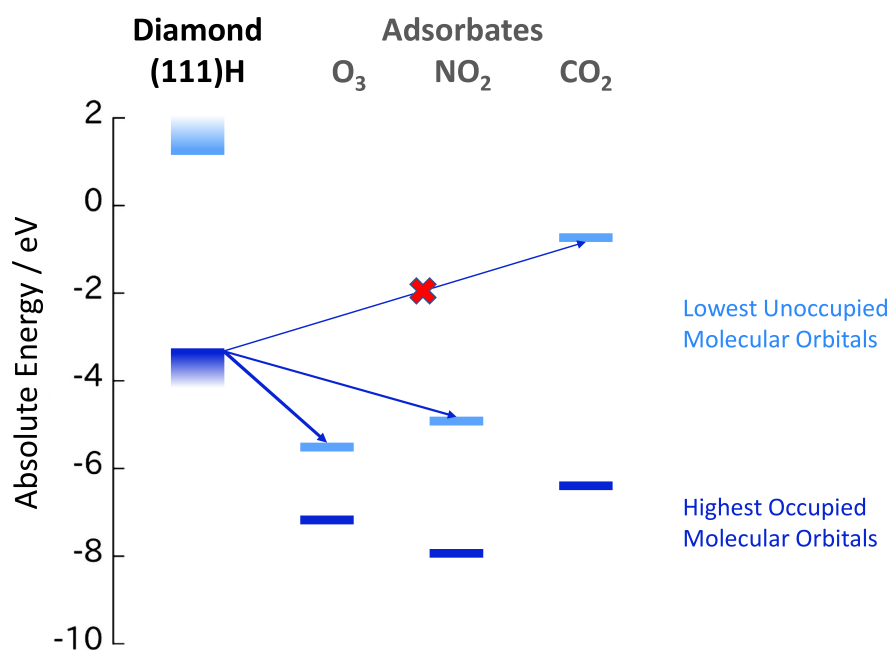

Figure 2.5: Band energy levels of the H-terminated diamond (111) surface and frontier orbital energies of molecular adsorbates. The arrows indicate the direction of electron transfer from the occupied energy levels of diamond into the unoccupied energy levels of the adsorbates (electron transfer doping). Reprinted (modified) from Takagi *et al.* with permission from Elsevier.[94]

Generally, surface transfer doping occurs, if the highest occupied electronic state of a surface (valence band maximum) is higher in energy than an unoccupied energy level of the adsorbate molecule (*i.e.*, the lowest unoccupied molecular orbital, LUMO). The effect is depicted in figure 2.5 for the H-terminated diamond (111) surface and three molecular adsorbates. The electrons of the H-terminated diamond (111) surface

will relax from the conduction band into the unoccupied orbitals of ozone (O_3) and nitrogen dioxide (NO_2). The electron transfer towards ozone will be higher than towards the nitrogen dioxide, because the electrons relax into a lower lying orbital. For carbon dioxide (CO_2), no electron transfer occurs, because the adsorbate's LUMO is higher in energy than the diamond (111)H surface's valence band maximum. [94]

In principle, the occurrence of this effect is not limited to diamond, but can be observed at other materials' surfaces as well. [94] However, most materials have their conduction band maximum at relatively lower energies (*cf.* figure 2.3). Therefore, the effect is relevant mostly to diamond-based materials and less commonly observed in other fields. For nanodiamonds, their high surface-to-volume ratio may promote even more pronounced effects as compared to bulk diamond. [23,84–86,96]

2.2 Molecular Modelling and Simulation

The analytical mathematical description of physical systems is as old as 300 years, when Newton first realized that apples fall from trees because of gravitation, thereby founding the field of classical (Newtonian) mechanics. About 200 years later, quantum mechanics was invented to describe the properties and evolution of atomic and molecular systems that fall outside the realm of classical physics. Today, both classical and quantum mechanical modelling and simulation are used hand in hand with experimental investigations to understand and advance complex systems in chemistry, physics and materials science.

2.2.1 Quantum Chemistry

The theories of quantum chemistry provide the groundwork for computing the static properties and dynamic evolution of atomic and molecular systems.[97–99] In 1926, Schrödinger postulated that a quantum chemical system can be described by a wave function ψ which represents its quantum state and describes its evolution in time *via* the partial differential equation

$$i\frac{\partial}{\partial t}\Psi = \hat{H}\Psi,\tag{2.3}$$

today known as the *time-dependent Schrödinger equation*.[99] Here, Ψ is a high-dimensional, in principle complex function, and $\hat{H}$ is the Hamilton operator that characterizes the state and generates the evolution of the system. The properties of a stationary system in its ground state can be obtained from the *time-independent Schrödinger equation*

$$\hat{H}\Psi = E\Psi,\tag{2.4}$$

where E is the total energy of the system.[99] However, this equation can only be solved exactly for one-electron systems.

The fundamental method to obtain approximate solutions for many-electron systems was developed by Douglas Hartree and Wladimir Fock, and is known as the *Hartree-Fock method*.[100–105] In this method, each energy eigenfunction is described by a single Slater determinant, an antisymmetrized product of one-electron wave functions (*i.e.*, orbitals).[106] The interactions of electrons are approximated by means of a mean electronic field, coining the term *mean field method*, and the electronic wave function is described *via* a linear combination of basis functions:

$$\Psi = \sum_i c_i \varphi_i \tag{2.5}$$

with coefficients c_i and basis functions φ_i. Nuclear motion and relativistic effects are neglected by Hartree-Fock.

Building on this approach, a range of *post-Hartree-Fock methods* have been developed over the years. Most prominently, Møller-Plesset perturbation theory, the coupled cluster method and the configuration interaction method are capable of converging to the exact solution of the time-independent Schrödinger equation (2.4) for up to 10-electron systems within a given basis set.[107] The perturbation theory developed by Møller and Plesset, usually used at second order (MP2), adds electron correlation effects by means of Rayleigh–Schrödinger perturbation theory.[108,109] In the coupled cluster method, multi-electron wavefunctions are constructed using the exponential cluster operator to account for electron correlation,[110,111] and the configuration interaction method builds the wave function from more than one electronic configuration using a linear combination of Slater determinants.[112–114] These methods are very successful in describing small chemical systems, but their unfavorable computational scaling prevents their use for large systems such as proteins or nanoparticles.

2.2.2   Density Functional Theory

Density functional theory (DFT) provides a different but related approach to describe the state of a quantum chemical system. By using the electron density ρ instead of a many-body wave function, a significant reduction in the dimensionality of the problem is achieved, because the electron density of any system is always only three-dimensional. Thus, DFT can be applied to much larger systems consisting of hundreds or even thousands of atoms.[115]

DFT was first introduced by Thomas[116] (1927) and Fermi[117] (1928) but has become popular only with the contributions of Hohenberg and Kohn in 1964.[118] In their famous theorems, they proved that (a) the total energy of a system is a unique functional of its electron density, and (b) the density obeys the variational principle, *i.e.*, given the exact functional and an arbitrary density $\rho(r)$ the functional yields the lowest energy if, and only if, the $\rho(r)$ is the true ground state density.[118] These theorems have been further developed in *Kohn-Sham DFT* for non-interacting electrons in an external potential.[119] This Nobel prize decorated work has enabled the precise calculation of the electronic properties of large systems and solid materials,

and has therefore become the workhorse of modern computational chemistry.

In Kohn-Sham DFT, the total energy of a system is obtained as the sum of the kinetic energy of the electrons $T[\rho]$, the electron-nuclei interaction $V_{ne}[\rho]$ and the electron-electron interaction $V_{ee}[\rho]$. The last term can be formulated as the sum of the classical Coulomb repulsion $J[\rho]$ and the so-called exchange-correlation part $V_{XC}[\rho]$ that contains the energy contributions of Pauli repulsion and electronic correlation, *i.e.*,

$$E_{tot}[\rho] = T[\rho] + V_{ne} + J[\rho] + V_{XC}[\rho]. \tag{2.6}$$

For the calculation of a system's electron density, Kohn and Sham provided an approach similar to the linear combination of atomic orbitals.[119] The non-interacting system is described *via* the Kohn-Sham orbitals Ψ^{KS} [115] as

$$\rho^{KS}(r) = \sum_{i=1}^{n} |\Psi_i^{KS}(r)|^2. \tag{2.7}$$

These are constructed from a set of l basis functions Φ_μ and have no physical meaning, but are purely mathematical constructs, obtained as

$$\Psi_i^{KS} = \sum_{\mu=1}^{l} c_{\mu i} \Phi_\mu(r). \tag{2.8}$$

The whole system can then be calculated in a self-consistent approach using the one-electron Kohn-Sham equations

$$\left(-\frac{1}{2} \nabla^2 + V_s(r) \right) \Psi_i^{KS}(r) = \varepsilon_i \Psi_i^{KS}(r), \tag{2.9}$$

where

$$V_s(r) = V_{ne}[\rho] + J[\rho] + V_{XC}[\rho] = \sum_{\alpha=1}^{N} \frac{Z_\alpha}{r_{1\alpha}} + \sum_{j=1}^{n} \frac{|\Phi_j(r_2)|^2}{r_{12}} dr_2 + \frac{\partial E_{XC}(\rho)}{\partial \rho(r_1)} \tag{2.10}$$

with N nuclei labeled α, nuclear charges Z_α, and n electrons labeled j.

The main drawback of DFT is that the exchange-correlation functional $V_{XC}[\rho]$ cannot be calculated exactly. Its precise determination constitutes a major challenge and countless approximate functionals have been developed over the last decades. According to Perdew, they fit in only a few categories which are summarized in *Jacob's ladder of heaven* (figure 2.6).[115,120]
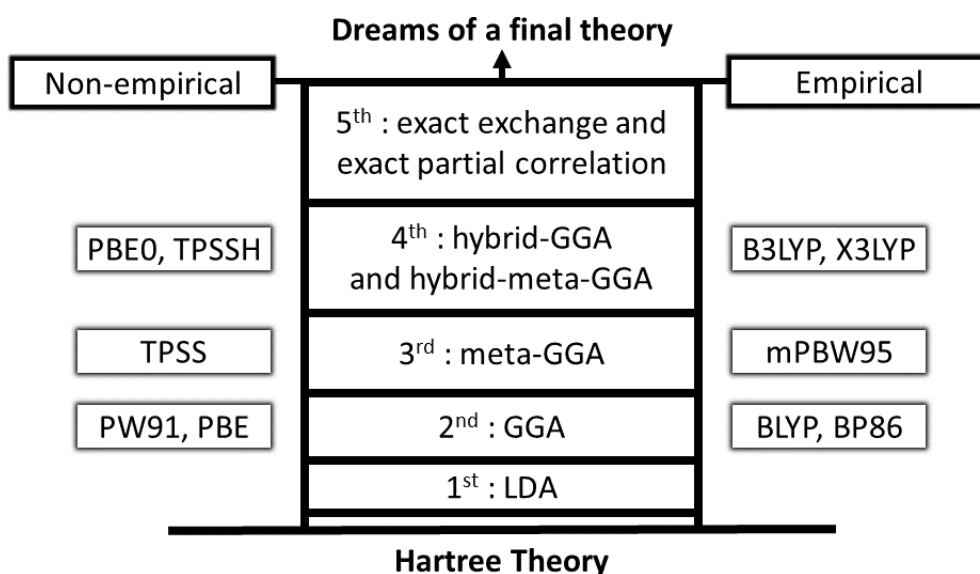
Figure 2.6: *Jacob's ladder of heaven* ranking the quality of exchange-correlation functionals in DFT.[115,120] LDA: Local Density Approximation, GGA: Generalized Gradient Approximation. The functionals are usually named after the initials of the developers' last names and sometimes the year of publication.

In local density approximation (LDA) functionals, only the electron density at position r is used to calculate $E_{XC}(r)$. By also taking into account the gradient of the local charge density one arrives at generalized gradient approximation (GGA) functionals, which can further be extended to meta-GGA functionals by employing higher derivatives. Moreover, a portion of the exchange energy obtained from Hartree-Fock calculations can be admixed, yielding so-called hybrid functionals. Further improvements are obtained, *e.g.*, by using range-separated hybrid functionals, in which the fraction of Hartree-Fock exchange is increased for long-range interactions.[121] Another distinction can be made by separating functionals which are constructed purely mathematically (non-empirical) from those whose parameters are fitted to experimental data (empirical).

After the choice of the functional, the second major parameter in a DFT calculation is the choice of basis functions Φ_μ (see eq. 2.8). In an ideal setup, the calculation systematically converges to the exact result with increasing number of basis functions employed, however, in practice, the crafting of basis sets that display this behavior is an intricate task. Today, one of the most commonly used set of basis functions is the Gaussian basis set developed by Ahlrichs and co-workers.[122–124] Furthermore, it has been shown that the use of additional dispersion correction methods is indispensable to account for the weak, but non-negligible van-der-Waals interactions in weakly bonded systems.[125,126]

The cost of a DFT calculation increases with the complexity of the exchange-correlation functional, the size of the basis set and the number of electrons in the system.[115] To reduce the computational effort for calculations of large solid materials, the cheaper tight-binding DTF (DFTB) can be employed.[127] In this variant, only the valence electrons of the systems are calculated explicitly – all other electrons are considered to be *tightly bound* and their interactions are approximated using a fixed set of parameters. A robust parametrization and implementation of DTFB was recently published by the Grimme group.[128,129]

The calculation of excited states and, subsequently, electronic spectra constitutes a major task for DFT, for which the electronic structure of a given material needs to be captured with high accuracy. In this context, the DFT-based restricted open-shell configuration interaction singles (DFT/ROCIS) method was developed to provide an improved description of excited states.[130] In the wavefunction-based configuration interaction singles (CIS) approach, all possible singly excited determinants are admixed to the ground state to obtain the wave function Ψ_{CIS}:

$$|\Psi_{CIS}\rangle = c_0\Phi_0 + \sum_{i,a} c_i^a |\Phi_i^a\rangle .$$

(2.11)

Here, Φ_0 is the ground state determinant with coefficient c_0, and c_i^a are the coefficients of the singly excited determinants Φ_i^a, in which one electron i is excited into the virtual orbital a. In DFT/ROCIS, Kohn Sham orbitals are used to construct Kohn Sham determinants that are calculated according to the restricted open shell (RO) ansatz.[130] In this way, DFT/ROCIS combines the accurate and computationally cheap description of band structures and orbitals from DFT with the ability to correctly describe spin-coupling, multiplet structure and spin–orbit coupling of the CI approach.

In systems for which it is necessary to include effects of a solvent, the computational cost of modelling a full solvation shell can quickly grow prohibitively high. By modelling the solvent as a polarizable continuum, rather than individual molecules, the electrostatic effects of the environment can be included at much lower cost. In the conductor-like polarizable continuum model, for example, the solute is placed in a cavity of roughly molecular shape and surrounded by apparent polarization charges. These charges are in turn determined by the solute, and describe the solvent reaction field around it.[131]

2.3   Machine Learning

Machine learning (ML) is a sub-discipline of artificial intelligence and data science that aims at extracting patterns and deriving knowledge from data. The field can be further divided into supervised learning, which is almost exclusively used in this thesis, unsupervised learning and reinforcement learning. Supervised learning aims to reproduce a mapping by "learning" from a set of pre-computed data. Most prominently, deep neural networks (NNs) have recently shown huge successes in various tasks, ranging from speech recognition[132] to protein structure prediction.[133] Throughout this thesis, we use different chemistry-focused supervised learning techniques to accelerate the quantum mechanical models at hand.

2.3.1   Machine Learning in Chemistry

In chemistry, ML has been used to tackle a large variety of problems, ranging from solving the Schrödinger equation (2.4)[134,135] over sampling the space of chemical structures[136,137] to coarse-graining of molecular dynamics simulations.[138,139] However, the prevalent application of ML in chemistry consists of supervised learning with data from high-accuracy quantum chemistry models to circumvent expensive calculations.[140–143] Traditionally, the various molecular modelling techniques provide different options on the trade-off between accuracy and computational effort (see figure 2.7). Here, supervised ML provides a new approach to model systems with high accuracy at much reduced computational cost. However, as of today, the use of ML remains limited to specialized applications. The major bottleneck in the ML workflow usually consists of the acquisition of data for training and testing the models, and the trained algorithms can then only be used for the specific application that was targeted during the training.

The primary application of supervised ML in chemistry is high-throughput screening for materials and drug discovery.[141] Here, the desired properties are calculated for a representative training set of molecules that samples the chemical compound space of interest using a high-accuracy model. After training the ML algorithm, the ML model can then predict these properties at a fraction of the cost of the underlying quantum chemical model. These approaches can efficiently screen millions to billions of candidate materials.[144,145] The resulting set of structures can be further refined using more elaborate modelling techniques and finally needs to be tested in experimental setups to confirm their applicability.[146–148]

The second major use case is the fast computation of energies and forces to drive
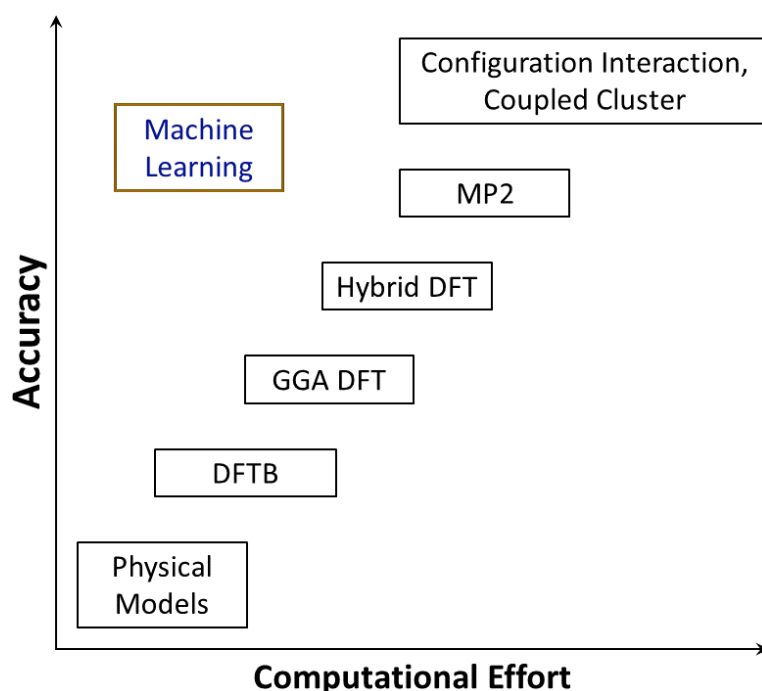
Figure 2.7: Simplified schematic representation of the accuracy *vs.* computational effort trade-off of conventional molecular modelling techniques. Supervised ML provides models at high accuracy with much reduced computational cost.

molecular dynamics simulations at high accuracy.[142] Therefore, a set of snapshots that sample the configuration space of interest is calculated by a quantum chemical model and used for training, and the resulting ML algorithms can then run the corresponding simulations at much larger system sizes and time scales than the underlying model. Such approaches have been used, *e.g.*, for large-scale simulations of metals[149,150] and for exploring the phase diagram of water.[150–153] To learn atomic forces for molecular dynamics simulations, usually the total potential energy of the system is predicted as the sum of atomic potential energies $E_{total}^{pot} = \sum_\alpha e_\alpha^{pot}$, and the forces are obtained as derivatives of the atomic energies $f_\alpha = \dot{e}_\alpha^{pot}$. This approach provides a physically motivated way of calculating forces as potential energy derivatives, leading to intrinsically energy-conserving ML force fields, and allows both atomic forces and total potential energies to be utilized for the training process.[142,149]

The main challenge of chemistry ML consists of finding appropriate vectorial representations of molecular structures. Traditional ML methods such as deep NNs operate on fixed-size vectors to compute the target properties. However, because molecules are very different in their shapes and sizes, finding a unifying fixed-size vector representation is not straightforward. Early approaches have used sets of easy to compute properties to describe the chemical systems (geometric descriptors, con-

stitutional descriptors, molecular properties, etc.) which, however, were very limited in their effectiveness. [154] Subsequently, different approaches have been developed to capture molecular geometries in a vector format, including extended connectivity fingerprints, [155] the Coulomb matrix, [156] and bag of bonds. [157] However, all of these approaches come with certain limitations, rendering them suboptimal for use in applications. [158]

In recent years, two major approaches have become popular for ML in chemistry: atomic fingerprinting techniques and graph neural networks (GNNs). Both methods rely on the construction of atomic rather than molecular descriptors. Molecular representations are then obtained by summing up or averaging over the atomic descriptors to predict extensive or intensive properties, respectively. These two approaches will be discussed in more detail in the following sections.

2.3.2   Atomic Fingerprints

Atomic fingerprinting techniques capture the geometric environment of an atom in a fixed-size vector format using deterministic functions that retain rotational and translational symmetry as well as the invariance with respect to atom indexing. We will here discuss two of the most commonly used techniques: Atom-centered symmetry functions as proposed by Behler and Parinello [149], and the smooth overlap of atomic positions (SOAP) descriptor proposed by Bartok *et al.* [159] Further fingerprinting techniques include the overlap matrix fingerprint, [160] modified Behler–Parrinello symmetry functions, [161] the Faber–Christensen–Huang–Lilienfeld descriptor [162] and Gaussian-type orbital-based density vectors. [163]

In their seminal work, Behler and Parinello proposed the use of atom-centered symmetry functions as inputs for dense NNs to predict atomic energies and forces. [149] Here, an atomic fingerprint vector consists of sets of atom-centered many-body radial and angular functions G that describe the geometric environment of a central atom i. The radial environment is described by the sum of two-body terms, *e.g.*, in the form

$$G_i^1 = \sum_j e^{-\eta(r_{ij}-r_c)^2} f_c(r_{ij}), \qquad (2.12)$$

including atomic distances r_{ij} of atoms j around the central atom i within the cutoff distance r_c. The cutoff function $f_c(r_{ij})$ smoothly decays to zero upon approaching r_c. The angular environment is described using sums of three-body terms, *e.g.*, as

defined in the two examples below: [149,164,165]

$$G_i^2 = 2^{1-\zeta} \sum_{j,k\neq i}^{all} (1 + \lambda \cos(\theta_{ijk}))^\zeta \; e^{-\eta(r_{ij}^2 + r_{ik}^2 + r_{jk}^2)} \; f_c(r_{ij}) f_c(r_{ik}) f_c(r_{jk}), \qquad (2.13)$$

$$G_i^3 = 2^{1-\zeta} \sum_{j,k\neq i}^{all} (1 + \lambda \cos(\theta_{ijk}))^\zeta \; e^{-\eta(r_{ij}^2 + r_{ik}^2)} \; f_c(r_{ij}) f_c(r_{ik})). \qquad (2.14)$$

The atom-centered symmetry function of atom i is then constructed using different radial and angular functions G_i with various values of η, λ, ζ and r_c.

In the SOAP approach,[159] a Gaussian of width σ is centered on each atom j within the cutoff distance r_c of a central atom i. The resulting density of atoms is multiplied with a cutoff function f_c which smoothly approaches zero at the cutoff radius r_c,

$$\rho_i(\mathbf{r}) = \sum_j \exp\left(-\frac{(\mathbf{r} - \mathbf{r}_{ij})^2}{2\sigma^2} \right) \times f_c\left(|\mathbf{r} - \mathbf{r}_{ij}|\right). \qquad (2.15)$$

This density is then expanded in terms of orthogonal radial functions $g_n(r)$ and spherical harmonics $Y_{lm}(\theta, \phi)$ as

$$\rho_i(\mathbf{r}) = \sum_{nlm} c_{nlm}^i g_n(r) Y_{lm}(\theta, \phi), \qquad (2.16)$$

where $c_{nlm}^i = \langle g_n Y_{lm} | \rho_i \rangle$. Finally, the rotationally invariant scalar descriptors p of the central atom i's environment are obtained as

$$p_{nn'l}^i = \sqrt{\frac{8\pi^2}{2l+1}} \sum_m c_{nlm}^i \left(c_{n'lm}^i\right)^*. \qquad (2.17)$$

The final SOAP fingerprint vector $\mathbf{F}^i$ then contains all $p_{nn'l}^i$ with n, $n' \leq n_{max}$ and $l \leq l_{max}$.[159,165,166]

The different fingerprinting techniques vary in their quality concerning their abilities to capture minute geometric changes of a system without using a very large number of descriptor functions. Apart from that, most fingerprints have the common drawback of being highly sparse.[165] Accordingly, different techniques such as principal component analysis (PCA) can be employed to condense the fingerprints into a lower dimension while retaining most of the structural information they encode.[166,167]

2.3.3   Graph Neural Networks

GNNs for molecules are NNs which, instead of taking dedicated feature functions as inputs, directly process atom positions and types and learn a representation of suitable features internally. They represent molecular structures as graphs, with nodes (vertices) v representing the atoms and edges e representing their interactions (either bonded or nearby nonbonded).[168–177] Each graph node (and sometimes also each edge) has a feature vector assigned that carries information on the atom (or bond) it represents, often starting with a one-hot encoding of the atom (bond) type. During training, these features are updated by graph convolutions that share parameters in such a way that permutation invariance or equivariance is maintained. The convolution kernels typically depend on distances or angular information between atoms, such that translational and rotational invariance or equivariance is maintained. The prediction of the desired molecular property is usually made in a final readout step, *e.g.*, by summing or averaging the feature vectors after the last convolution layer, by processing them with a densely connected network, or applying more elaborate aggregation functions.[169] In the following, we will discuss the network architectures that are used throughout this thesis in more detail.

An early GNN architecture is the edge-conditioned NN with a set2set readout function (enn-s2s) as proposed by Gilmer *et al.*[169] Within this approach, the undirected molecular graph G is initiated with atomic feature vectors $x_i = h_i^0$ of size d at the graph nodes, containing a set of chemical properties of the respective element (e.g., one-hot atom type, atomic number, hybridization state, etc.), and bond features e_{ij} at the graph edges (containing, *e.g.*, one-hot bond type and bond distance). The hidden states h_i^0 of the nodes then get updated T times during the message passing phase, which is defined in terms of message functions M_t that generate messages m_i^{t+1} as

$$m_i^{t+1} = \sum_{j \in N(i)} M_t(h_i^t, h_j^t, e_{ij}), \tag{2.18}$$

where $j \in N(i)$ denotes the neighbors j of node i in graph G. The message function M_t has the form $M(h_v, h_w, e_{ij}) = A(e_{ij})h_j$, where $A(e_{ij})$ is a dense NN that maps the edge vector e_{ij} to a $d \times d$ matrix. The atomic feature vectors h_i^t are updated using a gated recurrent unit[178] update function U_t: $h_i^{t+1} = U_t(h_i^t, m_i^{t+1})$. After the message passing phase, the graph information is accumulated using a learnable set2set operator,[179] whose output is then passed to a dense NN that computes the final prediction.[169]

SchNet is a popular GNN that uses a different approach to incorporate spatial information into the learning architecture.[180,181] Here, the node representations h_i^0 of size d are initialized randomly for each element type and subsequently adapted (learned) during training. Subsequently, in the atom-wise layers, the atomic feature vectors h_i^t are updated using atom-wise layers that have the form

$$h_i^{t+1} = \phi^t(h_i^t) = W^t h_i^t + b^t \tag{2.19}$$

with learnable weight matrices W of dimension $F \times d$ and biases b for each interaction step t. In the network's interaction blocks, the interactions of atom i with neighboring atoms j are incorporated as the convolution with all surrounding atoms:

$$h_i^{t+1} = (H^t * W)_i = \sum_{j \in N(i)} \phi^t(h_i^t) \circ \mathcal{W}(r_j - r_i). \tag{2.20}$$

Here, $\circ$ represents element-wise multiplication (Hadamard product), and $\mathcal{W}(r_j - r_i)$ is a filter-generating dense NN that maps the vector pointing from atom i to atom j onto an F-dimensional space in a way that preserves the known physical invariances of molecules and materials. After passing N interaction layers, a prediction block is used to obtain the final result. For the prediction of molecular properties, a sum-over-nodes operation (sum pooling) is used to obtain extensive properties and an average pooling to obtain intensive properties.[180,181]

The polarizable atom interaction neural network (PaiNN) was recently proposed as an extension of SchNet.[173] The PaiNN architecture uses equivariant representations over angular features to enable the incorporation of angular information into the learning process. Thus, the network receives additional structural data while retaining the ability to make rotation-invariant predictions by design.[173] PaiNN uses atomic scalar features s and atomic vector features h that are updated using stacked message-passing and update blocks. Inside the message passing blocks, the updates of s_i are calculated as

$$s_i^{t+1} = s_i^t + \sum_{j \in N(i)} \phi_s(s_j^t) \circ \mathcal{W}_s(r_j - r_i) \tag{2.21}$$

analogous to the definitions made for SchNet. The atomic vector features are updated as

$$h_i^{t+1} = h_i^t + \sum_{j \in N(i)} h_i^t \circ \phi_{vv}(s_j^t) \circ \mathcal{W}_{vv}(r_i - r_j) + \sum_{j \in N(i)} \phi_{vs}(s_j^t) \mathcal{W}_{vs}(r_i - r_j) \frac{r_i - r_j}{\|r_{ij}\|} \tag{2.22}$$

where the first half of the equation is a convolution with respect to the vector features,

and the second half is a convolution with respect to the scalar features using an equivariant filter. Subsequently, in the update block, the scalar and vectorial features are updated as follows:

$$s_i^{t+1} = s_i^t + a_{ss}(s_i^t, \|W_v h_i^t\|) + a_{sv}(s_i^t, \|W_v h_i^t\|)\langle W_u h_i^t, W_v h_i^t \rangle \qquad (2.23)$$

$$h_i^{t+1} = h_i^t + a_{vv}(s_i^t, \|W_v h_i^t\|)W_u h_i^t. \qquad (2.24)$$

Here, a_{ss}, a_{sv} and a_{vv} are learnable functions, and W_v, W_u are learnable linear projection matrices.[173,182] In the final readout step, as in SchNet, molecular properties are computed after sum- or average pooling over all graph nodes.

Chapter 3

Soft X-Ray Characterization of Highly Fluorinated Nanodiamonds

The contents of this chapter will be published in the article

<u>T. Kirschbaum</u>, A. Chemin, M. Bartkowiak, D. Wong, C. Schultz, A. Krueger, T. Petit, A. Bande. Soft X-Ray Spectroscopy Characterization of HF-fluorinated Nanodiamonds. *In preparation.*

Thorren Kirschbaum was lead author and sole first author in this project. The author contributions were as follows: T. Kirschbaum: X-Ray absorption spectroscopy and resonant inelastic X-ray scattering spectroscopy computations: acquisition, data curation, analysis, validation, visualization; manuscript writing. A. Chemin: X-Ray absorption spectroscopy and X-ray photoelectron spectroscopy experiments: acquisition, data curation, analysis, validation, visualization; manuscript writing. M. Bartkowiak: Resonant inelastic X-ray scattering spectroscopy experiments: acquisition, data curation, visualization. D. Wong: Resonant inelastic X-ray scattering spectroscopy experiments: acquisition, data curation, visualization. C. Schultz: Resonant inelastic X-ray scattering spectroscopy experiments: acquisition, data curation, visualization. A. Krüger: Sample prepraration, funding acquisition. T. Petit: Project conceptualization, funding acquisition, supervision, validation, manuscript writing. A. Bande: Project conceptualization, supervision, validation, manuscript writing.

3.1   Introduction

Pristine nanodiamonds are often covered by amorphous carbon clusters, fullerene-like shells, and/or heteroatoms.[15,183] Functionalization of their surfaces allows for direct tuning of the nanodiamonds' chemical, electrochemical, and fluorescent properties. In particular, fluorination has been the topic of recent interest to both achieve a uniform surface chemistry and open up pathways for further modification.[35,184,185] For applications in quantum information processing and magnetic sensing, surface fluorine can stabilize shallow nitrogen vacancy centers in nanodiamonds.[186,187] For chemical sensing, fluorination of B-doped diamond results in low electronic surface barriers.[188] Fluorination also provides a means of stabilizing the nanodiamonds' frontier orbitals,[189–191] allowing for tuning the photophysical properties. Furthermore, the stability and electronic properties of diamond electrodes can be modified by surface fluorination. Especially, fluorination leads to the highest electron affinity ever achieved for diamond materials.[192–195] Moreover, the enhanced physical properties of hydrogen- and fluorine-terminated nanodiamonds can be used for the fabrication of nanocomposite materials with unique nanodiamond characteristics.[196] For nanodiamond photocatalysis, combining the high stability of fluorinated nanodiamonds with the electron-rich nature of the F atoms may allow for a more efficient production of solvated electrons. Potentially, the incident light may directly excite the surface F atoms, instead of the diamond core, to allow for a facile ejection of the excited electrons into the surrounding water.

Fluorinated nanodiamonds (F-NDs) have been previously synthesized following different procedures.[35,68,197–200] Dubois and colleagues used pure F_2 after purification, which removed oxygen functionalities and sp^2 bound carbon, but rendered a comparatively low surface fluorine content on the nanodiamonds.[197,198] XAS in junction with solid-state nuclear magnetic resonance spectroscopy and vibrational spectroscopy was used as a key method to investigate the surface structure of these F-NDs.[198] In the procedure used by Osipov and colleagues, the purified detonation nanodiamonds were first oxidized under air and subsequently fluorinated with F_2.[200] This route yielded high F contents of 15–18 atom% and an almost complete F covering for the given nanodiamonds. Another route employed a mixture of 3:1 F_2/H_2 to generate HF for fluorination *in situ*, which is expected to effectively catalyze the surface fluorination.[35,68] The resulting nanodiamonds had fluorine contents of up to 8.6 atom%, while the surface amorphous carbon clusters were reduced, the hydrogen and oxygen functional groups largely removed and agglutinates broken up during the synthesis.[68]

In this chapter, we discuss the electronic structure of highly-fluorinated nanodiamonds obtained from liquid HF synthesis. The initial characterization of their surface chemistry *via* infrared, nuclear magnetic resonance and XPS indicated a fluoride content up to 11.8 wt.% (data not shown). In this chapter, we analyze the XPS, XAS and RIXS signatures of the F-ND sample. In particular, the XAS C K-edge is very useful to identify the carbon surface bonds, as the different surface groups signatures are more distinct than for the XPS. However, in contrast to XPS, these spectra are hardly quantitative due to the complexity of the involved transitions. XAS has been applied in previous studies to elucidate the electronic structure of carbon nanomaterials, including graphite fluorides and nanodiamonds.[70,198,201] From RIXS, we obtain complementary information on the local valence electronic states of the respectively probed element. Previous studies with RIXS or non-resonant XES have revealed new insights into fluorine bonding.[202,203]

The interpretation of the XAS and RIXS spectra is aided by DFT calculations using the DFT/ROCIS method.[130] We discuss the impact of different H/F mixtures on the XA spectra and analyze the spectral contributions of the different functional groups to the total spectra. Furthermore, we show how the LUMO shapes of hydrogen- and fluorine-terminated nanodiamonds change with varying surface functionalization.[190,204] Finally, we calculate the RIXS signatures of adamantane with different degrees of fluorination and reveal the physical origin of the observed spectral signals.

3.2   Methods

3.2.1   Experimental

The F-terminated nanodiamonds were provided by the group of Prof. Anke Krueger at the university of Würzburg (now university of Stuttgart). Briefly, the synthesis was performed as follows. Acid purified detonation nanodiamonds were purchased from Gansu Lingyun Corp. (P. R. China) and fluorinated according to the following procedure. The nanodiamonds were first annealed in vacuum at 170 °C for 8 hours and subsequently in high vacuum at 750 °C for 2 hours to remove adsorbed water and impurities from the surfaces. The nanodiamonds were then dispersed in anhydrous HF and cooled to -78 °C before adding elemental F_2. The suspension was then warmed to room temperature and stirred at 50 °C for 5 days. Finally, HF was removed in vacuum and the fluorinated nanodiamonds were dried in vacuum for 24 hours.

XAS and XPS measurements were performed at the high-resolution Russian-German beamline of the electron storage ring BESSY-II at Helmholtz-Zentrum Berlin (Germany) using an ultrahigh vacuum experimental station. The nanodiamonds were drop-casted onto a conductive doped Si substrate in a thin layer to limit charging effects. XAS measurements were conducted in the electron yield mode, where the incident photon energy was swept and the emitted electrons from the sample were simultaneously recorded under a 150 V screening potential. The energy resolution of the monochromator in the range of the C(1s) X-ray absorption edges (285 eV) was 70 meV, and the X-ray energy was calibrated against the energy positions of the first narrow peak of the C(1s) absorption spectrum of highly ordered pyrolytic graphite (285.45 eV). XPS was calibrated in accordance with the position of the reference highly ordered pyrolytic graphite peak (284.7 eV). Due to charging effects on the nanodiamonds, the position of the emission peaks shifted to higher energies. RIXS measurements were performed at the U41-PEAXIS beamline using the endstation PEAXIS of BESSY II. The RIXS spectra were acquired with an incident angle on the sample of 30°, a scattering angle 2θ of 60° and a slit of 20 μm. The instrument resolution was optimized to 130 meV at the F K-edge.

3.2.2 Calculation of X-Ray Absorption Spectra

The model system used for calculating nanodiamond XA spectra is a spherical nano-diamond with 35 C and 36 surface (H, F) atoms.[205] This system is large enough to capture the electronic properties of a nanodiamond, and small enough to keep calculation times reasonably short. The structures were optimized by DFT using the non-empirical meta-GGA TPSS functional[206,207] and Ahlrichs' def2-SVP basis set.[122,123] Grimme's third order atom-pairwise dispersion correction with Becke-Johnson (D3BJ) dampening[126] was used to include van-der-Waals interactions, and the RIJCOSX approximation[208] together with the appropriate def2-SVP/J auxiliary basis sets[124] was employed to speed up integral calculation. Numerical frequency analyses were performed to ensure that the structure optimizations converged.

For the calculation of XA spectra, the building block principle[201,209] was utilized to obtain the total molecular spectra from single-MO spectra. In this approach, each spectrum is calculated for only one core MO that can be assigned to a distinct atom or functional group. The total spectra are then obtained by adding up the spectral contributions of all single atoms. This concept is illustrated in figure A1.5 of appendix A1. Consequently, this approach allows to decompose the total spectra into the spectral contribution of a designated atom or group of atoms.

The spectra were calculated using the DFT/ROCIS method,[130,210] Becke's empirical hybrid functional B3LYP[211,212] and Ahlrichs' def2-TZVP basis set.[123] Three empirical values $c_1 = 0.18$, $c_2 = 0.20$, and $c_3 = 0.40$ are needed to scale down the two-electron integrals that occur in the CI matrix.[130,213] For each single-MO XA spectrum, 120 excitations were calculated, and the acceptor orbital space was restricted to the lowest 151 virtual orbitals. A Gaussian line broadening with a full width at half maximum of 1 eV was applied to include natural lifetime effects into the obtained line spectra

The DFT/ROCIS method is only able to model events of state transitions in the near-edge region of the XA spectra. The electronic transitions can also be calculated for higher excitation energies beyond the ionization threshold, but the ionization is not part of the calculations. In experiments, the samples are ionized at high incident X-ray energies, and the emitted electrons are scattered at the surrounding atoms, resulting in an interference pattern in the extended fine-structure region of the spectrum. There, signals from orbital transitions cannot easily be extracted from the measured spectra. Accordingly, we cut off the calculated spectra after the rising edge maxima and focus the interpretation on the rising edge and pre-edge signals only.

Initial XA spectra calculations for tetrahedrally coordinated carbon/fluorine systems were compared using the set of fluorinated methanes (CH_3F, CH_2F_2, CHF_3, CF_4) [214], graphite monofluoride $(CF)_n$ and adamantane $C_{10}H_{16}$ as a benchmark reference to calibrate and assess the accuracy of this method for these closely related systems (see appendix A1, tables A1.4 and A1.5). Based on this calibration, the XAS and RIXS spectra are systematically shifted by $+11.4$ eV and $+18.3$ eV for C and F K-edge spectra, respectively, to match the experimental data.

All calculations were carried out using the ORCA suite of programs. [215]

3.2.3   Calculation of RIXS Spectra

The same method (B3LYP-D3/def2-TZVP DFT/ROCIS) was used for calculating the RIXS at the F K-edge. The large amount of memory required for these calculations restricts the orbital range that can be employed, as well as the overall size of the nanodiamond. Instead of $C_{35}H_{36}$ and its derivatives, the smallest possible diamond crystallite, adamantane ($C_{10}H_{16}$) and its fluorinated derivatives were used. A maximum of 5000 excitations was calculated for each system. The range of core, valence, and virtual orbitals employed was adjusted depending on the F content. The respective number of involved orbitals and transitions for each RIXS spectrum is listed in the results section. These calculations will indicate the general shape of the respective RIXS spectra and serve the interpretation of the experiments. The effect of employing only a limited range of orbitals for RIXS calculations on the obtained spectra is discussed in appendix A1.

3.3   Results and Discussion

3.3.1   X-Ray Photoelectron Spectroscopy

Experimental

This section briefly summarizes the results of the XPS spectra analysis for the HF-fluorinated nanodiamonds. The spectra along with a more detailed discussion are given in the first section of appendix A1.

The XPS survey at $E_{h\nu} \leq 700$ eV confirms the presence of fluorine, and further reveals a small nitrogen contamination of the nanodiamonds which most probably originates from the detonation synthesis procedure.[15] The total fluorine content deduced from the survey is about 9.5 %, which translates to a surface F coverage of around 45 % assuming a mean particle diameter of 5 nm. The energy-resolved C(1s) XPS data suggests a surface CF coverage of ≤ 53 %, and indicates the presence of both CH and amorphous sp^2 carbon on the surface. Furthermore, XPS reveals the presence of oxygen on the sample, which is likely in the form of both adsorbed water and oxygen-containing functional groups on the nanodiamonds' surfaces.

3.3.2   X-Ray Absorption Spectroscopy

Experimental

Figure 3.1a shows the experimental XA spectra at the C K-edge of the HF-fluorinated nanodiamond sample. The large absorption above 289.5 eV is attributed to the excitation of the core C(1s) electrons to the diamond conduction band, and the dip at 302.5 eV corresponds to a second absolute gap in the diamond band structure, which are characteristic XAS features of diamond materials.[216] The absorption features in the pre-edge region shown in figure 3.1b originate from the excitation of C(1s) electrons to unoccupied surface states. The pre-edge region is fitted by an edge and Gaussian peaks in order to better determine the different surface states. The fitting parameters and further details on the fit are listed in appendix A1. In contrast to XPS, this fit yields a qualitative analysis only. A Gaussian error function is used to model the rising edge (hatched blue), whose parameters are determined using the XA of a H-terminated single crystal diamond as a reference. Subsequently, five Gaussian functions are used to fit the pre-edge signal. The spectrum in figure 3.1c corresponds to the carbon XAS pre-edge region minus the edge as quantified by the Gaussian fit. The peak at 285.35 eV is assigned to $\pi^*_{C=C}$ transitions from amorphous carbon patches.[57,217,218] The absorption at 286.03 eV is assigned to $\pi^*_{C=O}$ transitions from
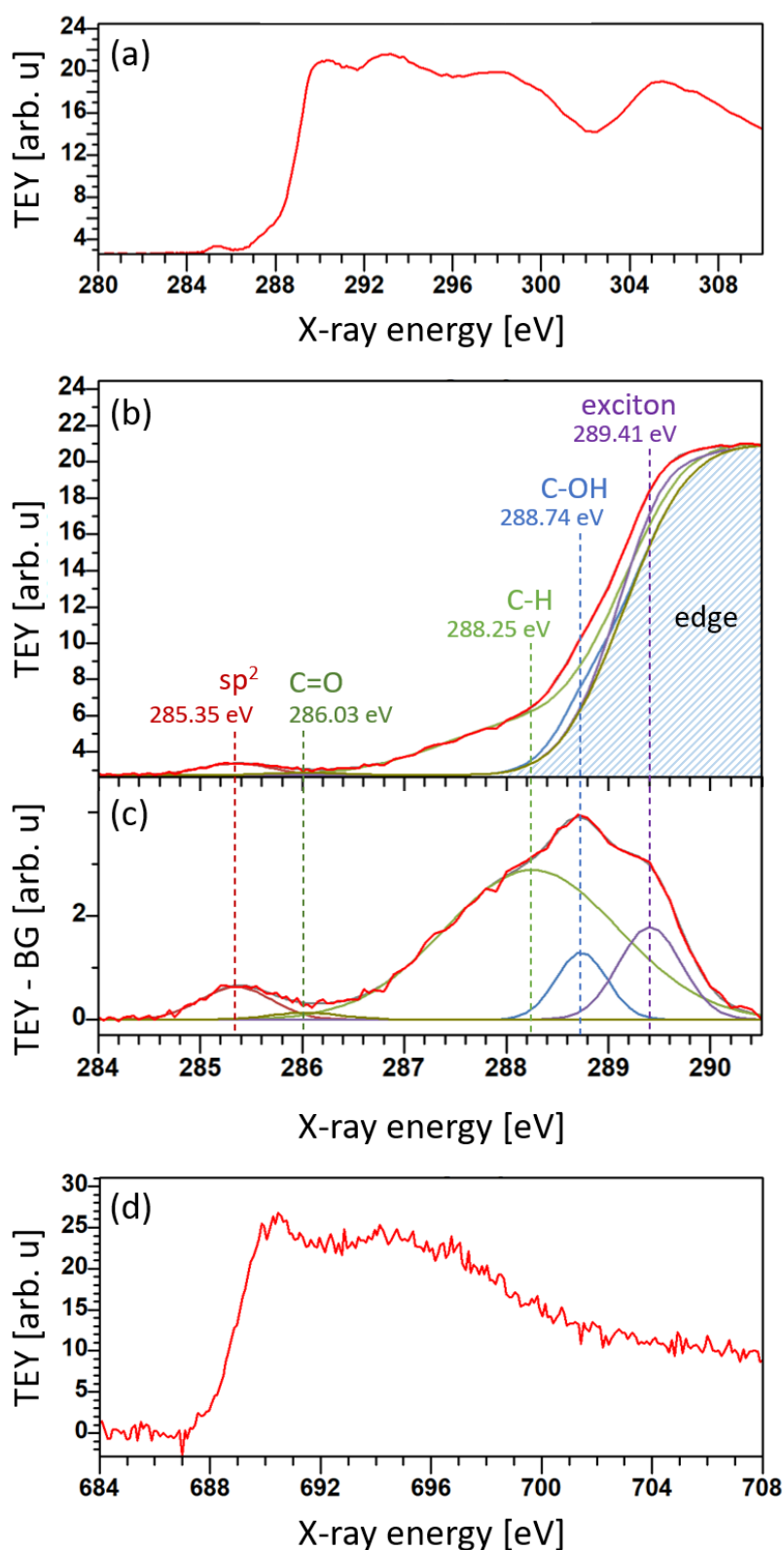
Figure 3.1: XAS spectra of the HF-fluorinated nanodiamonds, measured in total electron yield (TEY) mode. (a) C K-edge XAS of the F-NDs. (b) Zoom on the pre-edge features with the background (hatched area) and fit. (c) Zoom on the pre-edge features minus the background and fit. (d) F K-edge XAS of the F-NDs.

carbonyl groups.[219] The signal at 288.25 eV is attributed to the σ^* transition of CH carbons,[220] and the shoulder at 288.74 eV is attributed to hydroxyl carbons.[221] Finally, the core exciton that is typical for diamond C(1s) XA spectra is fitted at 289.41 eV. The XA on fluorinated nanodiamonds clearly shows a large amount of C-H surface states as well as sp^2 carbon bonds and a small amount of oxygen in the form of hydroxyl groups, which is consistent with the XPS analysis. Note that the C-F bonds are not visible at the C K-edge because they most likely appear at higher energies, overlapping with the carbon absorption edge as discussed in the following. As all carbon atoms (also from the nanodiamond core) contribute to the main absorption edge, surface states can only be isolated when their contributions appear in the pre-edge region.

Figure 3.1d shows the experimental XA spectrum at the F K-edge of the HF-fluorinated nanodiamond sample. The rising edge peaks at 690 eV with no pre-edge features being visible. This signature seems quite different from the previous work on the weakly F_2-fluorinated nanodiamonds. In this study, the main peak was found at the lower energy of 687.5 eV and followed by relatively weak features corresponding to transitions from fluorine into the π system above the ionization threshold.[198] The same lower-energy rising edge maximum at 687.5 eV has also been observed for graphite monofluoride.[70,198] The combined data suggests that in contrast to the F_2-fluorinated nanodiamonds, our HF-fluorinated sample has its fluorine moieties located on the diamond surface, but not on the amorphous carbon patches. Previous DFT calculations on perfluorocarbons demonstrated that CF_2 groups show comparable peaks around 688, 690 and 694 eV, while CF groups mainly contributed to a main peak at $\simeq$ 687 eV.[203]

Calculations for C$_{35}$X$_{36}$ (X=H,F)

The model systems used for the DFT/ROCIS calculations are based on a small nano-diamond structure C$_{35}$H$_{36}$, also known as superadamantane (figure 3.2a).[205] The nanodiamond has a tetrahedral symmetry and consists of 35 carbon and 36 surface atoms. The fully hydrogenated nanodiamond (H-ND) contains four different types of carbon atoms: 1 central C and 4 inner C (summarized into 5 inner C), 12 inner CH, 12 outer CH, and 6 CH$_2$. For the first set of spectra, starting from this H-ND, we gradually replace the surface hydrogen atoms with fluorine atoms at arbitrary positions. In this way, we obtain a set of randomly fluorinated nanodiamonds (F-NDs) which are labelled according to their surface F content: 1/36 F-ND, 1/6 F-ND, 2/6 F-ND, etc., up to the fully F-ND. The structures of the 1/2 F-ND and fully F-ND are shown in figure 3.2b and c, respectively.[222]
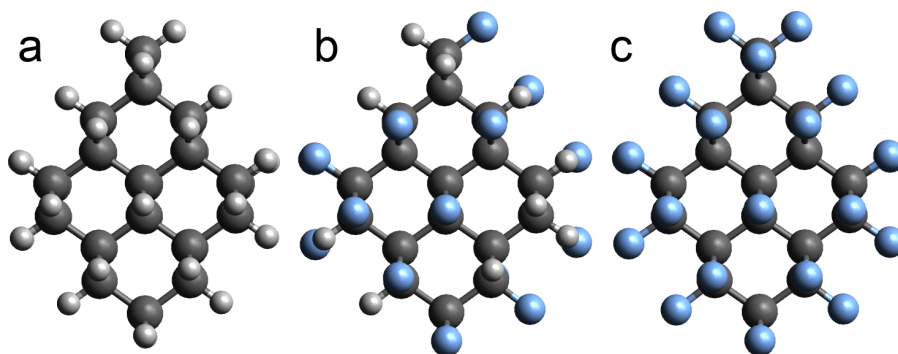

Figure 3.2: Structures of the (a) H-ND C$_{35}$H$_{36}$, (b) 1/2 F-ND C$_{35}$H$_{18}$F$_{18}$, and (c) F-ND C$_{35}$F$_{36}$. Colors: C (black), F (blue), H (light grey).

Regarding the fluorination pattern, the obtained spectra shift by up to $\pm$ 0.2 eV if the fluorine atoms are located at different random positions. For the 35/36 F-ND, the spectral shapes vary slightly, but the overall spectrum types are well retained.

The DFT/ROCIS-calculated C K-edge XAS rising edges of the randomly fluorinated nanodiamonds are shown in figure 3.3a. The rising edge of the H-ND peaks at 288.8 eV (grey). Upon adding a single F atom (1/36 F-ND, yellow), a pre-edge signal appears at 287.2 eV while the position of the edge maximum is nearly unchanged. Upon higher fluorination (1/6 F-ND, green, to 5/6 F-ND, violet) the shoulder becomes less pronounced and merges into the rising edge at 3/6 surface F content (medium blue) while the rising edge maximum is shifted to 289.0 eV. At 5/6 surface F content (dark violet), the rising edge is shifted to higher energies by approximately 0.5 eV and has become steeper as compared to the H-ND.

The rising edge then strongly shifts to higher energies at higher F contents. For the 35/36 F-ND (rose), a weakly pronounced shoulder at 288.9 eV and a marked shoulder
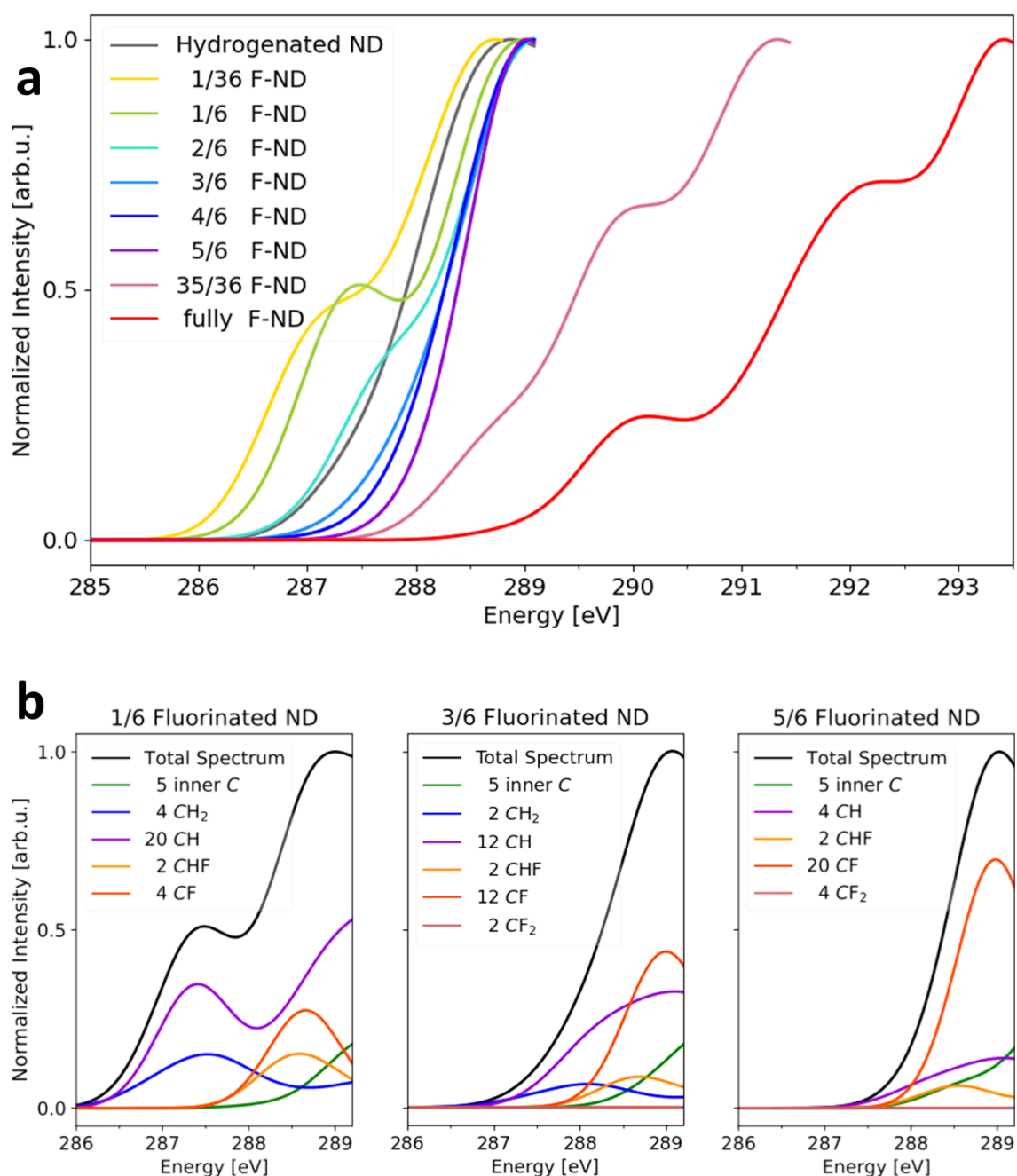
Figure 3.3: (a) DFT/ROCIS-calculated C K-edge XAS rising edges of the randomly fluorinated nanodiamonds $C_{35}X_{36}$ (X=H,F): Hydrogenated (grey), with increasing fluorine content (yellow to rose), and fully fluorinated (red). The F atoms replace the H atoms at random positions of the nanodiamond surface. (b) Composition of the XAS signals by functional groups of the 5/6, 35/36, and fully F-ND (from left to right).

at 290.0 eV are present, and the edge maximum is located at 291.3 eV. For the fully F-ND (red), the spectrum again shifts to higher energies and two marked shoulders at 290.1 and 292.2 eV are observed, while the edge maximum is placed at 293.4 eV. In experimental spectra, these signals of highly fluorinated nanodiamonds will most

likely be masked by the core carbons' signals which have no fluorine atoms in their direct vicinity. The rising edge maximum of untreated (H-terminated) nanodiamonds is placed at about 289 eV,[223] while the signals of surface carbon in our highly fluorinated nanodiamonds are placed at markedly higher energies. Accordingly, for highly fluorinated nanodiamonds, these signals will most likely merge into the extended regions of the spectra.

The C K-edge rising edge maximum of the HF-fluorinated nanodiamonds is located at 289.7 eV, very close to those of purely H-terminated nanodiamonds (290 eV).[223] This is in agreement with our calculations which suggest that the C K rising edge maximum of a hydrogenated/fluorinated nanodiamond will hardly change, except an (almost) complete fluorination is achieved.

As described in section 3.2, we can use the single-MO XA spectra to examine the contributions of the individual functional groups to the total spectra. In figure 3.3b, we decompose the total C K-edge spectra of the 1/6, 3/6, and 5/6 F-ND into the functional groups defined at the start of this section. The pre-edge peak of the nanodiamond with low F content can clearly be ascribed to the CH and CH_2 carbons' spectral contributions (violet and blue). With increasing degree of fluorination, the CH signal broadens and loses its double peak character. As more and more hydrogen atoms are replaced by fluorine, both the CH and CH_2 signals become weaker and shift to higher energies. Simultaneously, the total rising edges become less broadened and are increasingly defined by the CF carbons' spectral contributions.

In various experimental studies of H-terminated nanodiamonds a signal around 286.9–288 eV was observed and attributed to C-H σ^* transitions.[220,223–231] This is in excellent agreement with our finding of a shoulder at 287.5 eV for the 1/6 F-ND. We can thus verify the origin of this signal as resulting from surface hydrogen.

We also examined the functional groups' spectral contributions to the 35/36 and fully F-ND spectra (see appendix A1, figure A1.6). For the 35/36 F-ND, the first pre-edge peak and the rising edge maximum are defined by the 24 CF carbons, while the second pre-edge signal arises from the five inner carbons. For the fully F-ND, the single central carbon atoms defines the first pre-edge signal. Accordingly, this signal is expected be more pronounced in larger fluorinated structures with more inner carbon atoms. The second pre-edge signal and the edge maximum are mainly defined by the CF carbons' spectral contributions.

The DFT/ROCIS-calculated F K-edge XAS rising edges of the randomly fluorinated nanodiamonds are shown in figure 3.4a. The F K-edge XA spectrum of the 1/36 F-ND (yellow) consists of a steep rising edge that peaks at 688.1 eV. Upon higher fluorination, up to 5/6 surface F content (green to dark violet), the XA rising edges
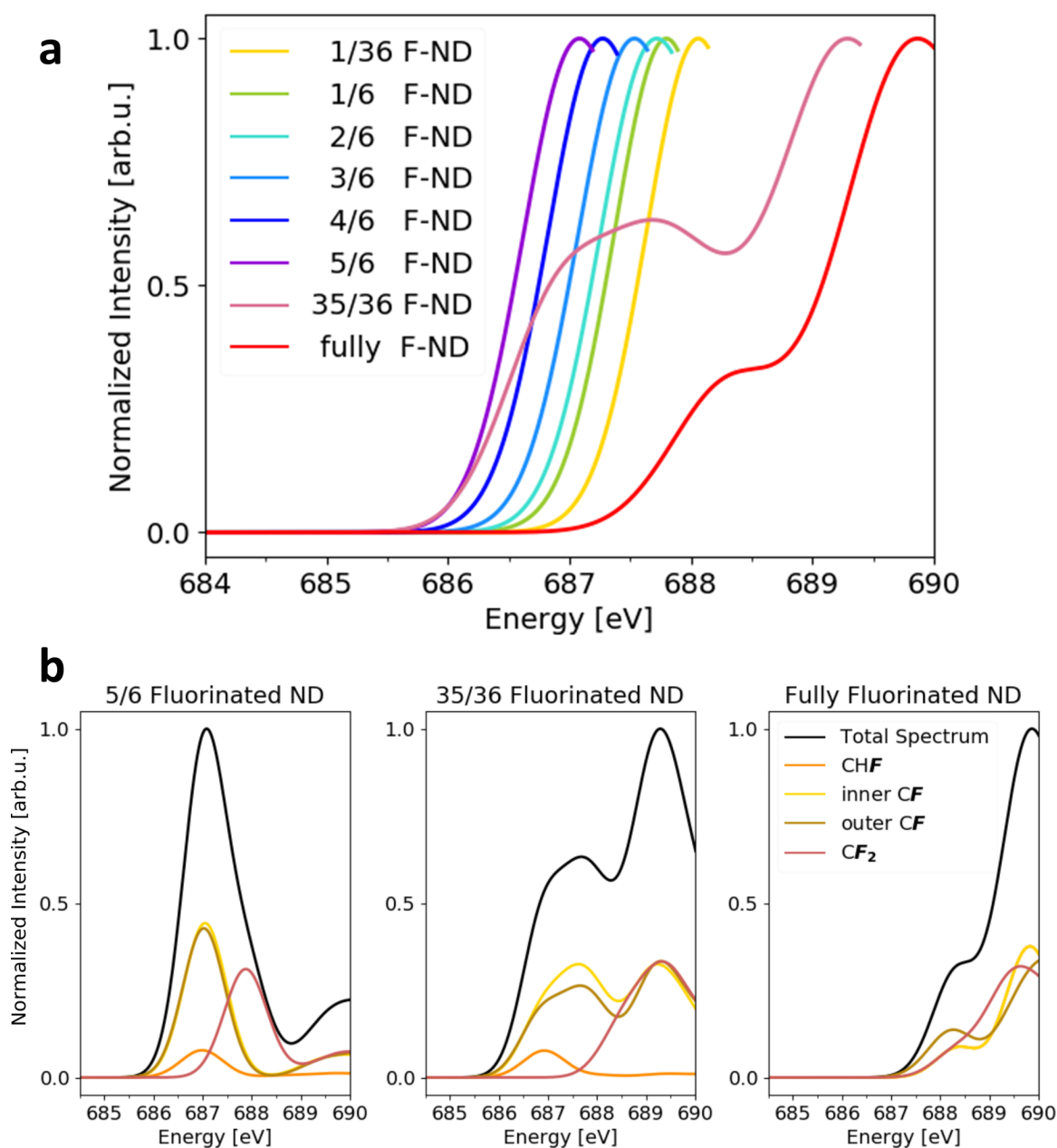
Figure 3.4: (a) DFT/ROCIS-calculated F K-edge XAS rising edges of the model nanodiamond with increasing fluorine content (yellow to rose), and fully fluorinated (red). (b) Composition of XAS signals by functional groups of the 5/6, 35/36, and fully F-ND (from left to right).

retain this shape and gradually shift to lower energies, each by 0.2—0.7 eV, such that the edge maximum of the 5/6 F-ND is located at 687.1 eV.

Surprisingly, for nanodiamonds with very high F content (35/36 and fully F-ND), the rising edges strongly shift back to higher energies. The 35/36 F-ND (rose) and fully F-ND (red) rising edge maxima are at 689.3 and 689.9 eV, respectively. Moreover, the spectral shapes change and a marked pre-edge feature appears for both spectra.

For the 35/36 F-ND, a broad signal is observed at 687.0–687.8 eV, which evolves into a shoulder at 688.4 eV in the fully F-ND. A similar behavior of shifted peak maxima in conjunction with the increased occurrence of pre-edge shoulders towards high surface F covering was observed for the C K-edge spectra (figure 3.3a).

We again use the single-MO XA spectra to examine the contribution of the individual functional groups to each of the total spectra. As shown exemplarily for the 5/6 F-ND in figure 3.4b (left), the spectra of the individual functional groups for the rising edges of up to 5/6 surface F content are very similar: All inner/outer CF and CHF fluorine signals are placed on top of each other and have equal shapes for a single structure. The CF_2 signal (if present) is at slightly higher energies in each case. For the spectra of the highly fluorinated structures (35/36 F-ND, rose, and the fully F-ND, red), the fluorine atoms of all functional groups contribute to the respective spectral shapes (only in the fully F-ND there is no CHF). The strong spectral change upon (almost) complete fluorination is mostly visible in the deformation of the CF fluorines' signals (yellow and ocre lines). In their spectra, a second peak at higher energies emerges at 689.3 and 689.9 eV (35/36 F-ND and fully F-ND, respectively), shifting the maxima of the rising edges to exactly these higher energies. Furthermore, the signal of the CF_2 fluorines (dark red lines) preserves its shape but is shifted by about $+1$ eV. Only the signal of the CHF fluorines (orange lines) remains unchanged. The strong shift of the spectrum when going from 35/36 to full F coverage mostly arises from the shift of the CF fluorines' signals to higher energies. Contrary, the signal position of the CF_2 fluorine barely changes at this point. The CHF signal vanishes, because this functional group is removed.

Calculations for O- and F-functionalized C$_{35}$H$_{36}$

We here consider the XA spectra of singly oxidized, as well as singly oxidized and fluorinated nanodiamonds, again using the C$_{35}$H$_{36}$ nanodiamond as a base structure. Their structures are depicted in figure 3.5. As shown in figure 3.3a, the C K rising edge of a singly fluorinated nanodiamond has a shoulder at 287.2 eV and its maximum at 288.8 eV. The spectrum strongly changes when an oxygen atom is present next to the CF. The corresponding single-atom XA spectra are displayed in figure 3.6a.
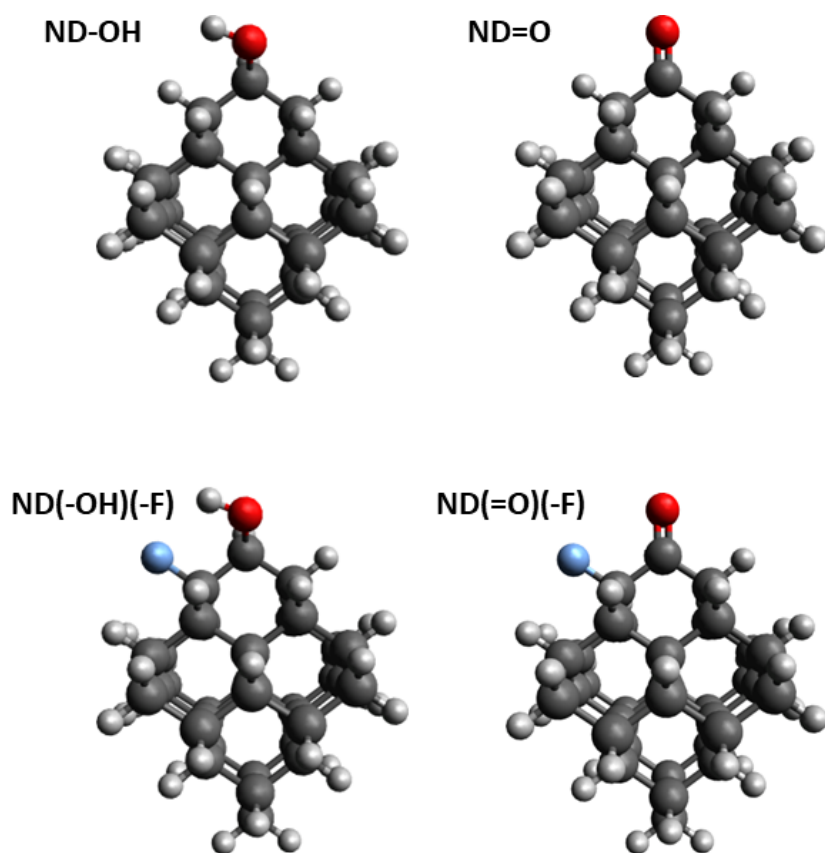

Figure 3.5: Structures of the C$_{35}$H$_{36}$ decorated with single hydroxyl oxygen or keto oxygen and fluorine moieties. Colors: C (black), O (red), F (blue), H (light grey).

The attachment of oxygen atoms results in strong, non-systematic shifts of the rising edges towards 286–290 eV. For the experimental sample, we expect the spectrum to be dominated by signals from the first few carbon layers with rather small contributions of CO and CO/F carbons to the total spectrum, because the coverage of oxygen is expected to be rather low. However, the computational data presented here indicates that the full C K-edge XA spectra of nanodiamonds with diverse surface coverages will be very rich and complex, which is reflected in the near-edge fine structure (*cf.* figure 3.1).
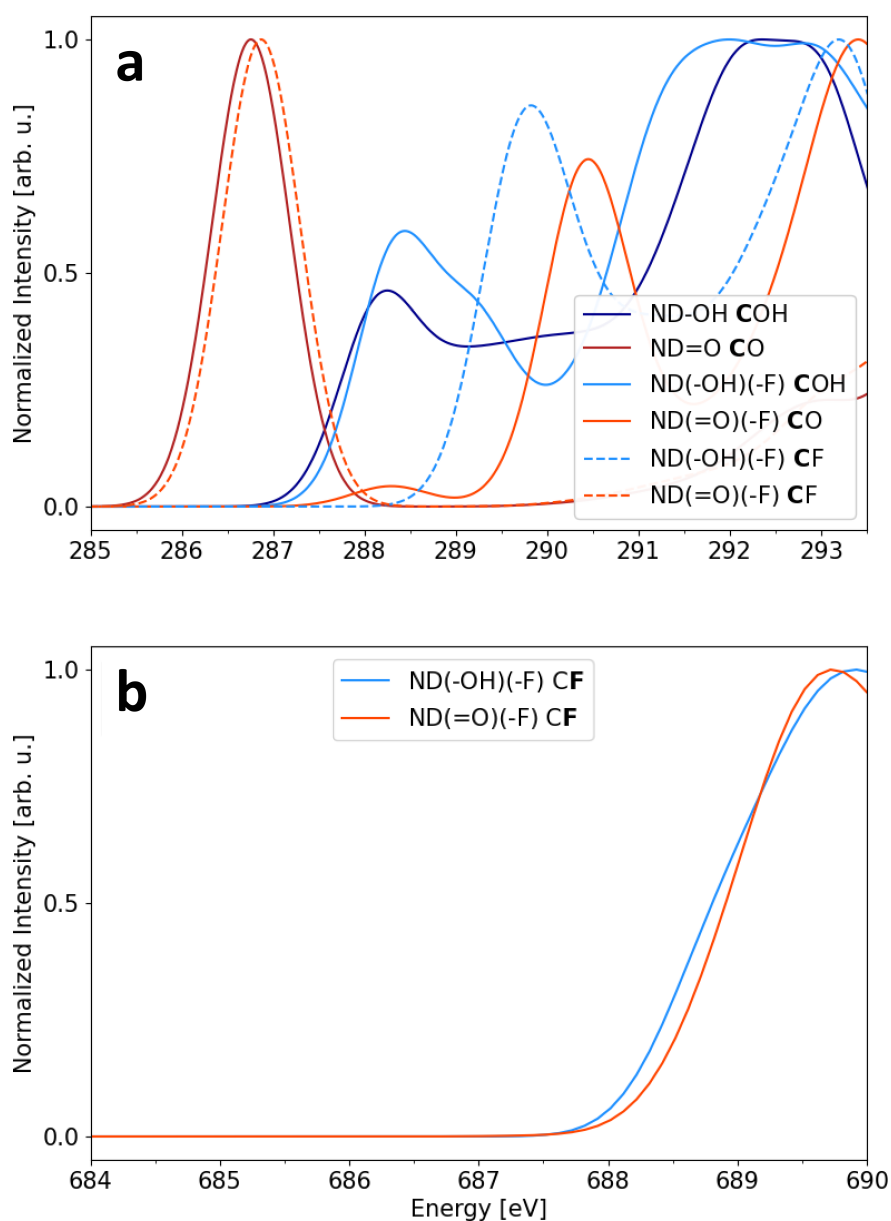
Figure 3.6: The DFT/ROCIS-calculated single-atom spectra of the partially oxidized and fluorinated $C_{35}H_{36}$ (structures in figure 3.5) at the (a) C K-edge and (b) F K-edge.

The F K-edge single-atom XA spectra of the oxidized and fluorinated nanodiamonds are shown in figure 3.6b. The fluorine rising edges shift to higher energies by +1.7 eV upon the introduction of hydroxyl or carbonyl oxygen next to the F atom, resulting in featureless rising edges with their maxima at around 689.8 eV. This result is in excellent agreement with our experimental data, where the rising edge maximum is located at 690 eV (figure 3.1d).

LUMO shapes of H-/F-terminated nanodiamonds

The frontier orbitals play a crucial role in the electron excitation and emission processes from nanodiamonds. For spherical, H-terminated nanodiamond, the LUMOs are known to have unique, atomic-orbital-like shapes. [204,232] The LUMOs are typically spread out spherically over the respective structure, resembling atomic s-orbitals (*cf.* figure 3.7a). The next highest MOs, denoted as LUMO+n (n=1,2,3,...), are shaped like atomic p-orbitals (n=1–3), d-orbitals (n=4–9), etc. We here discuss the LUMO shapes of the randomly fluorinated nanodiamonds (figure 3.7a-f), as well as the half fluorinated nanodiamond $C_{35}F_{18}H_{18}$ with the fluorine densely packed at one side of the nanodiamond (1/2-side F-ND, figure 3.7g). The corresponding frontier orbital energies are presented in appendix A1, figure A1.7.
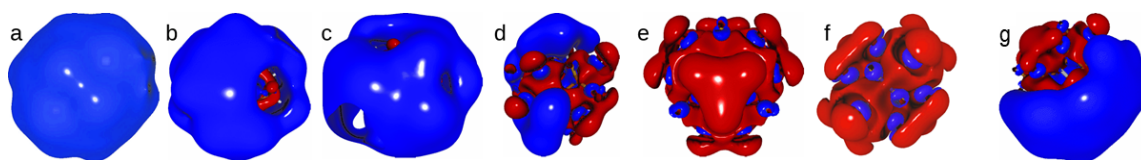

Figure 3.7: LUMO shapes of the hydrogenated and fluorinated nanodiamonds. (a) H-ND, (b) 1/36 F-ND, (c) 6/36 F-ND, (d) 18/36 F-ND, (e) 35/36 F-ND, (f) fully F-ND, (g) 1/2-side F-ND. Contour surfaces of orbital amplitudes ±0.0062.

The H-ND has a 1s-atom-like orbital extending over the whole surface of the nanodiamond. This shape is mainly preserved and only slightly disrupted if one or a few fluorine atoms are added. The LUMO shapes of the 35/36 F-ND and the fully F-ND are still delocalized over the whole structure, but have a very different shape with a less spread-out character and more nodal planes being visible. At half surface F content, both the atomic-s-like LUMO type and the F-ND LUMO type occur concomitantly. If the fluorine content is spread out over the structure (figure 3.7d), the two orbital types are interspersed according to the location of the fluorine and hydrogen surface patches. If the nanodiamond is densely covered by hydrogen and fluorine on either side (figure 3.7g), the LUMO is sharply separated into half H-ND and half F-ND character.

These findings are in line with previous investigations on the LUMO properties and shapes of H- and F-terminated diamondiods and nanodiamonds. [190,204,232] Szilvási and Gali presented the LUMO shapes of hydrogen- and fluorine-terminated diamondoids (adamantane, diamantane, triamantane) obtained from DFT calculations, comparing the orbital characteristics of 0, 25, 50, 75, and 100 % fluorine-covered diamondoids with the fluorine being densely packed at one side of the molecule in all cases. [190] With increasing surface F content, the LUMO shapes gradually develop from

a H-ND LUMO type to a F-ND LUMO type. Similar to our results, the LUMOs of the fully F-covered diamondoids were shown to be highly nodal and extend throughout the whole respective system.

It was previously argued that the characteristic LUMO shapes of H-terminated nanodiamonds only occur for highly symmetric nanodiamonds with complete H coverage.[204] However, the results presented here give a different picture: Upon addition of a small number of heteroatoms on the surface (1 or 6 fluorines), the LUMO shapes are mainly preserved and only slightly disrupted at the C-F sites. They further underline that F-termination can assist in binding excitons as well as excess electrons to the nanodiamond due to the decreased LUMO energies, as also found by Szilvási *et al.*[190]

3.3.3   Resonant Inelastic X-Ray Scattering Spectroscopy

Experimental

Figure 3.8a shows the experimental F K-edge RIXS map obtained for the HF-fluorinated nanodiamonds as a function of energy loss, and figure 3.8b shows selected RIXS spectra and the non-resonant XES spectrum measured at $E_{h\nu}$ = 720 eV (violet line) as a function of emitted photon energy. The RIXS spectrum recorded at $E_{h\nu}$ = 688.8 eV (bright green line) corresponds to the excitation energy at the XAS rising edge maximum. The spectra obtained at different excitation energies all consist of one sharp asymetric peak at 676.5 eV with a shoulder towards higher energies, and only differ in their relative intensities. The non-resonant XES signal has a similar signature with a less intense main peak (violet line in figure 3.8b). Glans *et al.* have found that the XES profiles of CH_2F_2, CHF_3 and CF_4 all consist of asymmetric signals similar to the ones obtained for the F-NDs, but the presence of CH_3F moieties on the F-ND sample can be ruled out, because the XES signature would then exhibit two well separated peaks at about 675 and 678 eV, which is obviously not the case. [202] These RIXS results therefore suggest that the majority of surface functional groups on the F-NDs are composed of multiple fluorine atoms. A finer interpretation of the resonant features will be achieved by comparison with theoretical calculations.
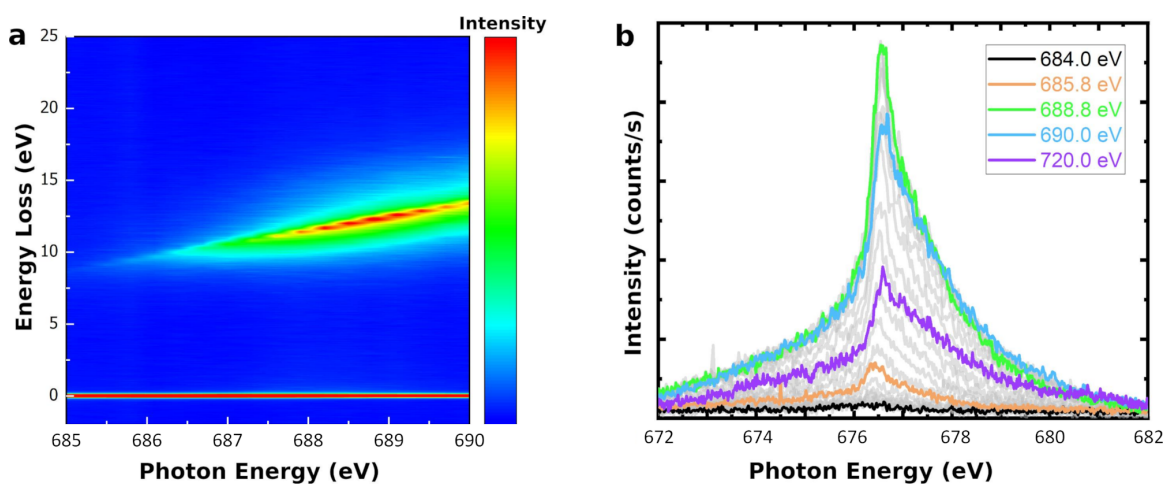

Figure 3.8: (a) RIXS F K-edge map of the HF-fluorinated nanodiamonds. The energy loss (difference between incident and emitted photon energy) is plotted against the incident photon energy (both in eV). The red line at 0 eV energy loss is the elastic scattering signal. (b) RIXS F K-edge spectra as a function of the emitted photon energy of the HF-fluorinated nanodiamond recorded at excitation energies $E_{h\nu}$ = 684.0 eV (black), 685.8 eV (orange), 688.8 eV (green), 690.0 eV (blue), 720.0 eV (violet). The light gray lines represent the spectra at further excitation energies corresponding to the RIXS map.

Calculations for fluorinated adamantanes

The RIXS process involves the excitation of a core electron into the multitude of unoccupied (virtual) MOs, and the subsequent relaxation of valence electrons into the core hole. To fully account for the possible processes that may occur within a larger nanodiamond structure, a huge orbital space would need to be included in each RIXS calculation. However, this is unfeasible in terms of computational cost. We therefore focus our investigations on the smallest diamondoid, adamantane ($C_{10}H_{16}$), which has the same base structure and bonding situation as any larger nanodiamond. For each spectrum, limited sets of core, valence and virtual orbitals were employed to make the computations feasible. To evaluate the reliability of the results in such a truncated orbital space, reference calculations with a larger number of orbitals were performed on small fluorocarbons (see appendix A1, figure A1.8). [222]

We use adamantane with four different fluorination patterns for the understanding of the experimental F K-edge RIXS spectrum of the HF-fluorinated nanodiamonds. Three structures and their respective RIXS spectra are shown in figure 3.9, where the adamantane is either (a) singly fluorinated, (b) has a CF group that is surrounded by three CF_2 carbons, or (c) carries a single CF_2 group. For the structure with CF + 3 CF_2, the RIXS spectrum is calculated only for excitation of the core MO at the central CF fluorine. Furthermore, the spectra obtained for fully fluorinated adamantane are shown in appendix A1, figure A1.9 alongside the RIXS maps of fluorinated methanes (figures A1.10–A1.13).

These model systems represent only a fraction of the fluorination patterns that can potentially occur in a real sample. Accordingly, we do not attempt to directly compare and discuss the individual signals in great detail. We are, however, able to reproduce the overall signal positions and shapes that are observed in the experimental spectrum.

The RIXS F K-edge map of the singly fluorinated adamantane is shown in figure 3.9a. The calculation included all 31 valence orbitals and the 62 lowest virtual orbitals. The first major signal (red) is visible at around 688.2 eV excitation energy and 12 eV energy loss. At higher incident energies, further signals with linearly increasing energy losses are present. This corresponds to an inelastic scattering signal at around 676.2 eV, independent of the excitation energy. The observed spectral shape reproduces the experimental findings (figure 3.8), but the calculated signals are broader and have no higher-energy shoulders.
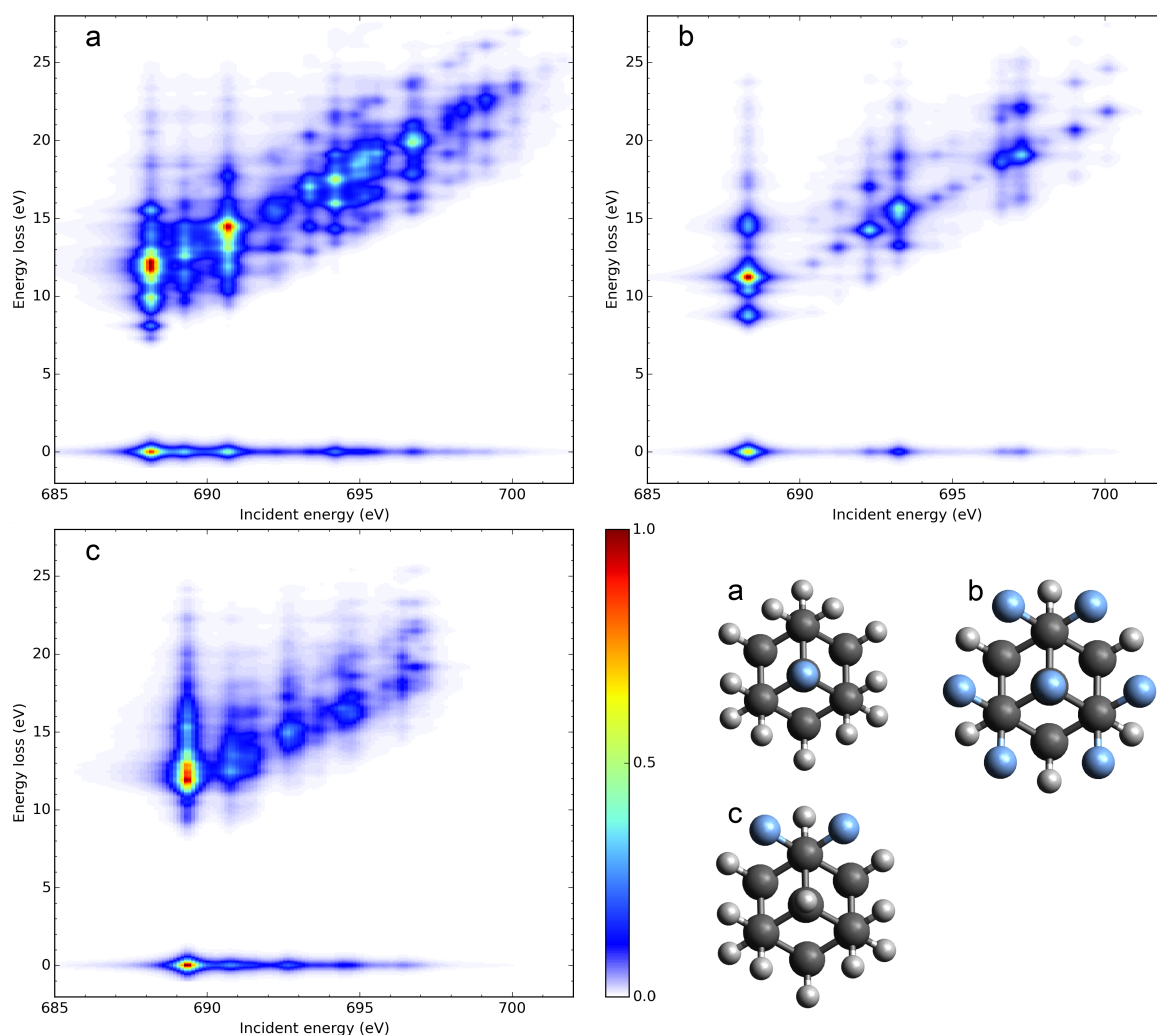
Figure 3.9: DFT/ROCIS RIXS F K-edge maps of fluorinated adamantanes as a function of incident energy and energy loss. The color scale indicates signal intensity from low (blue) to high (red) in arbitrary units according to the intensities being normalized to (0,1) in all spectra. Corresponding structures are shown in the bottom right. (a) Singly fluorinated adamantane, (b) fluorinated adamantane with one CF moiety surrounded by CF_2 and H-terminated otherwise, and (c) adamantane with one CF_2 moiety.

In the second molecule (figure 3.9b), one CF moiety is surrounded by three CF_2 carbons. The lowest MO is well localized at the central CF fluorine. We calculate the spectrum from only this F 1s orbital, neglecting the contributions of excitations from the surrounding CF_2 fluorines. Here, we restrict the orbital space to all 49 valence orbitals and the 49 lowest virtual orbitals. Figure 3.9b shows the resulting RIXS F K-edge map. The main signal is located at 688.3 eV excitation energy and 11.2 eV energy loss. Again, the same pattern of increasing energy loss upon higher-energy excitation energies is observed, corresponding to an inelastic scattering signal at around 677.1 eV. In contrast to the previous spectrum (figure 3.9a), the signals are

narrower and less intense, which might be attributed to the lower number of virtual orbitals employed for the calculation.

From the third molecule, we obtain the RIXS F K-edge spectrum of adamantane with one CF_2 group (figure 3.9c). We here included both F 1s orbitals, all 35 valence orbitals and the 35 lowest virtual orbitals. The main feature at 689.3 eV with an energy loss of 11.9 eV corresponds to an inelastic scattering signal at 677.4 eV. As observed before, the energy loss linearly increases with higher incident energies, resembling the experimental result.

The RIXS F K-edge features occurring upon excitation of the CF fluorines in fully fluorinated adamantane are given in appendix A1, figure A1.9. This molecule has a much larger set of orbitals, so the calculations are less exhaustive compared to those discussed above, however, they again all show the same trend of linearly increasing energy losses with the inelastic scattering signals being located at 677.3 eV.

Furthermore, we calculated the RIXS maps of fluorinated methanes, which are also tetrahedrally coordinated carbon systems, albeit much smaller than the adamantane. The spectra are shown in appendix A1, figures A1.10–A1.13. The spectra of tri- and tetrafluoromethane show the same pattern as those of the fluorinated adamantanes, however, different spectral shapes are observed for the singly and doubly fluorinated species. This result advocates a high degree of fluorination on the HF-fluorinated sample.

Overall, all computed spectra of differently fluorinated adamantanes as well as highly fluorinated methanes resemble the experimental spectrum of the HF-fluorinated nanodiamond. Only, the calculated absorption features are much broader than expected from the experiment.

Physical origin of the RIXS signature

During the RIXS process, the systems are first excited into intermediate, core-excited states, and subsequently relax into final, valence-excited states. The DFT/ROCIS calculations can be analyzed to reveal which intermediate and final states contribute to each of the features.

In all cases, the final states that are reached are strongly mixed and no single final state ever dominates. However, for the main peak of each adamantane spectrum (around 689 eV incident energy and 12 eV energy loss) a small number of 1–3 intermediate states dominates upon the initial excitation. These states are analyzed by computing the corresponding natural difference orbitals, which are defined as the eigenvectors of the difference density matrix between ground and excited states and

allow to visualize the excitation from the core MO to the virtual orbital. [233]

Interestingly, the natural difference orbitals that correspond to the respective intermediate states are very similar for all systems. They are shown for singly fluorinated adamantane in figure 3.10, and further natural difference orbital plots can be found in appendix A1, figures A1.14–A1.19. In each case, the excitation occurs from the F core orbital (left) into a characteristic orbital that is located at the fluorine and its neighboring carbon atom, resembling an antibonding CF orbital (right). The similarity of the natural difference orbitals of all systems for this peak together with the similarity of the calculated RIXS maps of all systems indicates that the RIXS F K-edge spectra of different fluorinated nanodiamonds all originate from a F(1s) σ^* transition and will always have a similar shape.
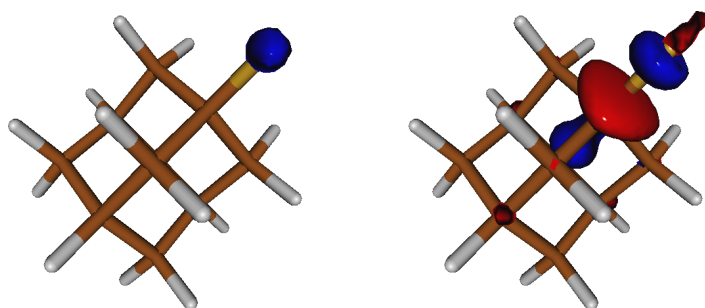

Figure 3.10: Natural difference orbitals corresponding to the main peak at 688.2 eV incident energy for the singly fluorinated adamantane (see figure 3.9a). The excitation occurs from the orbital shown on the left to the orbital shown on the right.

3.4   Conclusions

In this chapter, we investigated a sample of HF-fluorinated nanodiamonds using combined XPS, XAS and RIXS experiments supported by DFT/ROCIS-based XAS and RIXS computations. The XPS data suggests a fluorine concentration of 9.5 atom% and a CF surface coverage of about 50 %, and confirmed the presence of nitrogen impurities, oxygen moieties, CH and sp^2 carbon on the nanodiamond. The XAS data indicates that the HF-fluorinated sample has its fluorine moieties located on the diamond cores, but not on the amorphous carbon patches.

The calculations show that once a very high degree of fluorination is reached, the XAS rising edges strongly shift to higher energies. The computations allowed to decompose the spectra into the contributions of the individual functional groups, confirming that the low-energy C K-edge XAS shoulder of nanodiamonds with high hydrogen coverage can clearly be attributed to hydrogenated carbons. The position of the rising edge is otherwise dominated by the fluorine-containing functional groups and remains largely unchanged at lower levels of fluorination. The F K-edge XA spectra consist of featureless rising edges which are slightly shifted to lower energies upon increasing fluorination, and then strongly shift back to higher energies at (almost) complete fluorination. These spectra are dominated by the signals originating from the CF and CHF groups. The results indicate that fully fluorinated nanodiamonds will have markedly different electronic properties as compared to partially fluorinated particles. Upon addition of oxygen to the system, the XAS features shift strongly and non-systematically, rendering complex C K-edge spectral signatures.

The experimental RIXS F K-edge spectrum consists of a single signal that linearly shifts to higher energy losses with increasing incident energies. The DFT/ROCIS calculations reveal that the same spectral signature can be expected for a range of H/F-terminated tetrahedral carbon structures with different degrees of fluorination. For all investigated structures, the main spectral signal was found to correspond to a selective excitation of the F 1s electron into an anti-bonding CF orbital. For future investigations of fluorinated carbonaceous materials, XAS appears to provide higher information content compared to RIXS spectroscopy at the F K edge and should therefore be preferred for analytical experiments.

Chapter 4

Surface Transfer Doping at Nanodiamonds

The contents of this chapter were published in the following articles:

T. Kirschbaum, T. Petit, J. Dzubiella, A. Bande (2022). Effects of oxidative adsorbates and cluster formation on the electronic structure of nanodiamonds. *J. Comput. Chem.* 43, 13, 923–929. https://doi.org/10.1002/jcc.26849

Thorren Kirschbaum was lead author and sole first author in this project. The author contributions were as follows: T. Kirschbaum: Data acquisition, data curation, analysis, validation, visualization, manuscript writing. T. Petit: Project conceptualization, supervision, validation, manuscript writing. J. Dzubiella: Project conceptualization, funding acquisition, supervision, validation, manuscript writing. A. Bande: Project conceptualization, supervision, validation, manuscript writing.

F. Buchner, T. Kirschbaum, A. Venerosy, H. Girard, J.-C. Arnault, B. Kiendl, A. Krueger, K. Larsson, A. Bande, T. Petit, C. Merschjann (2022). Early dynamics of the emission of solvated electrons from nanodiamonds in water. *Nanoscale* 14, 46, 17188–17195. https://doi.org/10.1039/D2NR03919B

Thorren Kirschbaum was lead author for the theory part of this paper and second author in this project. The author contributions were as follows: F. Buchner: data curation, investigation, validation, visualization, manuscript writing. T. Kirschbaum: software, validation, visualization, manuscript writing. A. Venerosy: investigation. H. Girard: investigation. J.-C. Arnault: conceptualization, funding acquisition, project administration, resources. B. Kiendl: investigation. A. Krüger: conceptualization, funding acquisition, project administration, resources, supervision, manuscript writing. K. Larsson: investigation, funding acquisition, project administration, manuscript writing. A. Bande: conceptualization, investigation, software, supervision, validation, manuscript writing. T. Petit: conceptualization, funding acquisition, investigation, project administration, supervision, visualization, manuscript writing. C. Merschjann: conceptualization, data curation, investigation, resources, validation, visualization, manuscript writing.

Thorren Kirschbaum was lead author and sole first author in this project. The author contributions were as follows: T. Kirschbaum: Project conceptualization, data acquisition, data curation, analysis, validation, visualization, manuscript writing. X. Wang: Funding acquisition, data acquisition, validation, manuscript writing. A. Bande: Project conceptualization, funding acquisition, supervision, validation, manuscript writing.

4.1 Introduction

Diamond is a stable and inert material due to a very rigid lattice structure of sp³-coordinated carbon. However, when shrinking the material's size, surface effects dominate and the electronic interactions of nanodiamonds with the environment can strongly alter their properties. Applications in catalysis and biomedicine critically rely on the unique electronic properties of the nanodiamonds, hence, effects of the condensed environment are of paramount importance in these fields. [17,234,235]

The interaction of bulk diamond surfaces with aqueous adsorbates has been extensively researched with a strong focus on surface transfer doping. [80,81,236] In their landmark paper, Chakrapani *et al.* established that in the presence of air-equilibrated water, electrons move from the diamond surface into the liquid phase where they drive the redox reaction $O_2 + 4\,H^+ + 4\,e^- \leftrightharpoons 2\,H_2O$. [81] When oxygen is purged from the water, no electron flow occurs. However, if the water pH is lowered, electrons again move from the H-terminated diamond surface into the acidic water to reduce the excess protons. Furthermore, ozone is known to effectively remove inhomogeneities from nanodiamonds and obtain a fully O-functionalized surface, for which charge transfer effects my play a key role. [37] Surface transfer doping has concurrently been studied in many experimental[82–87] and theoretical works, [88–95] however, until recently, such investigations were missing for nanodiamonds.

In a previous study, Aranifard and Shojaei investigated the interaction of neutral, protonated and deprotonated water clusters with the bare and functionalized nanodiamond C_{35}. Strong hydrophobic interactions were found between the bare C_{35} (without surface saturation and dangling surface carbon bonds) and aqueous OH^-, and a significant rearrangement of electron density was observed when charged water clusters were in contact with the bare C_{35}. [23]

Surface modification of diamond can dramatically alter its electronic properties (electron affinity, work function, reactivity, etc.) without modifying the bulk material. Due to their large surface areas, these effects are amplified for nano-structured diamond materials. For example, nanodiamonds covered by hydrogen, hydroxyl or fluorine species will have a radically different surface chemistry and distinct surface electronic properties. [28,185,195,237] Furthermore, the introduction of dopants allows for targeted changes of nanodiamond's electronic structure. [45,58,238,239] The present study extends the theoretical investigations on surface transfer doping by quantifying and explaining the charge migration between nanodiamonds and aqueous oxidative adsorbates for different nanodiamond sizes, surface modifications, dopant atoms and adsorbate molecules.

We start by quantifying the effect of surface transfer doping for the oxidative adsorbates $H_2O \cdot H_2O$, $H_3O^+ \cdot H_2O$, $O_2 \cdot H_2O$ and $O_3 \cdot H_2O$, as these are the most abundant species in water and were already investigated in previous work on the diamond (100) surface.[92] Moreover, we analyze the charge transfer towards $O_2 \cdot H_2O$ for nanodiamonds of different sizes (35–147 carbon atoms), surface terminations (H, OH, F), surface patterns (full or partial coverage by a functional group or amorphous carbon) and dopant atoms (B, Si, N). In addition, we discuss the excited states of a small nanodiamond with different adsorbates present in its solvation shell, and the analyze charge transfer from the nanodiamond towards the respective adsorbate in the context of photocatalysis.

Furthermore, it is known from experiments that nanodiamonds tend to form clusters and self-assembled networks in water.[240,241] Some computational studies investigated the aggregation behavior[240] and stability[242] of these clusters, but until recently, the effects of clustering on the electronic structures of nanodiamonds and diamondoids had been largely unexplored. For the diamondoids, experimental data on their electronic structure (*i.e.*, the optical gap) is available, however, different results have been obtained from different experimental techniques.[243–245] A detailed analysis of the effects of cluster formation on the electronic structure of diamondoids and comparisons to experimental data are given in appendix A2.

4.2 Methods

The structures of adsorbates at nanodiamonds were optimized by DFT using the PBE general purpose functional,[246] Ahlrich's def2-SVP basis set,[122–124] and Grimme's three-body dispersion correction with Becke-Johnson dampening (D3BJ).[126] For the optimization of water shells around superadamantane, we instead used the revised PBE functional revPBE,[247] which is known to yield reasonable water structures,[248] with the same basis set and dispersion correction. For these systems, the optimizations were run with loose convergence criteria due to the shallow potential energy surfaces. Single-point calculations for quantifying the surface transfer doping were carried out using the TPSSH hybrid meta-GGA functional,[208,249,250] the def2-TZVP triple-zeta basis set and D3 dispersion correction. We employed the conductor-like polarizable continuum implicit solvation model to mimic the effects of an extended aqueous environment,[131] and we used the fractional occupation number weighted electron density method to allow for fractional occupation numbers of molecular orbitals at finite temperatures.[251] The charge transfer was quantified using Hirshfeld population

analysis,[252] which generally yielded the same qualitative results as the Loewdin analysis.[253]

Excited states were calculated by time-dependent DFT using the diffuse def2-SVPD basis set, D3 dispersion correction, and the long-range corrected CAM-B3LYP hybrid functional.[254] This level of theory has previously been employed successfully for calculating the excited states of similar systems as studied here.[255–257]

The diamondoid structures presented in appendix A2 were optimized using the TPSSH functional, the minimally augmented ma-def2-SVP basis set and D3 dispersion correction. For the structures with up to 100 atoms, convergence of the optimizations was checked by performing numerical frequency analyses. The diamondoid HOMO-LUMO gap energies were corrected according to the zero-point energy gap renormalizations (ZPR) published by Han *et al*.[258] For the dimers and higher adamantane clusters, no ZPR corrections have been calculated explicitly, and we instead use the respective monomer corrections as a proxy. For these calculations, the errors induced by basis set superposition were found to be negligible.

All DFT calculations were carried out within the ORCA suite of programs.[215] Natural transition orbitals were calculated using Multiwfn.[259]

4.3   Results and Discussion

4.3.1   Homogeneous Nanodiamonds

The nanodiamond $C_{84}H_{64}$ is used as the base structure for the investigations presented here. This structure has tetrahedral symmetry with eight facets of (111) surfaces, which is the cristallographically most important surface.[260–262] Figure 4.1 depicts the structure of this nanodiamond with the oxidative adsorbates $H_2O \cdot H_2O$, $H_3O^+ \cdot H_2O$, $O_2 \cdot H_2O$ and $O_3 \cdot H_2O$, for which the charge transfer doping magnitudes are summarized in table 4.1.
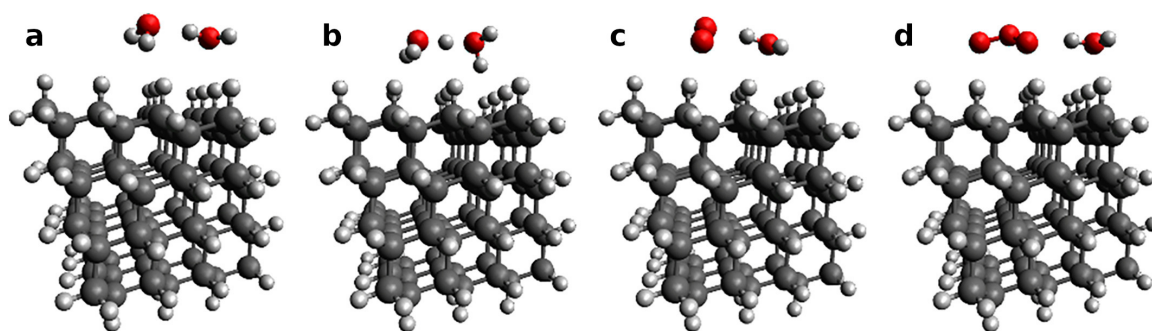

Figure 4.1: The nanodiamond $C_{84}H_{64}$ with molecular adsorbates (a) $H_2O \cdot H_2O$, (b) $H_3O^+ \cdot H_2O$, (c) $O_2 \cdot H_2O$, (d) $O_3 \cdot H_2O$. Colors: C (black), O (red), H (light grey). Reproduced from Kirschbaum *et al.* with permission from Wiley Periodicals LLC.[96]

Table 4.1: Charge transfer (CT) from the nanodiamond $C_{84}H_{64}$ towards varying adsorbates, quantified by the transferred Hirshfeld charge (in elemental unit charge e).

Nanodiamond	Adsorbate	CT (e)
$C_{84}H_{64}$	$H_2O \cdot H_2O$	0.00
$C_{84}H_{64}$	$H_3O^+ \cdot H_2O$	0.21
$C_{84}H_{64}$	$O_2 \cdot H_2O$	0.44
$C_{84}H_{64}$	$O_3 \cdot H_2O$	0.51

When only water is present at the $C_{84}H_{64}$ nanodiamond, no transfer doping is observed. For the oxidative adsorbates, the charge transfer increases from 0.21 e (hydronium) to 0.44 e (oxygen) to 0.51 e (ozone). This trend correlates with the electrochemical standard reaction potentials of the molecules.[92,263] In table 4.2, we list some relevant standard reaction potentials E^0 *vs.* the standard hydrogen electrode for the molecular adsorbates under investigation here and later in this chapter.[264]

This finding corroborates the observation that electrons rearrange towards the oxidative adsorbates to drive the respective redox reaction in the aqueous phase,

Table 4.2: Selected aqueous standard reaction potentials for the adsorbates investigated in tables 4.1 and 4.7.

Reaction	Standard Potential
$2H^+ + 2e^- \longrightarrow H_2(g)$	$E^0 = \pm 0.0$ V
$O_2 + 4H^+ + 4e^- \longrightarrow 2H_2O$ (in pH 7 water)	$E^0 = +0.8$ V
$O_2 + 2H_2O + 4e^- \longrightarrow 4OH^-$	$E^0 = +0.4$ V
$O_3 + H_2O + 2e^- \longrightarrow O_2 + 2OH^-$	$E^0 = +1.2$ V
$CO_2 + H_2O + 2e^- \longrightarrow HCOO^- + OH^-$	$E^0 = -0.7$ V
$N_2O + 5H_2O + 4e^- \longrightarrow 2NH_2OH + 4OH^-$	$E^0 = -1.1$ V
$2SO_3^{2-} + 4e^- + 3H_2O \longrightarrow S_2O_3^{2-} + 6OH^-$	$E^0 = -0.6$ V
$SO_4^{2-} + 2e^- + H_2O \longrightarrow SO_3^{2-} + 2OH^-$	$E^0 = -0.9$ V

as found in earlier studies on bulk diamond.[81,92] The presence of these adsorbates markedly changes the nanodiamond's electronic structure and may modify its application-related properties and increase its reactivity. Especially, aqueous ozone, which is used as an oxidizing agent for H-terminated NDs, strongly induces hole formation in the nanodiamonds, potentially resulting in faster oxidation reactions.[37] The charge transfer magnitudes obtained here are similar to those reported for the periodic diamond (100) surface, however, different theoretical methods were used in this study, which makes a direct comparison unfeasible.[92]

Next, we quantify the transfer doping for nanodiamonds with different sizes towards $O_2 \cdot H_2O$, which is the most common oxidative adsorbate. As listed in table 4.3, the charge transfer increases for nanodiamonds of larger size. Due to the quantum confinement effect, smaller structures have larger optical gaps and concomitant lower HOMO energies (*cf.* also the first section of appendix A2). Accordingly, the respective energy difference between the nanodiamond HOMO and the adsorbate LUMO decreases, and less electron density is transferred.

Table 4.3: Charge transfer (CT) from nanodiamonds of different sizes towards the adsorbate $O_2 \cdot H_2O$, quantified by the transferred Hirshfeld charge (in elemental unit charge e).

Nanodiamond	Adsorbate	CT (e)
$C_{35}H_{36}$	$O_2 \cdot H_2O$	0.30
$C_{53}H_{48}$	$O_2 \cdot H_2O$	0.36
$C_{84}H_{64}$	$O_2 \cdot H_2O$	0.44
$C_{147}H_{100}$	$O_2 \cdot H_2O$	0.51

We now investigate how surface modification of the nanodiamond influences the charge transfer doping. Table 4.4 summarizes the transfer doping magnitudes for the C_{85} nanodiamond that is fully covered by either hydrogen, hydroxyl oxygen, or

fluorine moieties. The charge transfer is reduced by 30 % when exchanging the hydrogen with hydroxyl, and virtually depleted upon complete fluorination. This trend again correlates with the HOMO energies of the respective nanodiamonds, which are reduced upon oxidation, and even further reduced upon fluorination, which induces a strong decrease in the amount of the transferred charge.

Table 4.4: Charge transfer (CT) from the nanodiamonds $C_{84}X_{64}$ (X = H, OH, F) towards the adsorbate $O_2 \cdot H_2O$, quantified by the transferred Hirshfeld charge (in elemental unit charge e).

Nanodiamond	Adsorbate	CT (e)
$C_{84}H_{64}$	$O_2 \cdot H_2O$	0.44
$C_{84}(OH)_{64}$	$O_2 \cdot H_2O$	0.31
$C_{84}F_{64}$	$O_2 \cdot H_2O$	0.05

4.3.2   Inhomogeneous Nanodiamonds

We proceed to investigating the impact of the local surface electronic structure of the nanodiamonds on the surface transfer doping, if the structure is only partially covered by either surface species or by a patch of amorphous carbon, and H-terminated otherwise. The addition of amorphous carbon (or fullerene-like reconstructions, FLR) on the diamond surface yields additional occupied and unoccupied orbitals in the band gaps of the nanodiamonds. This is shown for the nanodiamond $C_{170}H_{120}$ with increasing FLR coverage in figure 4.2.

The non-covered ND-H $C_{170}H_{120}$ has a negative electron affinity of -0.93 eV and a HOMO–LUMO gap of 6.46 eV, which is higher than the bandgap of bulk diamond (5.5 eV) due to the quantum confinement effect.[243] Upon addition of amorphous carbon on the nanodiamond, new orbitals are introduced by the surface patches, resulting in a decrease of the optical gap (fig. 4.2b). Contour plots of the relevant orbitals are depicted in appendix A2, showing that the mid-gap orbitals are indeed localized on the FLRs. With increasing coverage, additional orbitals appear within the optical gap. Interestingly, the HOMO energies are highest with small amorphous surface patches present and again decrease with larger reconstructed areas. This decrease in HOMO energies is, however, not monotonous. In contrast, the LUMO energies decrease monotonically with increasing amorphous carbon coverage. For nanodiamond photocatalysis, the lower band gap induced by the amorphous carbon facilitates lower-energy light excitations in the visible spectral range.[55]

We now investigate the surface transfer doping at two partially hydroxylated and fluorinated nanodiamonds, and at two nanodiamonds with partial amorphous carbon

(a)
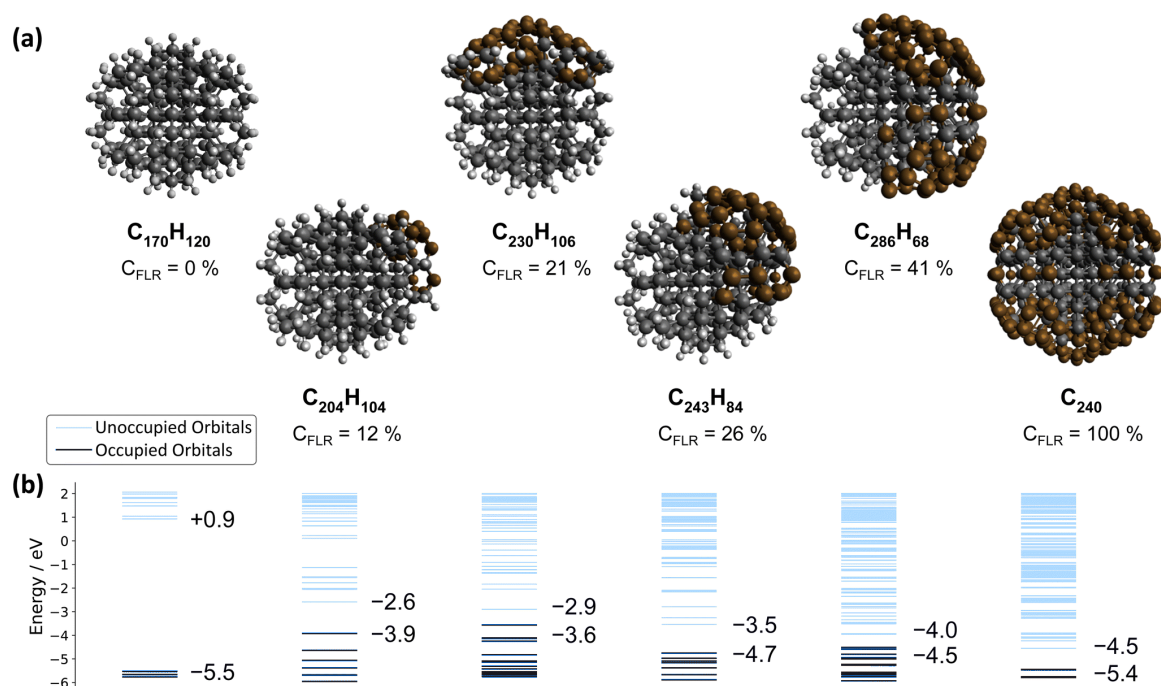
Figure 4.2: (a) Structures, sum formulae and amorphous carbon coverage (fullerene-like reconstructions, C_{FLR}, atom%) of the nanodiamond series. (b) Energies of the occupied and unoccupied orbitals. The HOMO and LUMO energies are given in eV. Nanodiamonds with increasing amorphous carbon coverage, from left to right: ND-H $C_{170}H_{120}$, $C_{240}H_{104}$, $C_{230}H_{106}$, $C_{243}H_{84}$, $C_{286}H_{68}$, and fully covered C_{450}. Atom colors: Diamond C (black), amorphous C (brown), H (grey). Reproduced (modified) from Buchner *et al.* with permission from the Royal Society of Chemistry.[55]

coverage. As shown in figure 4.3, the adsorbate $O_2 \cdot H_2O$ is placed at three different positions at the nanodiamond, either at the functionalized surface, or at the edge of the functionalized surface, or at the hydrogenated part of the structure. The charge transfer doping magnitudes that were found at the nanodiamonds $C_{84}H_{54}(OH)_{10}$, $C_{84}H_{54}F_{10}$, $C_{55}H_{14}$ and $C_{27}H_{28}$ for each different adsorbate position are summarized in table 4.5. The latter two structures consist of a diamond core and an amorphous carbon patch at one side of their respective surfaces. The structures of these nanodiamonds alongside plots of their highest occupied MOs are depicted in figures 6.3 and 6.4 of appendix A2. Note that the investigation of surface transfer doping at FLR-covered $C_{170}H_{120}$ was not feasible here, because the $O_2 \cdot H_2O$ adsorbate would inevitably form covalent bonds with the amorphous carbon layers.

The charge transfer that is observed from the partially functionalized nanodiamond to the respective adsorbate is largely independent of the position of the adsorbate. The bulky hydroxyl moieties push the adsorbate further away from the diamond core, and both OH and F strongly change the local electronic surface chemistry, *e.g.*, by inverting the surface dipoles. The amorphous carbon shells on the

$C_{27}H_{28}$	$C_{55}H_{14}$	$C_{84}H_{54}(OH)_{10}$	$C_{84}H_{54}F_{10}$
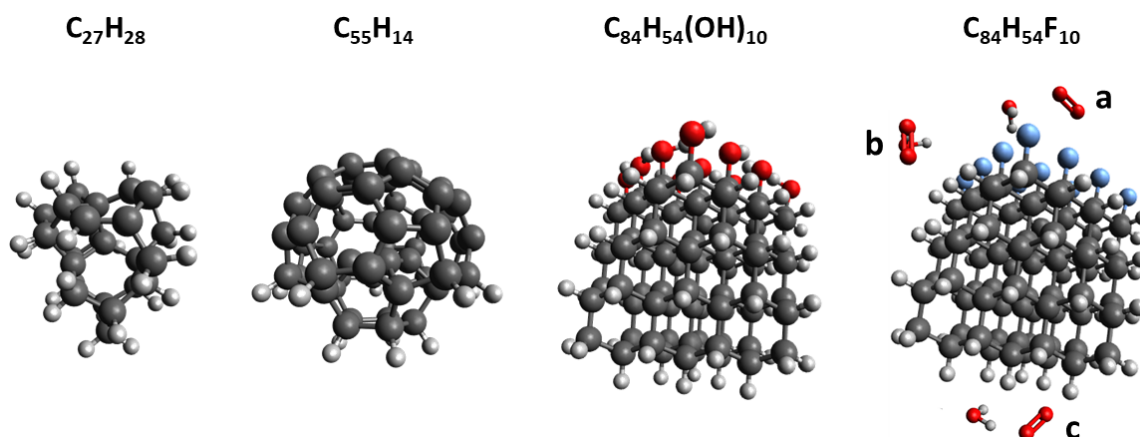
Figure 4.3: Structures of the nanodiamonds $C_{27}H_{28}$, $C_{55}H_{14}$, $C_{84}H_{54}(OH)_{10}$, $C_{84}H_{54}F_{10}$, and positions of the adsorbate $O_2 \cdot H_2O$ (illustrated for $C_{84}H_{54}F_{10}$): (a) at the fluorinated surface, (b) at the interface between the H- and F-terminated parts of the structure, and (c) at the hydrogenated surface. Atom colors: C (black), O (red), F (blue), H (grey).

Table 4.5: Charge transfer (CT) from four different nanodiamonds ($C_{27}H_{28}$, $C_{55}H_{14}$, $C_{84}H_{54}(OH)_{10}$, $C_{84}H_{54}F_{10}$) with densely packed partial functionalization towards the adsorbate $O_2 \cdot H_2O$, quantified by the transferred Hirshfeld charge (in elemental unit charge e). The adsorbate is located at either (a) at the functionalized surface, (b) at the boundary of the functionalized surface, or (c) at the H-terminated part of the nanodiamond (*cf.* figure 4.3).

Nanodiamond	Adsorbate	Adsorbate Position	CT (e)
$C_{27}H_{28}$	$O_2 \cdot H_2O$	a (C shell)	0.33
		b (boundary)	0.35
		c (H surface)	0.37
$C_{55}H_{14}$	$O_2 \cdot H_2O$	a (C shell)	0.41
		b (boundary)	0.37
		c (H surface)	0.36
$C_{84}H_{54}(OH)_{10}$	$O_2 \cdot H_2O$	a (OH surface)	0.37
		b (boundary)	0.43
		c (H surface)	0.38
$C_{84}H_{54}F_{10}$	$O_2 \cdot H_2O$	a (F surface)	0.35
		b (boundary)	0.37
		c (H surface)	0.34

nanodiamonds introduce new occupied and unoccupied orbitals into the structures' optical gaps.[55] Nevertheless, these local structural and electronic changes hardly influence the amount of charge transfer doping that is observed at the respective structures, with fluctuations of $\pm \leq 0.06$ e Hirshfeld charge. Again, the surface doping magnitudes strongly correlate with the nanodiamonds' HOMO energies.

We furthermore quantified the charge transfer doping for $C_{84}H_{64-n}X_n$ (X = OH, F) with n = 8 or 10 hydroxyl or fluorine moieties randomly spread out on their surfaces

towards $O_2 \cdot H_2O$. The results are summarized in table A2.3 in appendix A2. Again, we do not observe any systematic trends in the transfer doping that are induced by the local surface chemistry of the hydroxyl- or fluorine-terminated sites, but only random fluctuations of $\pm \leq 0.03$ e Hirshfeld charge.

Finally, we investigate how doping of the nanodiamonds with a single heteroatom (B, Si, N) locally influences the charge transfer doping. For each dopant, the respective atom is placed at either one of two positions in the nanodiamond $C_{83}YH_{63}$ (Y = B, SiH, N) as illustrated in figure 4.4. The charge transfer doping is quantified for the adsorbate $O_2 \cdot H_2O$ located either (a) next to the dopant, (b) further away from the dopant, or (c) far away from the dopant (*i.e.*, at the other side of the nanodiamond, *cf.* also figure 4.1). The results are listed in table 4.6.
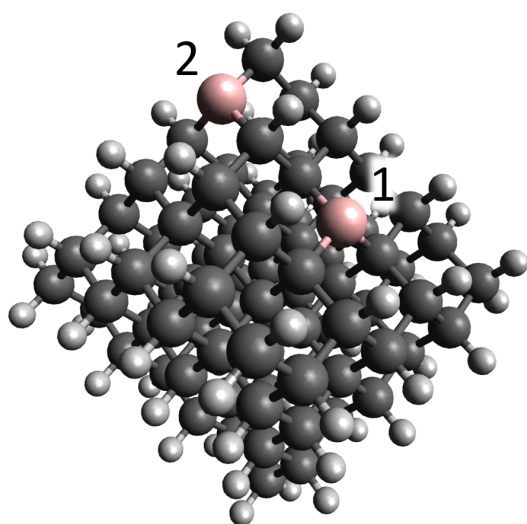

Figure 4.4: Illustration of the dopant positions 1 and 2 at the doped nanodiamond $C_{83}YH_{63}$ (Y = B, SiH, N) (here with B dopant). Atom colors: B (rose), C (black), H (grey).

We again find that the local change of the surface chemistry, here induced by the respective dopant atom, has no systematic effect on the amount of charge transfer doping. Potentially, the replacement of a core carbon atom (instead of a surface CH) with a boron or nitrogen dopant will induce stronger changes of the electronic structure and then also locally influence the charge transfer doping. However, these structures are not stable for the $C_{84}H_{64}$ investigated here and, therefore, such investigations are left for future work.

For all structures investigated here, we find that neither the degeneracy of the nanodiamond HOMO orbital nor the introduction of new orbitals in the optical gap have an impact on the charge transfer doping magnitudes. The HOMO of the nanodiamond $C_{84}H_{64}$ is threefold degenerate due to the high symmetry of the system,

Table 4.6: Charge transfer (CT) from singly doped nanodiamonds $C_{83}YH_{63}$ (Y = B, SiH, N) towards the adsorbate $O_2 \cdot H_2O$, quantified by the transferred Hirshfeld charge (in elemental unit charge e). The distance between dopant and adsorbate increases from position a to b to c.

Nanodiamond	Dopant Position	Adsorbate	Adsorbate Position	CT (e)
$C_{83}BH_{63}$	**B 1**	$O_2 \cdot H_2O$	a (close)	0.43
			b (distant)	0.39
			c (afar)	0.44
$C_{83}BH_{63}$	**B 2**	$O_2 \cdot H_2O$	a (close)	0.44
			b (distant)	0.43
			c (afar)	0.38
$C_{83}SiH_{64}$	**Si 1**	$O_2 \cdot H_2O$	a (close)	0.42
			b (distant)	0.44
			c (afar)	0.43
$C_{83}SiH_{64}$	**Si 2**	$O_2 \cdot H_2O$	a (close)	0.45
			b (distant)	0.45
			c (afar)	0.39
$C_{83}NH_{63}$	**N 1**	$O_2 \cdot H_2O$	a (close)	0.43
			b (distant)	0.44
			c (afar)	0.46
$C_{83}NH_{63}$	**N 2**	$O_2 \cdot H_2O$	a (close)	0.50
			b (distant)	0.47
			c (afar)	0.44

and the degeneracy is reduced when local surface species or dopants are introduced (*cf.* figure 6.3 in appendix A2). In contrast, when adding amorphous surface carbons, new occupied and unoccupied orbitals are introduced in the structures' optical gaps (*cf.* figure 6.4 in appendix A2). However, the addition or removal of such high-energy orbitals at the nanodiamonds that would be suitable for charge transfer doping does not influence the amount of transfer doping.

In figure 4.5, we show a scatter plot of the HOMO energies and transfer doping magnitudes towards $O_2 \cdot H_2O$ for the nanodiamonds investigated here. The plot indicates a strong correlation between the two values, with two outliers $C_{55}H_{14}$ and $C_{27}H_{28}$ corresponding to the structures partially covered by amorphous carbon (marked by orange arrows). We find a Pearson correlation coefficient of $r_c = 0.92$ when excluding the outliers. The additional occupied orbitals introduced by the amorphous carbon patches shift the respective data points away from the linear fit.
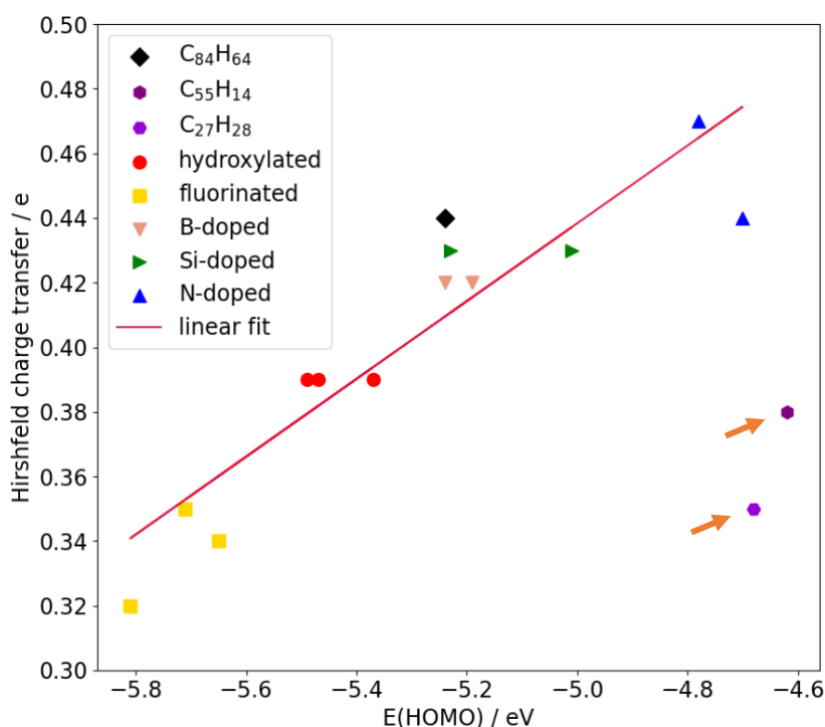
Figure 4.5: Scatter plot of nanodiamond HOMO energies (in eV) and Hirshfeld charge transfer doping towards $O_2 \cdot H_2O$ (in e). The charge transfer towards each nanodiamond is averaged over the different adsorbate positions. The nanodiamonds partially covered with amorphous carbon $C_{55}H_{14}$ and $C_{27}H_{28}$ are identified as outliers (marked by orange arrows). The linear fit without the outliers is indicated by the red line.

4.3.3 Impact on Nanodiamond Excited States

The presence of aqueous adsorbates may not only influence the electronic properties of nanodiamonds in the ground state, but potentially also has marked effects on the excited states of the nanodiamonds. This is of particular interest for photocatalysis[17,234] and some biomedical applications,[235] where nanodiamonds in water dispersion are excited by ultraviolet light to produce free aqueous electrons. In the photocatalytic process, the electrons are emitted from the nanodiamonds upon photoexcitation and move into the surrounding water, where the water molecules rearrange to form dynamic cavities around them.[17,63,234] The solvation mechanism may be strongly influenced by the presence of adsorbates.

In nanodiamond photocatalysis experiments, a multitude of molecules may be present in the aqueous dispersion. Purging the reaction solution with a non-interacting gas (*e.g.*, H_2 or N_2) removes ambient gases, such as oxygen, which increases the lifetimes of the solvated electrons.[65] In the ground state, charge transfer doping occurs towards the oxidative adsorbates H_3O^+, O_2 and O_3 (*cf.* table 4.1),

but we observed no transfer doping towards unreactive gases, such as CO_2 or N_2O, which is in agreement with previous work. [94] Nevertheless, nitrous oxide acts as an electron scavenger in water: When reacting with aqueous free electrons, it irreversibly decomposes into N_2 gas and OH_{aq}^-. [17,265,266]

Moreover, the sodium sulfite/sulfate couple is used in experiments to replenish the holes that are created in the nanodiamonds upon excitation in order to prevent their oxidation and concomitant degradation. [21] For the salts Na_2SO_3 and Na_2SO_4, the charge transfer doping has not been quantified, because these salts may induce different effects than the small molecules investigated so far. Most probably, some electron density would be transferred to the aqueous sodium cations, but no electron transfer is expected towards anions, such as SO_3^{2-} and SO_4^{2-}.

Here, we investigate how the lowest charge transfer excited state of the aqueous nanodiamond $C_{56}H_{36}$ is influenced by the presence of the aforementioned adsorbates. The nanodiamond is surrounded by an explicit layer of 93 water molecules and either none or one of the adsorbate molecules CO_2, N_2O, O_2, O_3, Na_2SO_3 and Na_2SO_4 (see figure 4.6 and appendix A2). The states are analyzed by plotting the corresponding natural transition orbitals, which visualize the hole and electron that are created in the respective excitation. [267]

The structures and excited state natural transition orbital densities of all systems are plotted in appendix A2, figures A2.5 and A2.6. Figure 4.6 exemplarily shows the excitation of the aqueous $C_{56}H_{36}$ with an oxygen adsorbate. If no adsorbate is present, the excited electron is delocalized on the surface of the water shell, where it is stabilized by dangling hydrogen atoms that are not part of the water hydrogen bond network. This finding is in agreement with previous work on electron injection into small water clusters, where the excess electrons move to the respective cluster surface. [268–270] The adsorbates CO_2 and Na_2SO_4 slightly change the geometry of the excitation, but also here, the electrons predominantly move to the surface of the respective system. If an oxidative adsorbate is present (O_2, O_3, Na_2SO_3), the electron instead localizes at the respective adsorbate molecule.

Table 4.7 lists the electron affinity of the molecular adsorbates in vacuum and in water (molecule · 3 H_2O), which is usually a good indicator of a molecule's tendency to attract electronic charge, and the excited state Hirshfeld charge transfer towards the respective adsorbate. The sodium salts have very different sizes and solvation structures as compared to the small molecules (CO_2, N_2O, O_2, O_3), therefore, we do not attempt to directly compare the electron transfer among these two different kinds of adsorbates. Among the individual groups, however, we find that the excited state charge transfer is largely independent of the molecules' electron affinities,

<div align="center">structure   hole   electron</div>
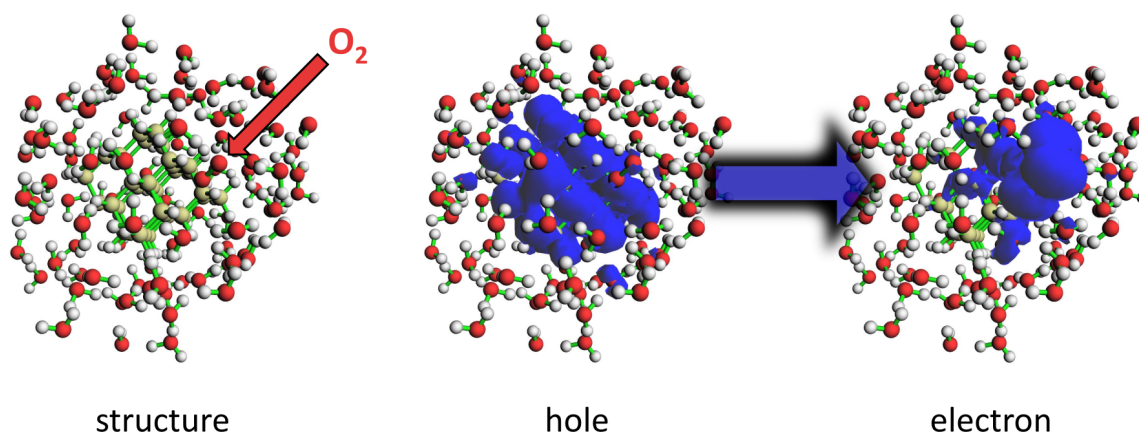
Figure 4.6: Structure and charge transfer excited state natural transition orbitals (hole and electron) for $C_{35}H_{36}$ with an explicit water layer and an oxygen adsorbate (highlighted by the red arrow). The blue arrow indicates the electron transfer from the natural transition orbital hole density to the natural transition orbital electron density upon excitation.

Table 4.7: Charge-transfer excited states of $C_{35}H_{36}$ with a water layer and various aqueous adsorbates: Adsorbate, electron affinity (EA) of the adsorbate in vacuum and with three water molecules (both in eV), and Hirshfeld charge transfer (CT) towards the adsorbate (in elemental unit charge e).

Adsorbate	$EA_{Molecule}$ (eV)	$EA_{Molecule \cdot 3H_2O}$ (eV)	CT (e)
CO_2	-3.24	-0.87	0.03
N_2O	-1.89	-0.34	0.82
O_2	2.03	2.55	0.86
O_3	2.76	3.83	0.93
Na_2SO_3	0.36	0.00	0.17
Na_2SO_4	0.39	0.14	0.01

but correlates with the standard reaction potential of the respective adsorbate (see table 4.2). The same correlation was found for the ground state charge transfer doping, indicating that this phenomenon also directly influences the mechanism of the electronic excitation.

The only marked exception in the observed trends is a strong excited state charge transfer towards the nitrous oxide. This molecule has a low standard reaction potential with water, negative electron affinities, and no charge transfer doping is observed in the ground state. Still, a significant charge transfer is observed towards the N_2O upon excitation. We find that in the water layer, the N_2O molecule is net positively charged (Hirshfeld: $+0.07$ e, Loewdin: $+0.21$ e), which is much less the case for the equally unreactive CO_2 (Hirshfeld: $+0.03$ e, Loewdin: ±0.00 e). This positive charge apparently creates a minimum in the potential energy surface of the system, which creates a trap for the excited electron.

4.4   Conclusions

In this chapter, we investigated the effect of charge transfer doping on the electronic structure of nanodiamonds. The magnitude of charge transfer increases with higher HOMO energies of the nanodiamond, and correlates with the standard reaction potentials of the molecular adsorbates. The nanodiamond HOMO energies can be tuned by size modification, surface functionalization, or by the introduction of dopant atoms. At nanodiamonds with inhomogeneous surface covering (hydroxyl, fluorine, amorphous carbon or lattice dopants), local changes of the nanodiamonds' electronic structures do not have any marked impact on the charge transfer doping.

We furthermore investigated the impact of charge transfer doping on the excited states of an aqueous nanodiamond. If no adsorbate or a non-interacting adsorbate (CO_2, Na_2SO_4) is present, the electron moves towards the water surface upon excitation. The oxidative adsorbates (O_2, O_3, Na_2SO_3) effectively capture the excited electronic charge, potentially preventing it from travelling further into the solution and forming a free solvated electron. Here, again, the charge transfer correlates with the standard reaction potentials of the adsorbates. This finding confirms that replacing oxidative species with non-interacting molecules may increase the electron yield upon electronic excitation. However, also the non-interacting nitrous oxide effectively captures the excited electron, due to its positive partial charge induced by the local solvation geometry. This finding underpins the ability of N_2O to quench aqueous electrons despite its negative electron affinity and low electrostatic potential.

Furthermore, in appendix A2, we show that also clustering of nanodiamonds has a marked impact on the systems' electronic properties. When the cluster sizes increase, their optical gaps narrow, which is a result of the quantum confinement effect. Moreover, the lowest unoccupied molecular orbitals of various clusters resemble atomic s-, p-, d-, ... orbitals, as was previously found for spherical isolated nanodiamonds.

In summary, this work demonstrates that nanodiamonds should not be considered as inert particles when used in aqueous dispersions. Depending on their sizes and chemical modifications, they may strongly interact with both oxidative species and other dissolved molecules, such as N_2O, but also potentially with other O-containing molecules (such as proteins). Our findings have important implications, *e.g.*, for nanodiamond electronic devices and photocatalysis, where the size of their optical gaps and the initial charge transfer excited states are crucial parameters of the respective underlying processes. The precise interactions would require further experimental characterizations and should certainly be considered to obtain a full picture of nanodiamonds' properties in colloidal solutions.

Chapter 5

Machine Learning Frontier Orbital Energies of Nanodiamonds

The contents of this chapter were published in the article

The article can be accessed via the following link:

https://pubs.acs.org/articlesonrequest/AOR-B345ZK4GERVNGXMUVEZX

Thorren Kirschbaum was lead author and sole first author in this project. The author contributions were as follows: T. Kirschbaum: Project conceptualization, data set implementation, machine learning implementation, data analysis, validation, visualization, manuscript writing. B. von Seggern: Machine learning implementation, data analysis, validation. J. Dzubiella: Project conceptualization, funding acquisition, supervision, validation, manuscript writing. A. Bande: Project conceptualization, supervision, validation, manuscript writing. F. Noé: Project conceptualization, supervision, validation, manuscript writing.

Chapter 6

Conclusion

Sunlight-driven photocatalysis with aqueous nanodiamonds has the potential to revolutionize a variety of high-energy reduction reactions that can be conducted in the liquid phase. Replacing the current energy-intensive industrial processes would constitute a major step towards sustainable energy harvesting in the form of water splitting, ammonia production and the synthesis of chemical base materials, starting from the reduction of carbon dioxide.

The results presented within this thesis shed light on the different facets of nanodiamond properties which precede and influence the photocatalytic processes. Chapter 3 of this thesis has characterized a sample of highly fluorinated nanodiamonds from liquid HF synthesis, revealing a surface fluorine content of about 50 % and analyzing in detail the spectroscopic signatures of XAS and RIXS experiments. Starting from fluorination, nanodiamonds can be further modified and their surface structures tuned towards various applications. Higher fluorine coverages on the nanodiamonds would allow for more powerful synthesis routes, in which up to 100 % of the samples may be covered by the respective final species. Accordingly, further experimental research would be highly desirable to achieve (almost) complete fluorine coverage on the nanodiamonds, and the data presented within this thesis may be used to guide their analysis.

In most of their applications, nanodiamonds are in contact with aqueous environments or ambient moist, where they interact with aqueous species. As shown in chapter 4, these interactions may strongly influence the nanodiamonds' electronic properties, potentially adversely affecting the respective applications targets. In photocatalysis, the presence of oxidative adsorbates (*e.g.*, O_2, O_3), positively charged ions (*e.g.*, Na^+) or molecules with a positive partial charge (*e.g.*, N_2O) may impede the formation of solvated electrons by directly capturing the excited charges. Accordingly,

in photocatalytic experiments, the presence of circumfluent molecules needs to be carefully controlled in order to avoid deleterious effects. In future research, these interactions may be considered for other applications as well. For example, the impact of interacting species present in electrolyte solutions or biological environments may have strong effects on nanodiamonds used as electrode materials and in biomedicine, respectively.

Finally, the large number of nanodiamond modifications available renders a huge array of possible configurations that may be tested for each application target. Based on the ND5k data set of about 5000 nanodiamond structures with different shapes, surface terminations and scaffold dopants introduced in chapter 5, we suggest to consider P-doped, H- or NH_2-terminated nanodiamonds for use as sunlight-driven photocatalysts. However, the structures covered by the ND5k dataset still represent only a fraction of possible nanodiamond designs. Further research may explore new combinations of surface decorations, doping patterns, nano-structuration, composite materials, solvents, etc. to enable the facile emission of nanodiamond electrons into the surrounding medium. However, the plethora of design choices makes experimental research tedious and slow. Likewise, the use of machine learning to leverage the design of nano-sized materials remains difficult as of today. Only little data is available in the field, and the modern ML algorithms usually fail to make sensible predictions outside the range of the small training data sets. Accordingly, the compilation and publication of further systematically crafted data sets, as well as the development of robust algorithms for molecular property prediction would be highly desirable.

This thesis has provided important insights and suggestions towards sunlight-driven nanodiamond photocatalysis. However, the computational investigations focused only on the properties of static systems, which poses severe limits on the processes that can be captured by the respective models. Complementary studies on the dynamic process of electron excitation and solvation would be highly desirable to better understand and optimize the reaction. Further research on the electron dynamics upon excitation, as well as molecular dynamics of aqueous nanodiamonds and free electrons is currently in planning and will be carried out in the near future.

Appendix

A1 Soft X-Ray Characterization of Highly Fluorinated Nanodiamonds

This appendix contains information on the following items:

Experimental X-ray photoelectron spectra details

Experimental C K-edge XAS fitting parameters

XAS building block principle

DFT/ROCIS XAS calibration

DFT/ROCIS C K-edge XAS compositions of highly fluorinated nanodiamonds

Frontier orbital energies of the randomly fluorinated nanodiamonds

DFT/ROCIS RIXS partial orbital space assessment

DFT/ROCIS RIXS F K-edge maps of fully fluorinated adamantane

DFT/ROCIS RIXS F K-edge maps of the fluoromethanes

Natural difference orbitals for the fluorinated adamantanes' RIXS F K-edge spectra

Experimental X-ray photoelectron spectra details

We here present and discuss the XPS spectra of the HF-fluorinated nanodiamonds in more detail, based on the analysis from Dr. Arsène Chemin. Figure A1.1a shows the XPS survey spectrum measured at $E_{h\nu} = 750$ eV. The F(1s) and C(1s) signals are assigned to nanodiamonds, as is the small N(1s) signal that indicates nitrogen contamination of the particles. Nitrogen pollution is commonly observed for detonation nanodiamonds, originating from the N-containing precursors, such as TNT and hexogen. [15] The Si(2s) and Si(2p) signals likely originate from the sample holder, and the large emission of O(1s) is likely due to the substrate oxide layer and water adsorption, as the sample has not been annealed. Note that the emission spectra shift to higher energies due to charging of the samples. The CasaXPS fit of the survey peaks suggests an atomic ratio of about 9.5 % fluorine for 90.5 % carbon, in agreement with previous measurements (not shown). Considering an average diameter of 5 nm one can expect a fluorine surface coverage around 45 %.

Figure A1.1b-f displays the high-resolution C(1s) XPS spectra measured at energies $E_{h\nu} = 335, 435, 535, 635,$ and 750 eV, together with the respective fit. The probing depth of the XPS increases at higher photon energies, so that the measurement at $E_{h\nu} = 335$ eV is extremely surface-sensitive, while the measurements at higher energies penetrate increasingly deeper into the nanodiamonds. Also, by increasing the photon energy, the spectra shift to higher energies due to charging of the sample, which must be considered during the fitting process. Fitting was performed within the CasaXPS software, using a Toogaard background and Voigt-type line shapes. Only four components are considered here: sp^3 carbon bonds corresponding to the diamond lattice (nanodiamond core), sp^2 carbon bonds corresponding to surface defects, and C-H and C-F surface bonds. Note that the C-F bonds likely exist in different configurations, such as CF, CHF, and CH_2F (CF_2 and CF_3 moieties are unlikely as their binding energies are about 6 and 8 eV above the C-C binding energy, respectively). [271,272] This leads to a broadening of the XPS signal with FWHM$\simeq 2.6$ eV, while the reference highly ordered pyrolytic graphite peak has a FWHM$\simeq 0.47$ eV. Also note that oxygen bonds (carboxyl and hydroxyl groups) would add minor peaks in the same region of the spectrum as the C-F bonds. They are not considered in the fit, because their amount is expected small, and including them would make the data fit unstable. Accordingly, the amount of fluorine estimated from this fit can be regarded as an upper bound for the surface F content. The initial parameters for the fit were chosen to take into account the shift observed due to charging and the relative position between the sp^2 and sp^3 peaks and between sp^2 and CH peaks, which
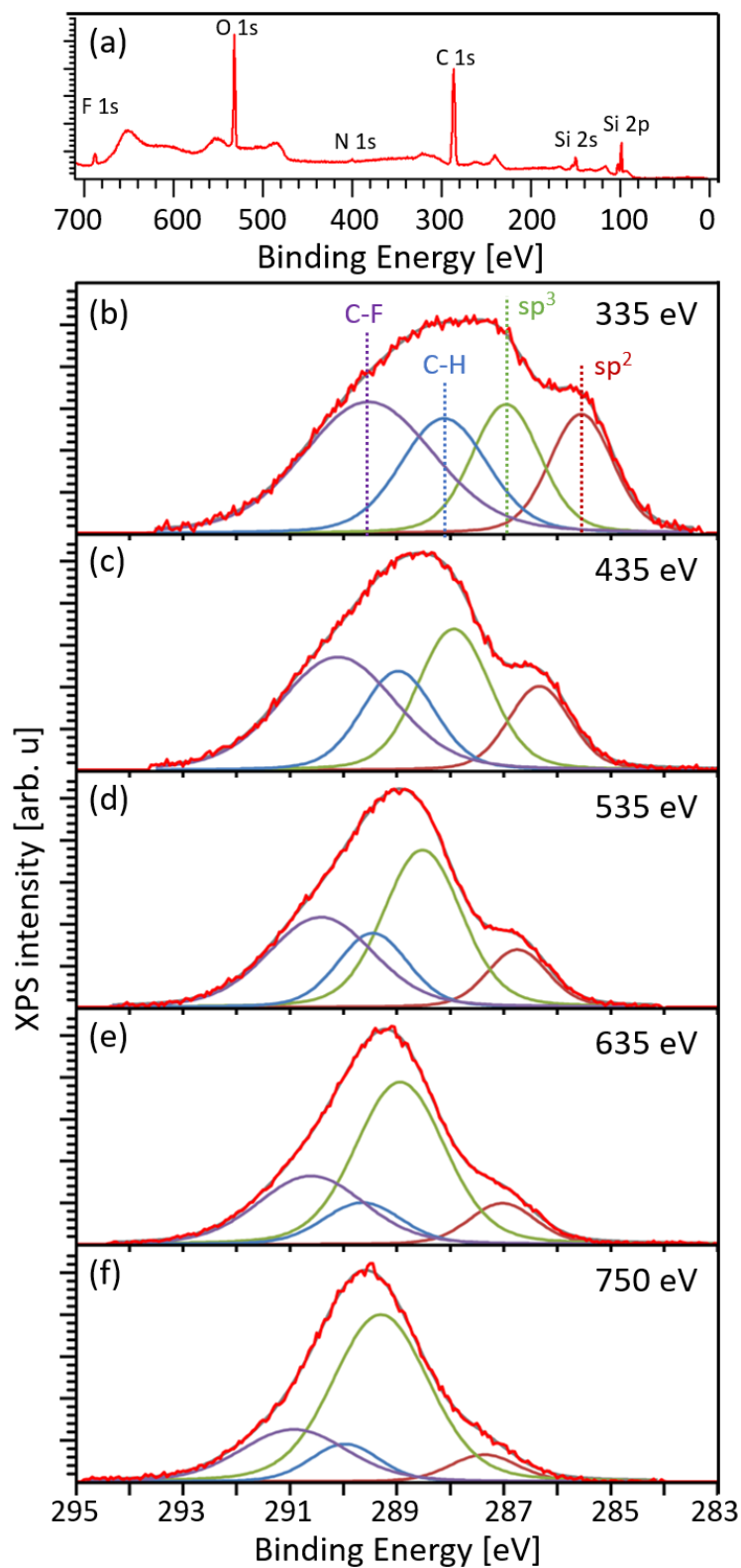
Figure A1.1: (a) XPS survey spectrum at $E_{h\nu} \leq 700$ eV, and C 1s X-ray photoelectron spectra of F-NDs measured at (b) $E_{h\nu} = 335$ eV, (c) 435 eV, (d) 535 eV, (e) 635 eV and (f) 750 eV with the general fits (gray) and their different components (colored).

were calibrated on a hydrogenated nanodiamond sample (1.3 and 2.5 eV respectively, see table A1.2).

Figure A1.2 shows the evolution of the binding energy (top) and the relative amount of the respective component (bottom) as a function of the probing energy. Overall, the shift due to charging is homogeneous across all components. The difference in the trends between the sp^3 component and the surface bonds may be due to uneven charging between the core and the surface of the nanodiamonds. Furthermore, since the probing depth increases at higher photon energies, the relative percentage of sp^3 bonds increases while the relative percentage of the surface bonds decreases. However, the ratio between the surface bounds remains constant, with 53 % CF, 20 % sp^2 carbon, and 27 % CH. This estimation is slightly higher than the estimation obtained from the XPS survey ($\simeq$ 45 % of CF).
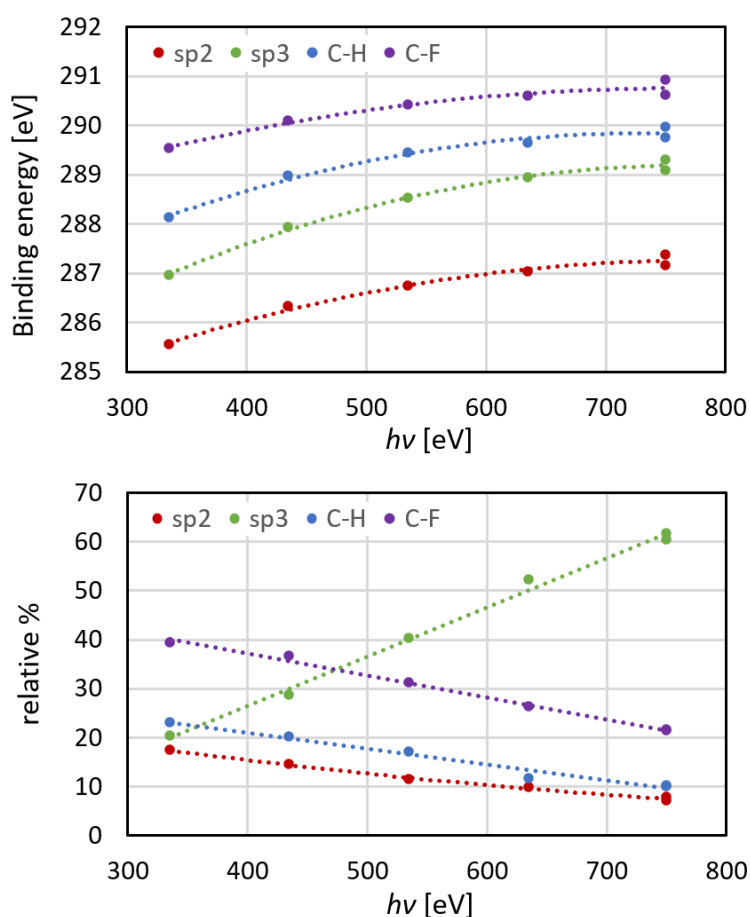

Figure A1.2: Binding energy (top) and relative amount of sp^2, sp^3, C-H and C-F bounds (bottom) depending on the probing energy $E_{h\nu}$ determined from the C 1s XPS spectra fit.

Figure A1.3a shows another C(1s) XPS characterization of the same F-ND sample, measured at $E_{h\nu}$ = 750 eV at a different measurement spot. The reproducibility of

the measurement at high energy and fitting parameters indicates a high homogeneity of the sample, and substantiates that the measurements are relevant despite charging. The fitting parameters are listed in the last rows of table A1.1. Figure A1.3b displays the F(1s) XPS characterization of the F-NDs, also shifted due to sample charging. The single signal is fitted by a Voigt function centered at 690.3 eV and a FWHM of 2.6 eV. This peak is assumed to be broadened due to the different chemical environments of the C-F bonds.
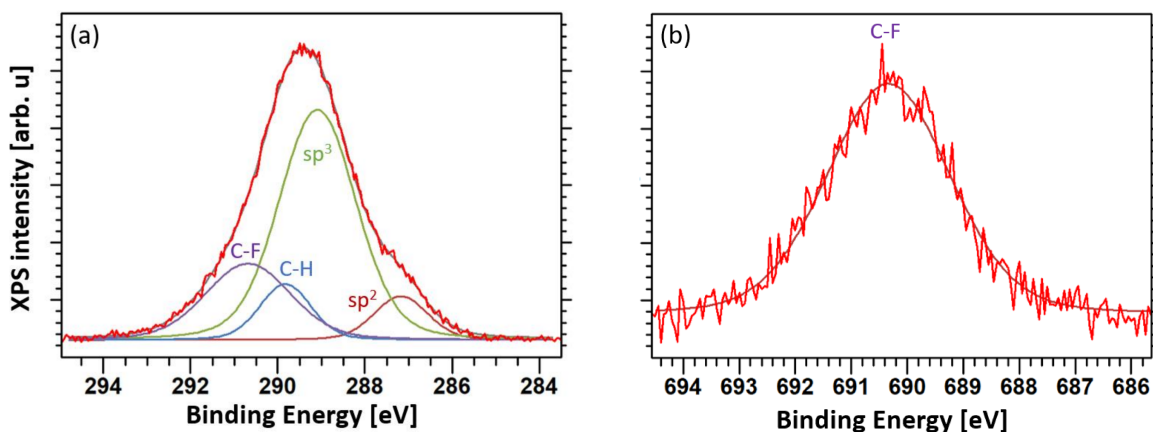

Figure A1.3: (a) C 1s and (b) F 1s X-ray photoelectron spectra of the F-ND sample measured at $E_{h\nu}$ = 750 eV, each with a general fit (grey) and its different components (colored).

Figure A1.4 depicts the C(1s) XPS characterization ($E_{h\nu}$ = 335 eV) of the hydrogenated nanodiamonds obtained from Carbodeon Ltd. Despite having a different origin than the F-NDs, this measurement and fit provide a good initial guess for the relative positions of the CH, sp^2 and sp^3 carbon peaks. The fit parameters are listed in table A1.2.
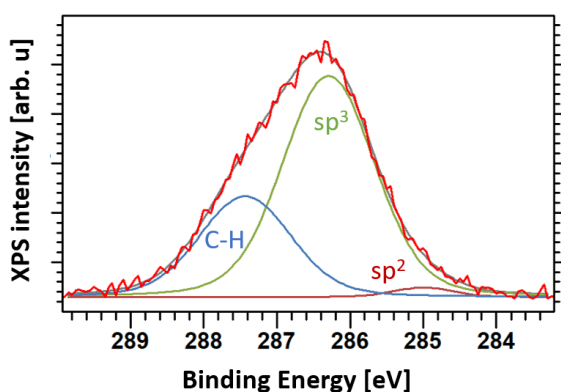

Figure A1.4: C 1s X-ray photoelectron spectra of hydrogenated ND used for reference, measured at $E_{h\nu}$ = 335 eV (red) with a general fit (grey) and its different components (colored).

Table A1.1: Fitting parameters obtained for the C 1s X-ray photoelectron spectra of F-NDs measured at $E_{h\nu}$ = 335 eV, 435 eV, 535 eV, 635 eV and 750 eV for the sp^2, sp^3, C-H and C-F bounds. The first row corresponds to the measurement shown in figure A1.1, the second row at 750 eV corresponds to the second measurement presented in figure A1.3.

Binding Energy (eV)

$E_{h\nu}$ (eV)	sp^2	sp^3	C-H	C-F
335	285.55	286.96	288.12	289.53
435	286.33	287.93	288.98	290.10
535	286.74	288.52	289.45	290.42
635	287.03	288.94	289.64	290.60
750	287.37	289.30	289.97	290.92
750	287.16	289.09	289.75	290.61

FWHM (eV)

$E_{h\nu}$ (eV)	sp^2	sp^3	C-H	C-F
335	1.39	1.51	1.92	2.89
435	1.36	1.60	1.61	2.56
535	1.34	1.72	1.55	2.33
635	1.46	1.97	1.71	2.34
750	1.49	2.11	1.51	2.34
750	1.51	2.11	1.29	2.24

Relative %

$E_{h\nu}$ (eV)	sp^2	sp^3	C-H	C-F
335	17.34	20.31	22.97	39.39
435	14.50	28.72	20.16	36.61
535	11.48	40.34	17.03	31.15
635	9.82	52.28	11.69	26.22
750	7.02	61.72	9.93	21.34
750	7.85	60.39	10.09	21.67

Table A1.2: Fitting parameters obtained for the C 1s X-ray photoelectron spectra of hydrogenated nanodiamonds measured at $E_{h\nu}$ = 750 eV for the sp^2, sp^3, and C-H bounds.

	sp^2	sp^3	C-H
Binding energy (eV)	284.96	286.29	287.43
FWHM (eV)	0.91	1.5	1.5
Relative %	1.60	67.73	30.67

Experimental C K-edge XAS fitting parameters

For the F-ND's C K-edge XA spectrum, the main edge is fitted by a Gaussian function centered at 289.15 eV with a width of $2(\sqrt{\ln 2}) \times 0.7 = 1.17$ eV. These parameters were determined by a fit on a H-terminated single crystal diamond used as reference (not shown here). The offset and amplitude are set to match the signals at 284.0 and 290.5 eV, respectively. The final parameters are listed in table A1.3.

Table A1.3: Fitting parameters of the C K-edge XA spectra of fluorinated nanodiamonds.

Assignation	Position (eV)	FWHM (eV)	Area (arb. u.)
sp^2	285.35	0.82	5.49
C=O	286.03	0.81	1.15
C-H	288.25	2.01	61.73
C-OH	288.74	0.59	8.17
exciton	289.41	0.73	13.81

XAS building block principle

We use the building block principle[201,209] to obtain the XA spectra from the single core MO's spectral contributions as described in section 3.2. Figure A1.5 shows the DFT/ROCIS XA spectra of a randomly fluorinated adamantane ($C_{10}H_{10}F_6$) at the C and F K-edge, respectively, which were calculated either in a single, full job (blue line), or by adding up the single MO spectra (red dotted line). The same total number of excitations (NRoots) was used in each case. There is virtually no difference between each two spectra, which validates the use of the building block approach for our calculations. Note that we here show the full calculated XA spectra including the region after the ionization edge to allow for a full comparison. For comparing to experimental data, we focus only on the near edge region of the spectra, because the DFT/ROCIS calculations only account for the near edge region and are not able to predict the extended fine structure of the spectra.
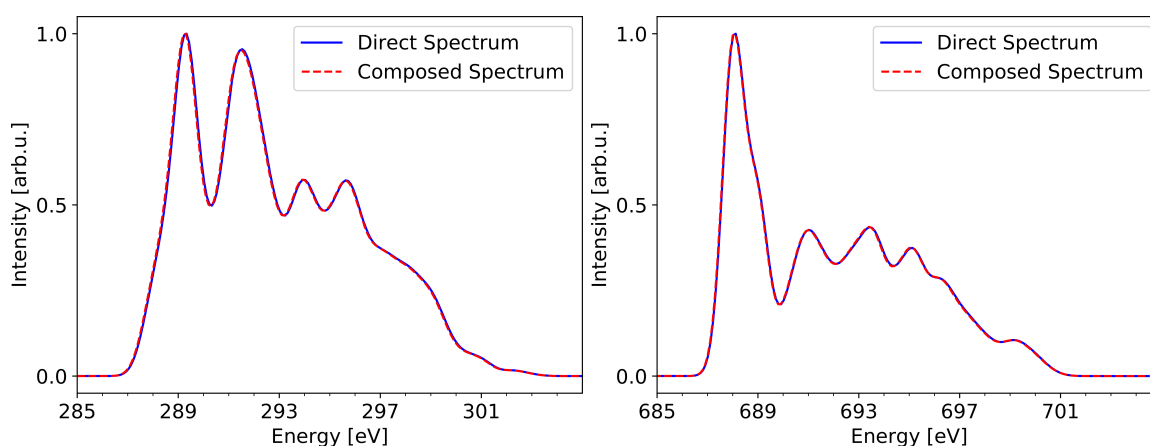

Figure A1.5: DFT/ROCIS-calculated XA spectra of randomly fluorinated adamantane ($C_{10}H_{10}F_6$) from a single, full calculation (blue line) and from the added-up single core orbitals' spectral contributions (red, dotted line). Left: C K-edge; right: F K-edge.

DFT/ROCIS XAS calibration

We used six small and medium-sized molecules to benchmark the DFT/ROCIS method for calculating XA spectra of tetrahedrally coordinated hydro- and fluorocarbons: The fluoromethanes $CH_{4-n}F_n$ (n=1–4), carbon monofluoride $(CF)_n$, and adamantane.

DFT-based methods are usually incapable of correctly predicting transitions to Rydberg excited states.[273] Nanodiamond XA spectra have no Rydberg-type signals and, therefore, do not suffer from this drawback.[198] The methane XA spectrum, however, is dominated by a Rydberg-type transition and therefore is not included in our benchmark.[214] Equally, the Rydberg signals that occur in the adamantane XA spectrum are not predicted from the calculations, but the position of the ionization edge and its pre-edge feature are predicted correctly.[27]

The sudden-approximation that is used for the XAS and RIXS calculations introduces element-specific systematic redshift to the spectra,[274] which can be corrected by fitting to the benchmark data. The shifts obtained here are +11.4 eV and +18.3 eV for C and F K-edge spectra, respectively.

The predicted and measured signals at the C and F K-edges of the benchmark systems are shown in tables A1.4 and A1.5, respectively. The calculated C K-edge spectra of the fluorinated methanes are close to the experimental results, however, this is less so for their F K-edge spectra and the C K-edge spectra of $(CF)_n$ and adamantane. The qualitative trend in the fluoromethane's F K-edge spectra is predicted correctly, however, the respective distances between each pair of signals are smaller than in the experiments (see table A1.5).

We also tested the more commonly used linear-response time-dependent DFT method[201,275,276] for reproducing the XA spectra of the aforementioned systems, but we found the DFT/ROCIS method to give more accurate results. The benchmark overall suggests that the DFT/ROCIS predictions will be able to aid the understanding of the nanodiamond XA spectra, even though the relative signal intensities may deviate for some spectra and trends are only reproduced semi-quantitatively.

Table A1.4: Energy positions (eV) of the near-edge C K-edge signals: DFT/ROCIS calculations (B3LYP-D3/def2-TZVP), deviation from experiment, and experimental values. DFT/ROCIS energies are shifted by +11.4 eV for C K-edge spectra to obtain the best match with the experiments.

Molecule and Signal	DFT/ROCIS	Deviation	Experimental
CH_3F	289.4	+0.3	289.1 [214]
CH_2F_2	292.1	+0.3	291.8 [214]
CH_2F_2	293.0	+0.1	292.9 [214]
CHF_3	294.8	+0.2	294.6 [214]
CF_4	297.8	±0	297.8 [214]
CF_4	not predicted		298.5 [214]
$(CF)_n$	288.7	−1.0	289.7 [70]
$(CF)_n$ edge	291.5	−0.3	291.8 [70]
Adamantane	288.9	−0.4	289.3 [27]
Adamantane edge	291.9	−0.2	292.1 [27]

Table A1.5: Energy positions (eV) of the NEXAFS F K edge signals: DFT/ROCIS calculations (B3LYP-D3/def2-TZVP), deviation from experiment, and experimental values. DFT/ROCIS energies are shifted by +18.3 eV for F K-edge spectra to obtain the best match with the experiments.

Molecule and Signal	DFT/ROCIS	Deviation	Experimental
CH_3F	688.6	+1.5	687.1 [214]
CH_2F_2	689.6	+0.2	689.4 [214]
CHF_3	690.6	−0.4	691.0 [214]
CF_4	691.0	−1.1	692.1 [214]
$(CF)_n$ edge	687.2	−0.6	687.8 [70]

DFT/ROCIS C K-edge XAS compositions of highly fluorinated nanodiamonds

Figure A1.6 shows the functional groups' contributions to the C K-edge spectra of the 35/36 and fully F-ND, respectively (structures in figure 3.2).
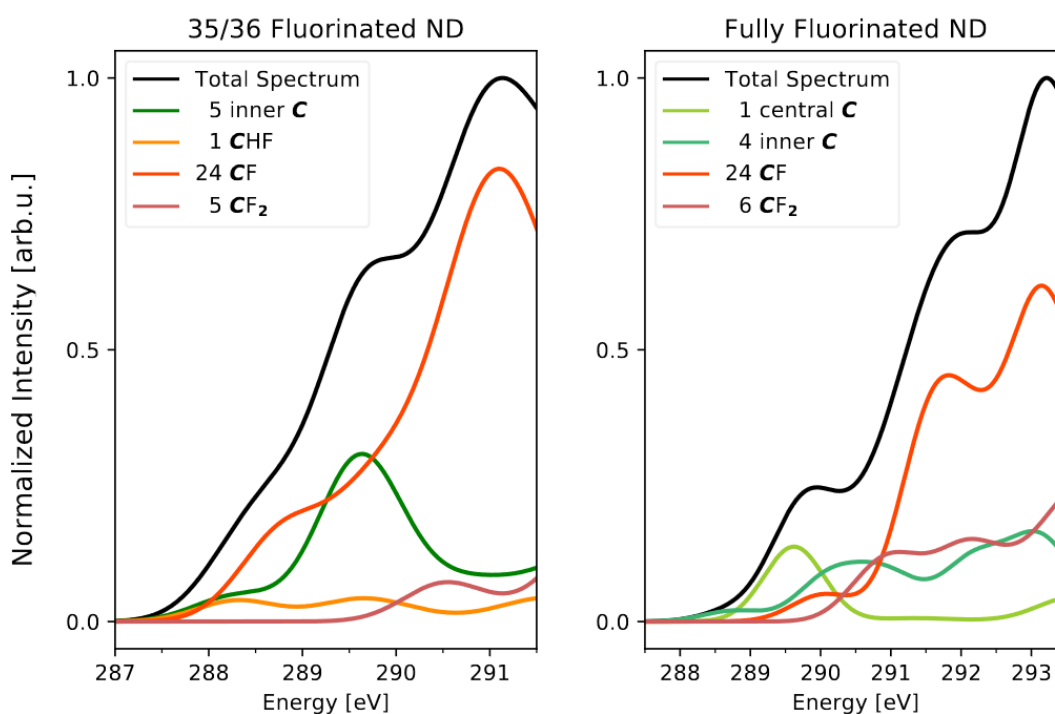

Figure A1.6: Composition of the XAS signals by functional groups in the DFT/ROCIS-calculated C K-edge spectra of the fluorinated nanodiamonds with 35/36 (left) and full (right) surface F content.

Frontier orbital energies of the randomly fluorinated nanodiamonds

The frontier orbital energies of the set of randomly fluorinated nanodiamonds are visualized in figure A1.7 (structures in figure 3.2). The figure contains the HOMO, LUMO, LUMO+1 and HOMO-LUMO gap energy (all in eV) of the nanodiamonds with increasing surface F content from left (0 %) to right (100 %).
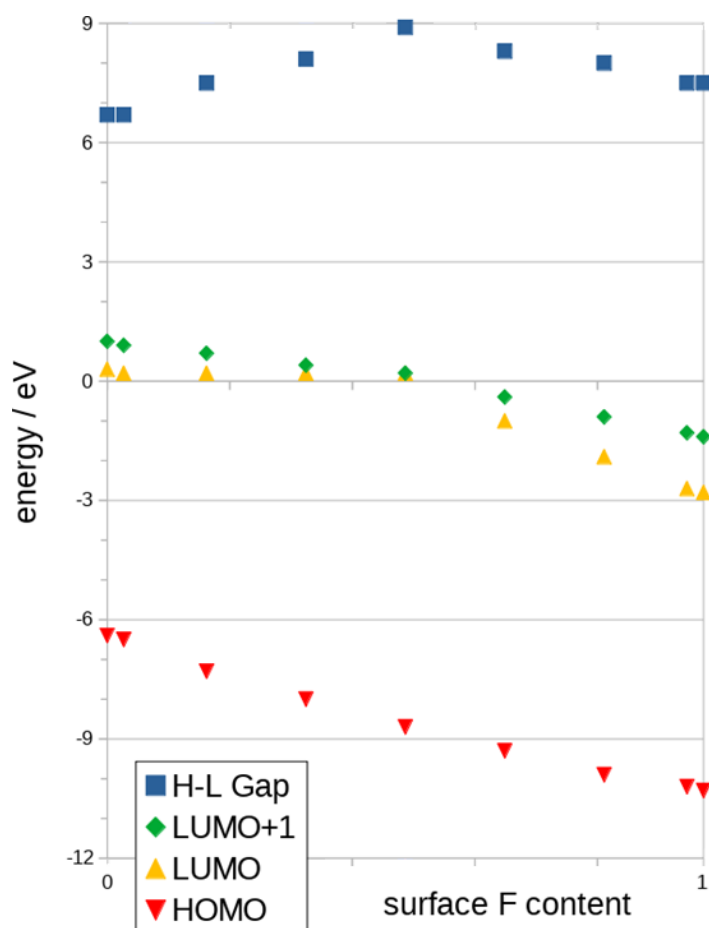

Figure A1.7: Frontier orbital energies (all in eV) of the set of randomly fluorinated nanodiamonds with increasing surface F content: HOMO-LUMO gap (blue squares), LUMO+1 (green diamonds), LUMO (yellow upward triangles), and HOMO (red downward triangles). The nanodiamond surface F content increases from left (0 %) to right (100 %).

DFT/ROCIS RIXS partial orbital space assessment

We here discuss the use of a restricted number of valence and virtual orbitals for the DFT/ROCIS RIXS calculations. Figure A1.8 shows two calculations on the tetrafluoromethane RIXS F K-edge which employ a different number of valence and virtual orbitals, respectively. All four F 1s orbitals are included in both calculations, and the 6 highest valence orbitals and the 50 lowest virtual orbitals (figure A1.8a) *vs.* the 4 highest valence orbitals and the 35 lowest virtual orbitals (figure A1.8b) are employed, respectively.

The spectral shapes obtained from both calculations are largely identical. Only, in the second spectrum (b) the signals are less resolved, especially for the signal at around 694 eV incident energy. Overall, employing a smaller orbital space has no significant effect on the resulting spectra. We thus conclude that the restricted orbital spaces that are employed in the calculations throughout the study will provide qualitatively reliable, semi-quantitative information. The amount of orbitals included in each calculation is individually determined, based on the size of the system and the concomitant computational effort.
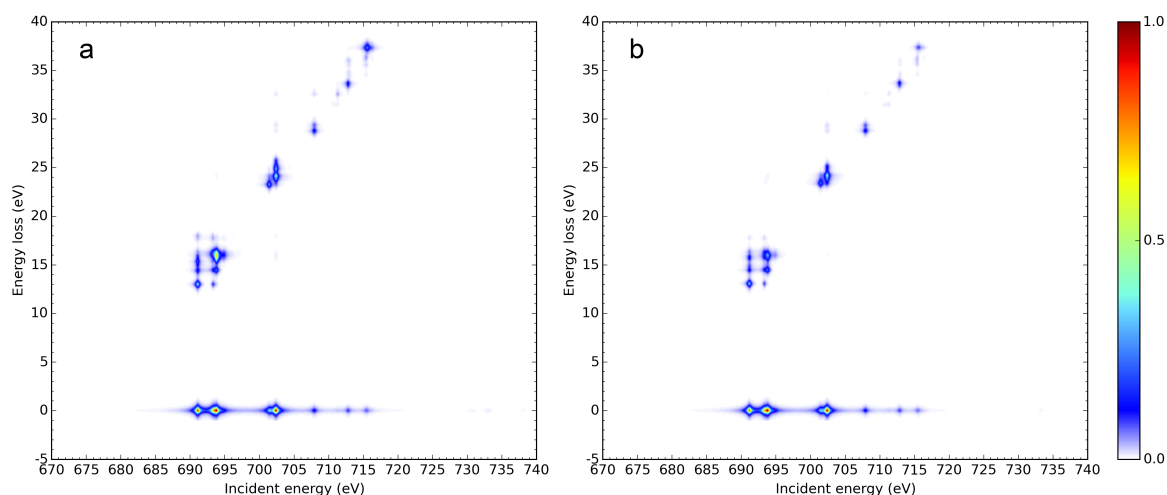

Figure A1.8: DFT/ROCIS RIXS F K-edge maps of tetrafluoromethane as a function of incident energy and energy loss (both in eV). The color scale indicates the signal intensity from low (blue) to high (red) in arbitrary, normalized units. (a) Calculation including 4 F core MOs, the 6 highest valence MOs and the 50 lowest virtual MOs. (b) Calculation including 4 F core MOs, the 4 highest valence MOs and the 35 lowest virtual MOs.

DFT/ROCIS RIXS F K-edge maps of fully fluorinated adamantane

In figure A1.9 we show the RIXS maps that were computed for the C-F fluorine's core orbitals of fully fluorinated adamantane, complementing the adamantane spectra that were given in figure 3.9. Each calculation includes a single core MO, the 60 highest valence orbitals and the 30 lowest virtual orbitals. The pattern of increasing energy loss and an inelastic scattering signal at constantly (around) 678.5 eV is the same as observed for the other fluorinated adamantanes' spectra (figure 8). Note that the main peak at 688.4 eV incident energy is not present in the spectrum obtained from core orbital 3 (figure A1.9d).
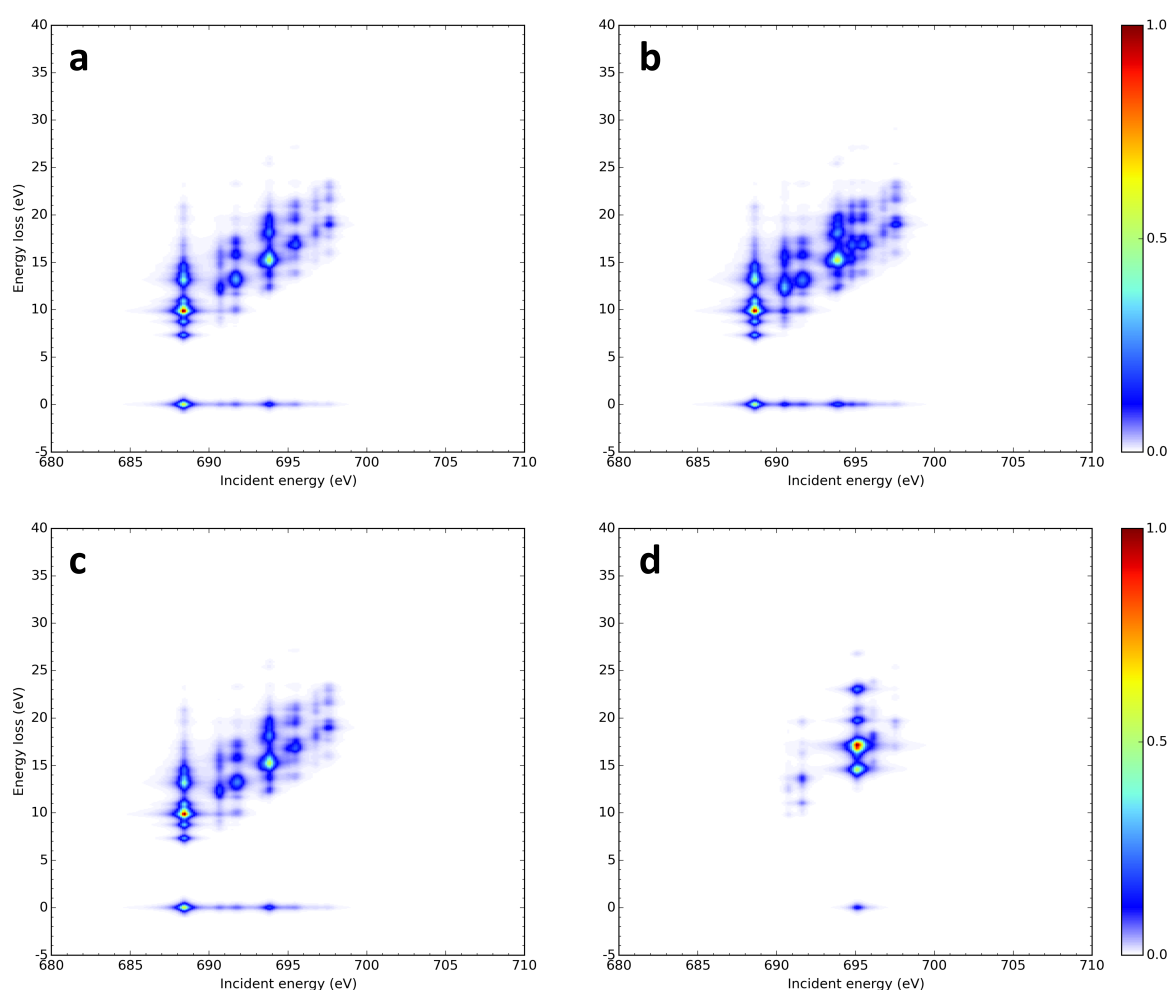

Figure A1.9: DFT/ROCIS RIXS F K-edge map of fully fluorinated adamantane from the lowest four F 1s core orbitals (a) 0, (b) 1, (c) 2, (d) 3. The color scale indicates the normalized signal intensity from low (blue) to high (red) in arbitrary units.

DFT/ROCIS RIXS F K-edge maps of the fluoromethanes

Figures A1.10–A1.13 depict the DFT/ROCIS RIXS maps of the fluoromethanes $CH_{4-n}F_n$ (n=1–4) at the F K-edge. These calculations employ a single F 1s core orbital each (as indicated in the captions), all valence orbitals, and the lowest 100 virtual orbitals, and allow a maximum of 5000 transitions. The maps of the fluoromethane (figure A1.10) and difluoromethane spectra (figure A1.11) show different signals with high energy losses (25–35 eV). The patterns do not accord with the signals that were observed experimentally for F-NDs. The maps of the trifluoromethane (figure A1.12) and tetrafluoromethane spectra (figure A1.13) show signals at an energy loss around 12 eV for the lowest excitation resonance, and the energy loss increases at higher incident energies. This pattern is the same as observed in the experimental spectrum of the F-NDs. Despite the fluoromethanes having much lower C/F ratios than F-NDs, this finding points towards a high fluorine content on the F-ND sample's surface.
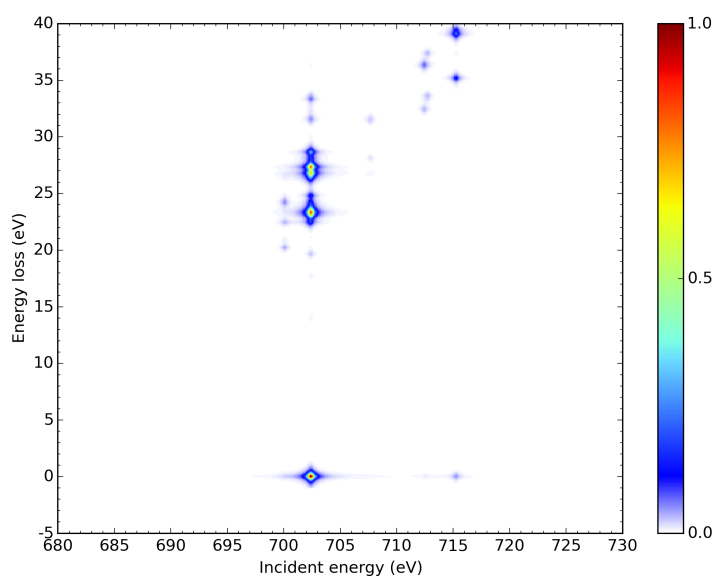

Figure A1.10: DFT/ROCIS RIXS F K-edge map of fluoromethane. The color scale indicates the normalized signal intensity from low (blue) to high (red) in arbitrary units.
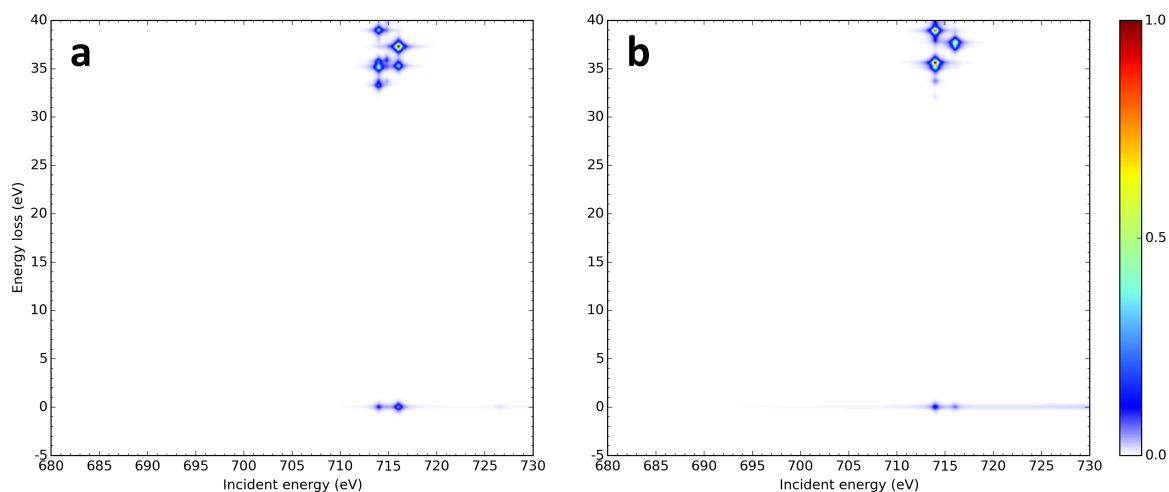
Figure A1.11: DFT/ROCIS RIXS F K-edge map of difluoromethane, excitation from core orbitals (a) 0 and (b) 1. The color scale indicates the normalized signal intensity from low (blue) to high (red) in arbitrary units.
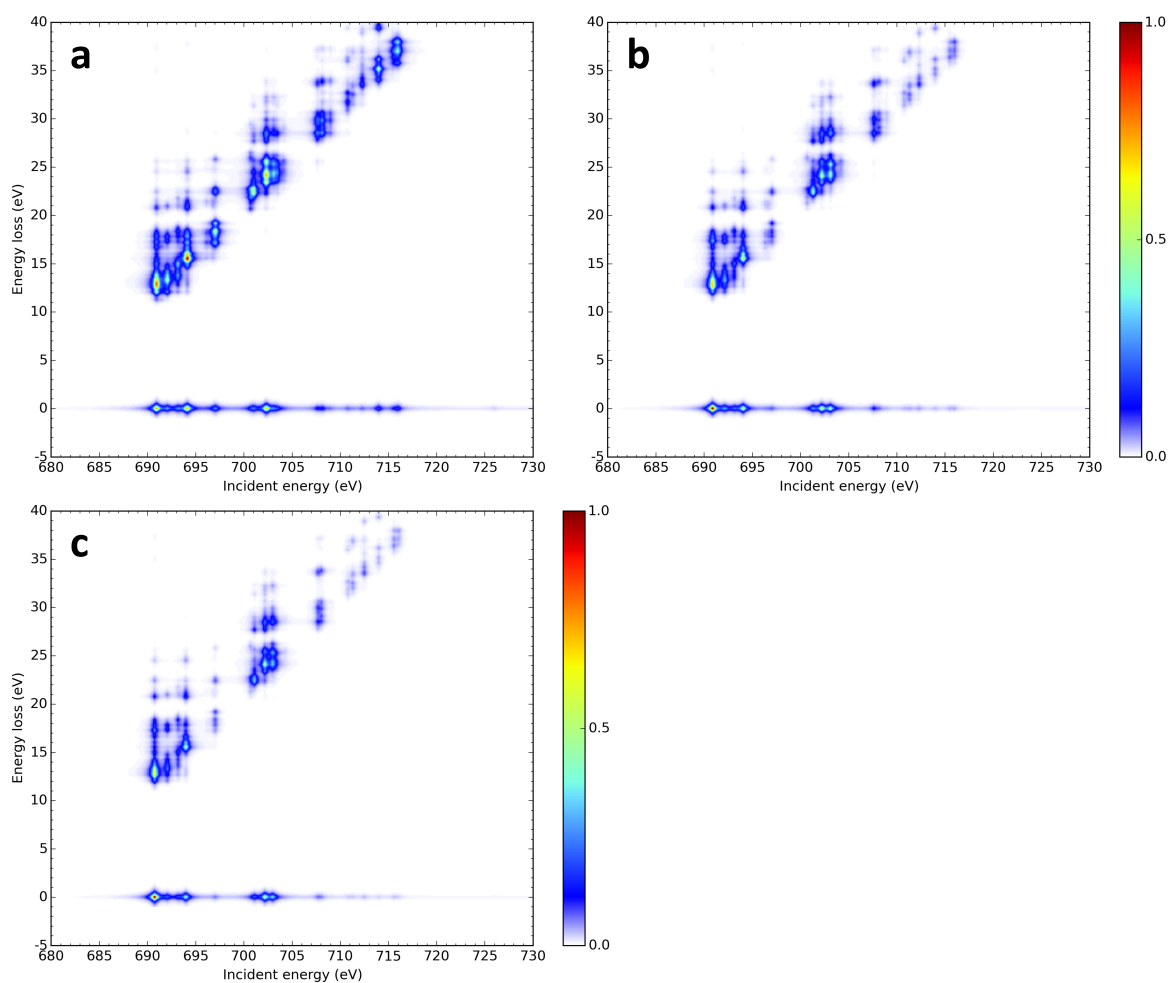
Figure A1.12: DFT/ROCIS RIXS F K-edge map of trifluoromethane, excitation from core orbitals (a) 0, (b) 1, (c) 2. The color scale indicates the normalized signal intensity from low (blue) to high (red) in arbitrary units.
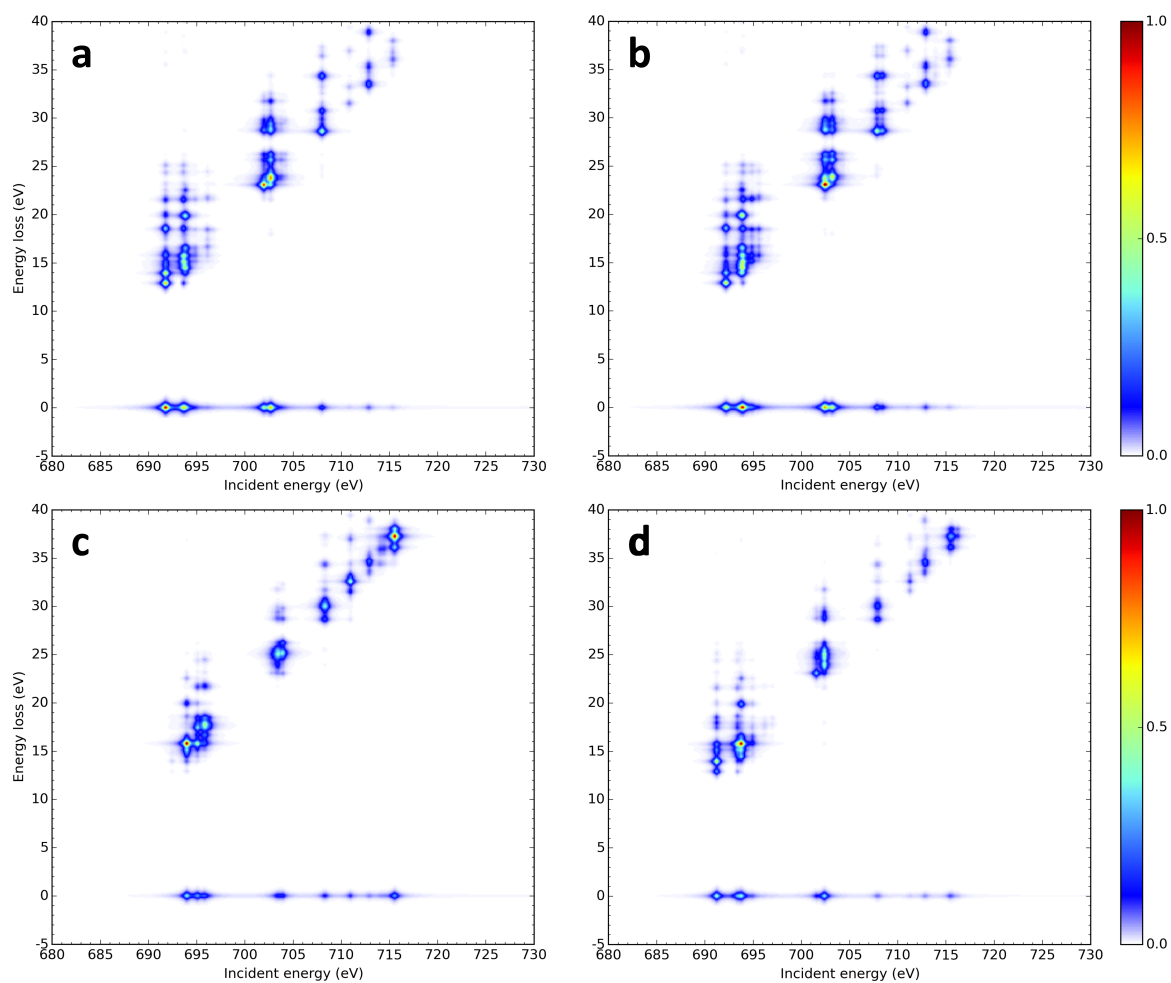
Figure A1.13: DFT/ROCIS RIXS F K-edge map of tetrafluoromethane, excitation from core orbitals (a) 0, (b) 1, (c) 2, (d) 3. The color scale indicates the normalized signal intensity from low (blue) to high (red) in arbitrary units.

Natural difference orbitals for the fluorinated adamantanes' RIXS F K-edge spectra

We show here the natural difference orbitals corresponding to the main peaks of the RIXS maps for the following (partially) fluorinated adamantanes (see figure 3.9): one CF fluorine surrounded by CF_2 moieties in figure A1.14; CF_2-functionalized adamantane in figures A1.15–A1.16; fully fluorinated adamantane (see above) in figures A1.17–A1.19. All contour surfaces [277] are plotted with orbital amplitudes $\pm$ 0.07. Each excitation occurs from the orbital shown on the left to the orbital shown on the right. Carbon atoms are represented in brown, hydrogen atoms in light grey, fluorine atoms in yellow.
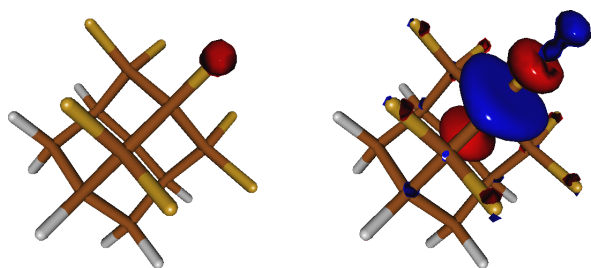

Figure A1.14: Natural difference orbitals corresponding to the main peak at 688.3 eV incident energy for the CF fluorine surrounded by CF_2 moieties in adamantane.
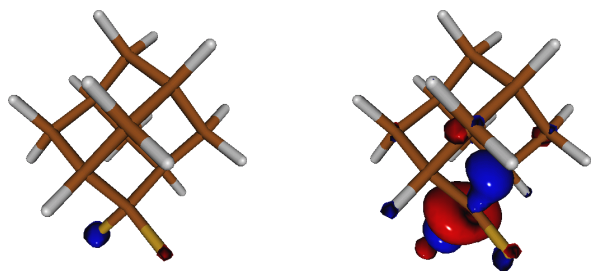
Figure A1.15: Natural difference orbitals corresponding to the main peak at 689.3 eV incident energy for the CF_2-functionalized adamantane.
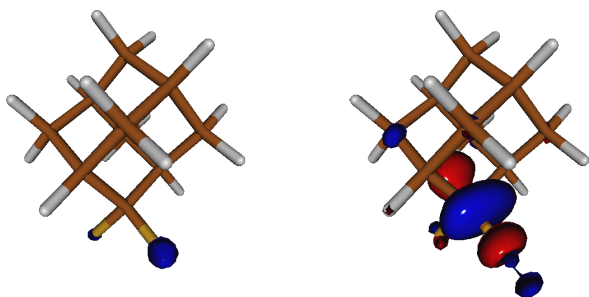
Figure A1.16: Natural difference orbitals corresponding to the main peak at 689.3 eV incident energy for the CF_2-functionalized adamantane.
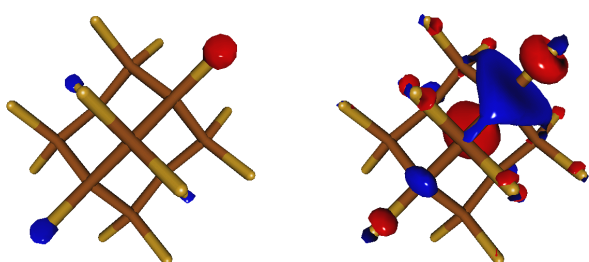
Figure A1.17: Natural difference orbitals corresponding to the main peak at around 688.4 eV incident energy for the spectrum from MO 0 of the fully fluorinated adamantane.
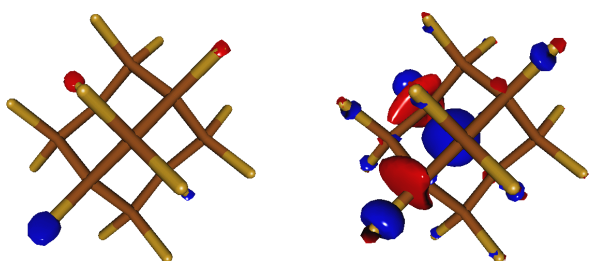
Figure A1.18: Natural difference orbitals corresponding to the main peak at around 688.4 eV incident energy for the spectrum from MO 1 of the fully fluorinated adamantane.
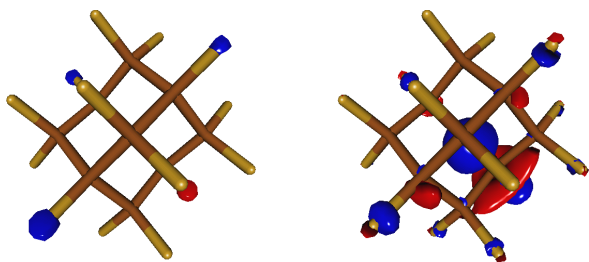
Figure A1.19: Natural difference orbitals corresponding to the main peak at around 688.4 eV incident energy for the spectrum from MO 2 of the fully fluorinated adamantane.

A2 Surface Transfer Doping at Nanodiamonds

This appendix contains information on the following items:

Diamondoid clusters: frontier orbital energies

Diamondoid clusters: frontier orbital shapes

Structures and unoccupied MOs of the FLR-covered ND-H $C_{170}H_{120}$

Structures and highest occupied MOs of the nanodiamonds $C_{84}H_{54}(OH)_{10}$,
$C_{84}H_{54}F_{10}$, $C_{55}H_{14}$ and $C_{27}H_{28}$

Surface transfer doping from $C_{84}H_{64-n}X_n$ (X = OH, F) (n = 8, 10) towards $O_2 \cdot H_2O$

Charge transfer excited state natural transition orbitals for $C_{35}H_{36}$ with a water
layer and different molecular adsorbates

Diamondoid clusters: frontier orbital energies

Numerous theoretical studies have been dedicated to investigations of the electronic properties of diamondoids and small nanodiamonds.[25,190,204,232,245,278–280] Furthermore, experimental works have determined the optical gaps of H-terminated diamondoids, however, different results have been obtained from different studies.[243,244,244] For these systems, zero-point energy gap renormalization (ZPR) corrections need to be considered when calculating the optical gaps to account for coupling to nuclear vibrations.[258] Here, the H-terminated diamondoid molecules, their dimers and larger clusters are investigated to quantify the concomitant electronic structure changes. These structures serve as model systems for larger high-quality, H-terminated nanodiamonds which are used, *i.e.*, in photocatalysis.

Table A2.1 summarizes the monomer HOMO, LUMO, HOMO-LUMO gap and dimer HOMO-LUMO gap energies obtained from DFT, and the optical gap values obtained from different experiments.[243,244,244] In the first two experiments (referred to as exp. 1[244] and exp. 2[243]) optical absorption measurements are conducted in the gas phase, while in the third experiment (exp. 3)[243] X-ray emission and absorption spectra are obtained from powders.

The optical gap values decrease with increasing size of the diamondoids, from adamantane $C_{10}H_{16}$ (ca. 6.0–6.5 eV in experiments) to the C_{26} diamondoids (ca. 5.5–6.0 eV in experiments), according to the quantum size effect.[243] Upon dimer formation, the DFT-calculated HOMO-LUMO gaps are reduced by 0.08–0.30 eV. Generally, the monomer HOMO-LUMO gaps are in close agreement with the experimental optical gaps obtained in the gas phase (exp. 1 and 2). The optical gaps obtained from exp. 3, however, are up to 0.65 eV lower than those from exp. 1 and 2. This can be explained by the fact that only exp. 3 used measurements on powders, in which the diamondoid molecules form large clusters leading to lower optical gaps of the joint systems.

The HOMO-LUMO gaps further decrease for larger cluster sizes, as shown for the (adamantane)$_n$ clusters in table A2.2. The DFT results predict a gap decrease of 0.54 eV when going from single adamantane to the (adamantane)$_5$ cluster, which is in excellent agreement with previous GW-corrected GGA-DFT calculations of crystalline adamantane.[281] Interestingly, the calculations indicate that the reduction of the gap mostly originates from a lowering of the LUMO energies. In contrast, the HOMO energy is slightly increased when adding the second adamantane unit and stays approximately constant thereafter.

Table A2.1: Calculated (TPSSH-D3/ma-SVP) and experimental electronic properties of diamondoids: Diamondoid name; sum formula, point group (PG); monomer HOMO and LUMO energies, zero-point energy gap normalization (ZPR), monomer HOMO-LUMO-gap energy, dimer HOMO-LUMO-gap energy; experimental optical gaps (all in eV). The calculated gaps that are compared to the experimental values are highlighted in bold. Note that for diamantane and [121]tetramantane the DFT HOMO-LUMO gaps may fail to approximate the optical gap, because here the HOMO-LUMO transitions are symmetry-forbidden.

Diamondoid	Sum	PG	E_{HOMO}	E_{LUMO}	$ZPR^{[258]}$	$E_{Gap}^{Monomer}$	E_{Gap}^{Dimer}	$E_{Gap}^{Exp.1\,[244]}$	$E_{Gap}^{Exp.2\,[245]}$	$E_{Gap}^{Exp.3\,[243]}$
Adamantane	$C_{10}H_{16}$	T_d	−7.17	−0.03	−0.33	**6.81**	**6.57**	6.49	6.55	6.03
Diamantane	$C_{14}H_{20}$	D_{3d}	−6.77	−0.08	−0.12	**6.57**	**6.32**	6.40	6.47	5.82
Triamantane	$C_{18}H_{24}$	C_{2v}	−6.51	−0.18	−0.23	**6.10**	**6.01**	6.06	6.10	5.68
[123]Tetramantane	$C_{22}H_{28}$	C_2	−6.40	−0.19	−0.20	**6.01**	**5.89**	5.95	5.98	5.60–5.65
[121]Tetramantane	$C_{22}H_{28}$	C_{2h}	−6.32	−0.20	−0.26	**5.86**	**5.78**	6.10	6.15	5.60–5.65
[1(2)3]Tetramantane	$C_{22}H_{28}$	C_{3v}	−6.42	−0.23	−0.32	**5.87**	**5.77**	5.94	5.96	5.60–5.65
[1(2,3)4]Pentamantane	$C_{26}H_{32}$	T_d	−6.37	−0.27	−0.27	**5.83**	**5.64**	5.81	5.85	5.54
[1212]Pentamantane	$C_{26}H_{32}$	C_{2v}	−6.17	−0.20	−0.26	**5.71**	**5.62**	5.85	5.90	5.51
[1231]Hexamantane	$C_{26}H_{30}$	D_{3d}	−6.21	−0.23	−0.30	**5.68**	**5.56**	5.88	5.91	5.54

Table A2.2: Calculated (TPSSH-D3/ma-SVP) electronic properties of adamantane clusters with up to n=5 adamantane units: Highest occupied molecular orbital (HOMO), lowest unoccupied molecular orbital (LUMO), and HOMO-LUMO gap energies (all in eV). ZPR correction of −0.33 eV is applied to all gap calculations.

n	E_{HOMO}	E_{LUMO}	E_{Gap}
1	-7.17	-0.03	**6.81**
2	-7.03	-0.13	**6.57**
3	-7.06	-0.36	**6.37**
4	-7.05	-0.41	**6.31**
5	-7.04	-0.44	**6.27**

Diamondoid clusters: frontier orbital shapes

Diamondoids and small nanodiamonds are known to have uniquely shaped frontier orbitals.[204,232] Especially, the LUMO and LUMOs+n (n = 1, 2, ...) of spherical nanodiamonds resemble atomic s, p, d, ... orbitals. Han *et al.* proposed that these orbital shapes can generally be expected if (i) an outwards-pointing surface dipole is present, (ii) the system has spherical symmetry, and (iii) a dielectric mismatch exists between nanoparticle and vacuum.[204] This section investigates the corresponding orbitals of the diamondoid clusters.

Figure A2.1 depicts the structure and HOMO, LUMO and LUMOs+n contour plots of the (adamantane)$_5$ cluster. All frontier orbitals are highly delocalized and extend over the whole cluster structure. The orbital shapes are similar to those of the isolated adamantane molecule,[204,232] but stretched according to the shape of the cluster. They still clearly resemble atomic orbitals (LUMO: s, LUMO+(1–3): p, LUMO+(4–8): d, LUMO+9: f).

The same frontier orbital types were found for all further investigated clusters, including mixed clusters of different diamondoids, such as adamantane-hexamantane, triamantane-[1212]pentamantane and diamantane-[123]tetramantane-[1(2,3)4]pentamantane. This observation clearly indicates that strict spherical symmetry of the system, the previous requirement (i),[204] is not necessary to observe these unique LUMO shapes. Instead, both single molecules and aggregates of T_d-symmetrical and less symmetric diamondoids (*e.g.*, triamantane, C_{2v}) all show this type of frontier orbitals. Interestingly, we found that clusters of rare gas atoms such as (Ar)$_4$ show the same type of joint LUMOs at this level of theory.

For the cases of non-mixed dimers and clusters (identical molecules), also the HOMO and HOMOs−n (n ≥ 5) are delocalized and spread out over the whole respective cluster. For the mixed diamondoid aggregates, these orbitals are partly localized at a single molecule and partly delocalized over several molecules. This finding confutes the previous assumption that no electron delocalization occurs between the different molecules of a diamondoid cluster.[242]
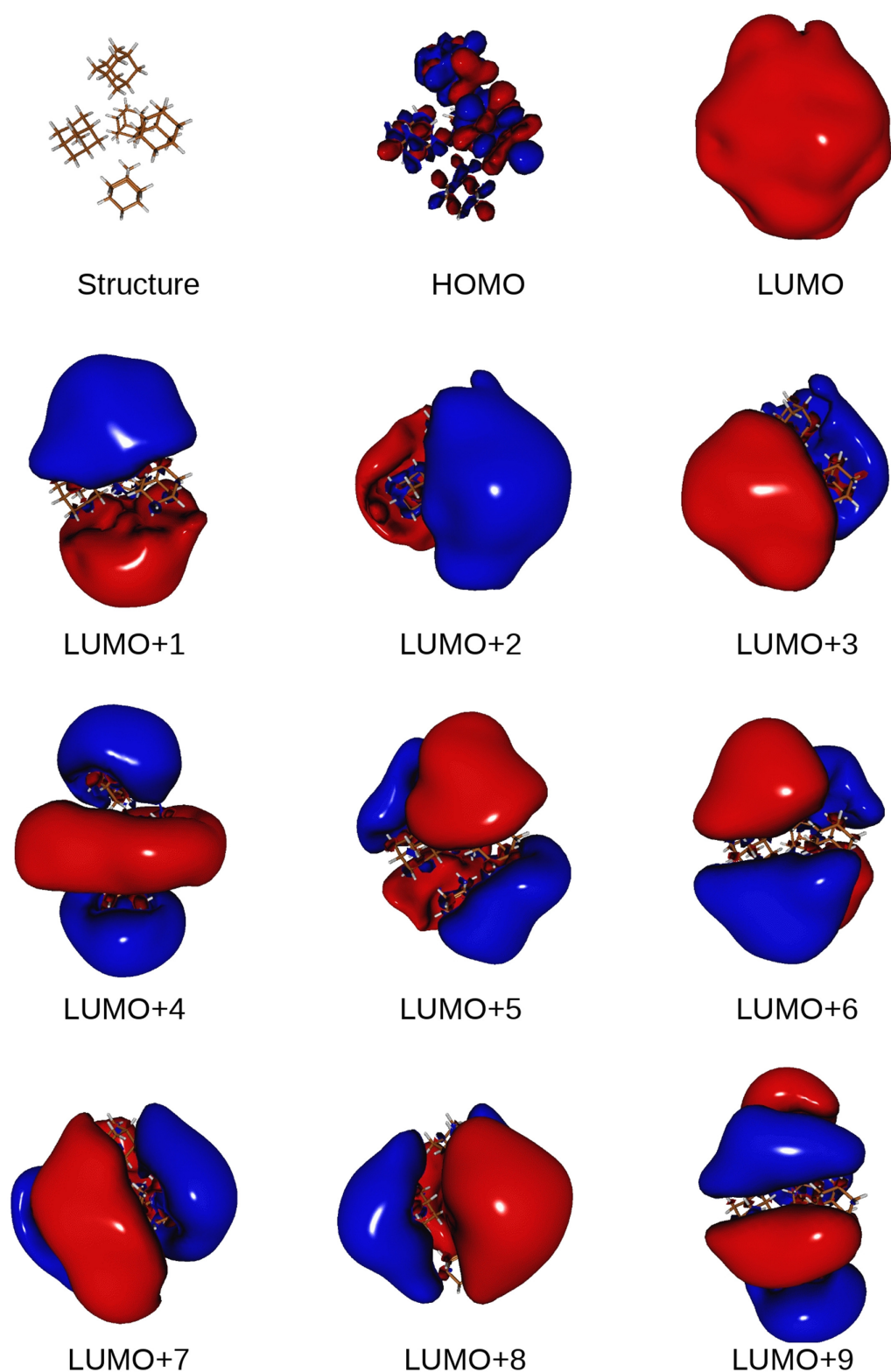
Figure A2.1: Structure, HOMO, LUMO and LUMOs+n of the (adamantane)$_5$ cluster (DFT TPSSH-D3/ma-SVP) with its orientation fixed in all frames. Contour surfaces are plotted for orbital amplitudes ± 0.005.

Structures and unoccupied MOs of the FLR-covered ND-H $C_{170}H_{120}$

ND $C_{170}H_{120}$	$C_{204}H_{104}$	$C_{230}H_{106}$	$C_{243}H_{84}$	$C_{286}H_{68}$
0 %	12 %	21 %	26 %	41 %
LUMO	LUMO	LUMO	LUMO	LUMO
E = +0.93 eV	E = −2.58 eV	E = −2.90 eV	E = −3.53 eV	E = −3.95 eV
	LUMO+10	LUMO+17	LUMO+19	LUMO+35
	E = +0.64 eV	E = +0.75 eV	E = +0.40 eV	E = −0.03 eV
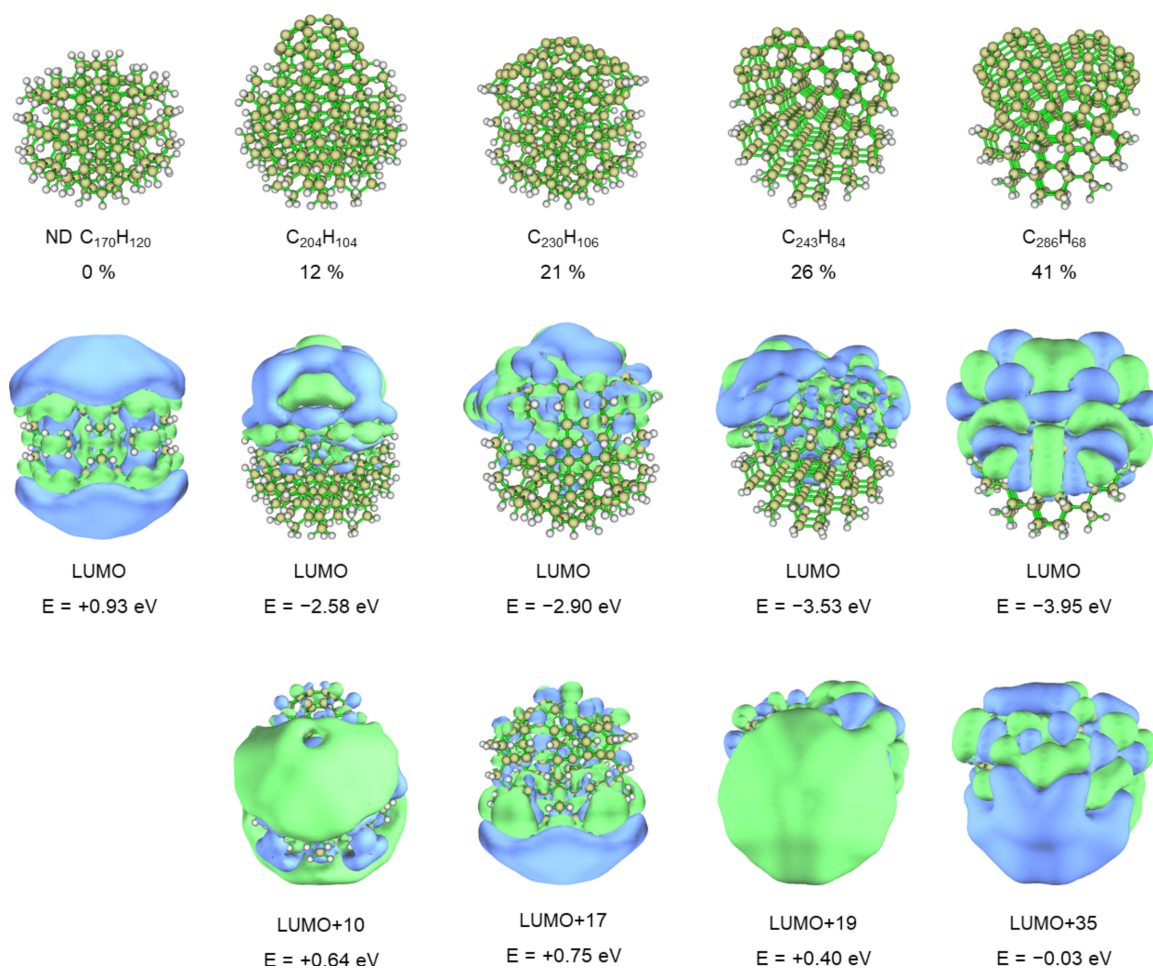
Figure 6.2: Structures, sum formulae, C_{FLR} coverage (in atom%) and unoccupied orbital shapes of the ND-H/-FLR structure series. C atoms in yellow, H atoms in light grey, bonds in green, orbital contour plots of isovalue ± 0.002.

Structures and highest occupied MOs of the nanodiamonds $C_{84}H_{54}(OH)_{10}$, $C_{84}H_{54}F_{10}$, $C_{55}H_{14}$ and $C_{27}H_{28}$

	structure	HOMO	HOMO−1	HOMO−2

a

b

c
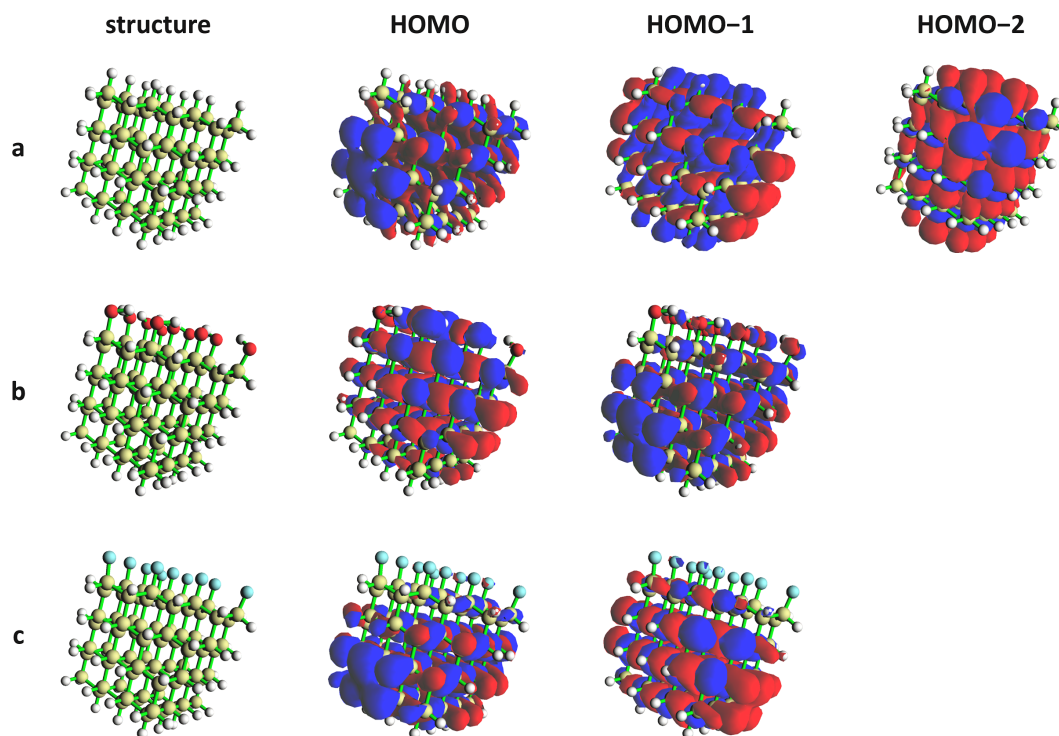
Figure 6.3: Structure and the threefold/twofold degenerate HOMO of the nanodiamonds (a) $C_{84}H_{64}$, (b) $C_{84}H_{54}(OH)_{10}$, and (c) $C_{84}H_{54}F_{10}$. Contour plots of isovalue ± 0.01.

a

b

	structure	HOMO	HOMO−1	HOMO−2
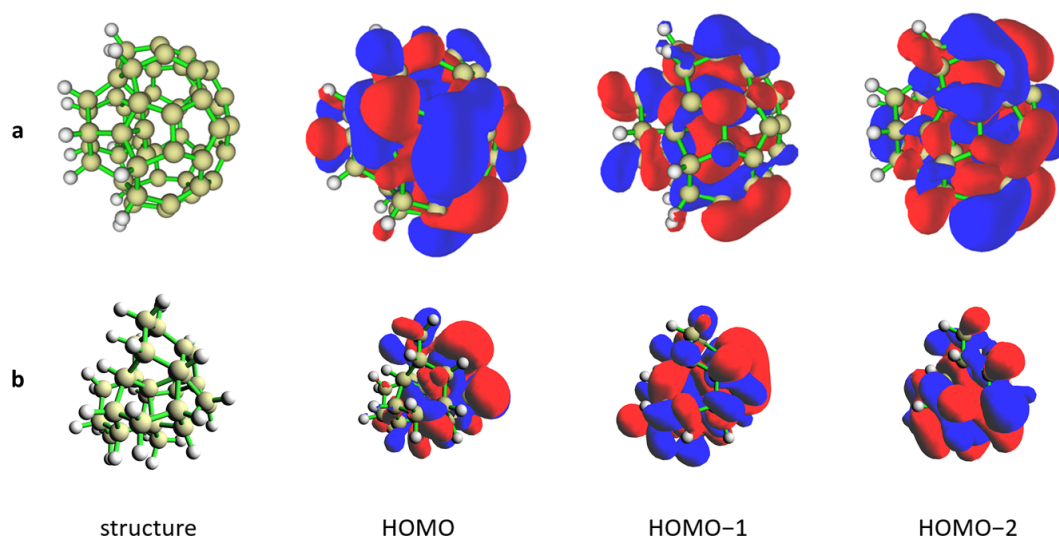
Figure 6.4: Structure and the three highest occupied MOs of the nanodiamonds partially covered by amorphous carbon (a) $C_{55}H_{14}$ and (b) $C_{27}H_{28}$. Contour plots of isovalue ± 0.01.

Surface transfer doping from $C_{84}H_{64-n}X_n$ (X = OH, F) (n = 8, 10) towards $O_2 \cdot H_2O$

Table A2.3: Charge transfer (CT) from four different nanodiamonds with randomly spread functionalization towards the adsorbate $O_2 \cdot H_2O$ at three random positions a, b, c, quantified by the transferred Hirshfeld charge (in elemental unit charge e). The nanodiamonds include two partially hydroxylated structures $C_{84}H_{54}(OH)_8$ and $C_{84}H_{54}(OH)_{10}$, and two partially fluorinated structures $C_{84}H_{54}F_8$ and $C_{84}H_{54}F_{10}$.

Nanodiamond	Adsorbate	Adsorbate Position	CT (e)
$C_{84}H_{56}(OH)_8$	$O_2 \cdot H_2O$	a	0.38
		b	0.40
		c	0.38
$C_{84}H_{56}F_8$	$O_2 \cdot H_2O$	a	0.35
		b	0.35
		c	0.33
$C_{84}H_{54}(OH)_{10}$	$O_2 \cdot H_2O$	a	0.37
		b	0.40
		c	0.39
$C_{84}H_{56}F_{10}$	$O_2 \cdot H_2O$	a	0.33
		b	0.32
		c	0.30

Charge transfer excited state natural transition orbitals for $C_{35}H_{36}$ with a water layer and different molecular adsorbates

H_2O

N_2O

CO_2

structure   hole   electron
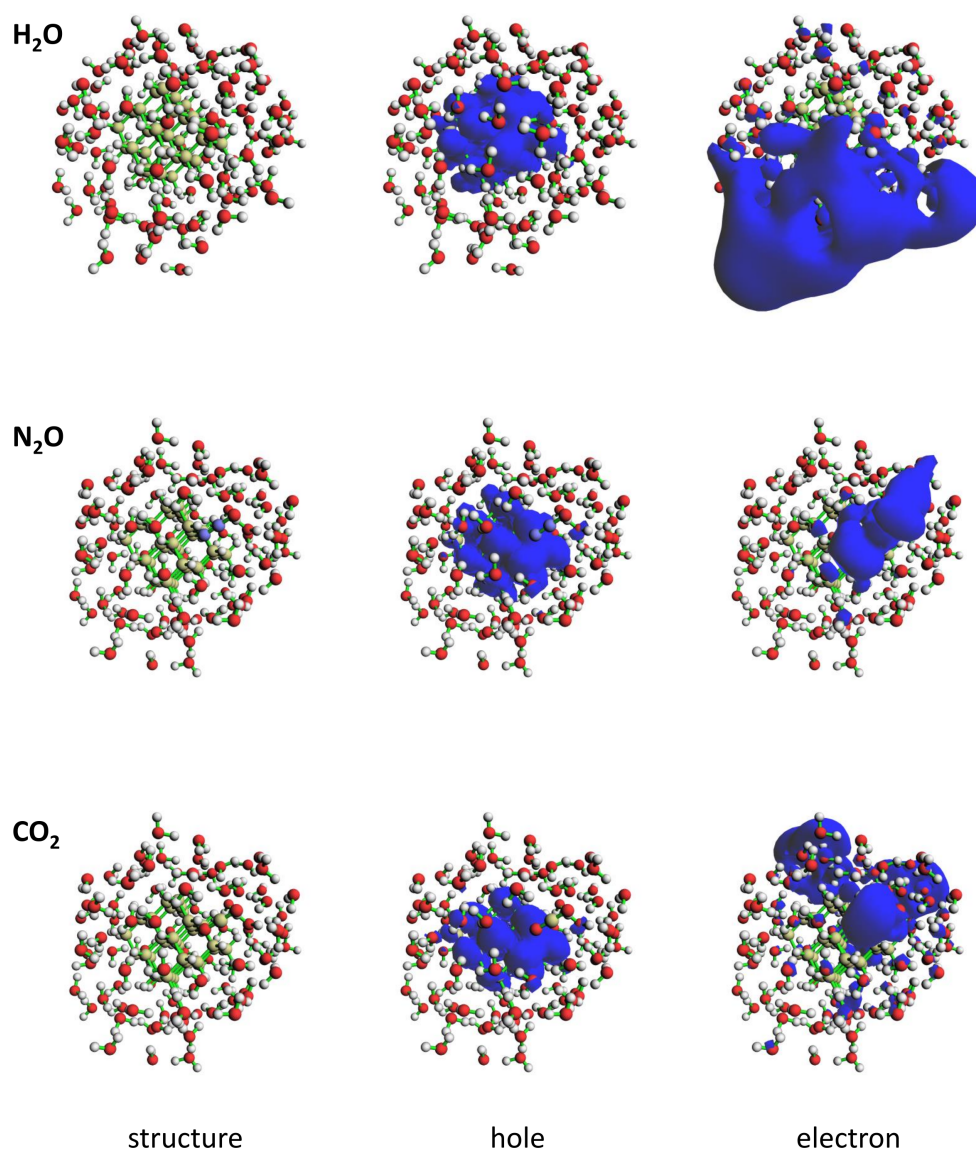
Figure A2.5: Structure and charge transfer excited state natural transition orbitals (hole and electron) for $C_{35}H_{36}$ with an explicit water layer and (from top to bottom) no adsorbate (H_2O), nitrous oxide (N_2O), and carbon dioxide (CO_2). The respective adsorbate is located in front of the nanodiamond (*cf.* figure 4.6).

O$_2$

O$_3$

Na$_2$SO$_3$

Na$_2$SO$_4$

structure   hole   electron
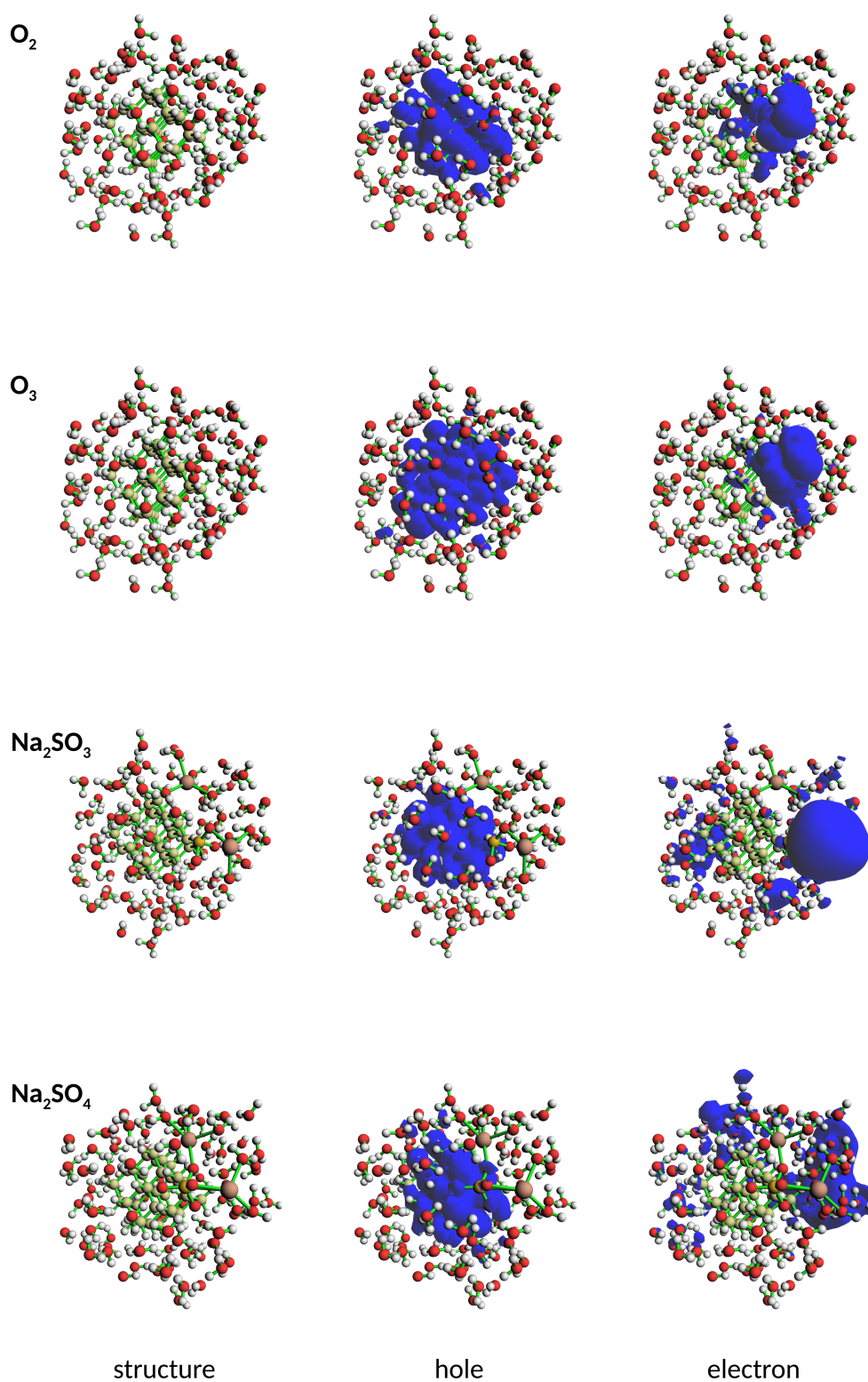
Figure A2.6: Structure and charge transfer excited state natural transition orbitals (hole and electron) for C$_{35}$H$_{36}$ with an explicit water layer and (from top to bottom) oxygen (O$_2$), ozone (O$_3$), sodium sulfite (Na$_2$SO$_3$) or sodium sulfate (Na$_2$SO$_4$). The respective adsorbate is located in front of the nanodiamond (*cf.* figure 4.6).

A3 Machine Learning Frontier Orbital Energies of Nanodiamonds

This appendix contains information on the following items:

Base structures of the ND5k data set

DFTB geometry optimization of nanodiamond structures

def2-SVP basis set for single point calculations

Frontier orbitals of P-doped nanoadiamonds for photocatalysis

Trends in the ND5k data set

Details of the machine learning setups

Correlations between nanodiamond size and HOMO/LUMO energy

Bibliography

[1] M. Green, E. Dunlop, J. Hohl-Ebinger, M. Yoshita, N. Kopidakis and X. Hao, *Prog. Photovolt. Res. Appl.*, 2021, **29**, 3–15.

[2] Y. Cheng and L. Ding, *SusMat*, 2021, **1**, 324–344.

[3] A. Qazi, F. Hussain, N. A. Rahim, G. Hardaker, D. Alghazzawi, K. Shaban and K. Haruna, *IEEE Access*, 2019, **7**, 63837–63851.

[4] E. T. Sayed, A. G. Olabi, A. H. Alami, A. Radwan, A. Mdallal, A. Rezk and M. A. Abdelkareem, *Energies*, 2023, **16**, 1415.

[5] J. Janek and W. G. Zeier, *Nat. Energy*, 2023, **8**, 230–240.

[6] J. A. Turner, *Science*, 2004, **305**, 972–974.

[7] B. Shadidi, G. Najafi and T. Yusaf, *Energies*, 2021, **14**, 6209.

[8] X. Liu, J. Xiao, H. Peng, X. Hong, K. Chan and J. K. Nørskov, *Nat. Commun.*, 2017, **8**, 15438.

[9] B. Wayland and X. Fu, *Science*, 2006, **311**, 790–791.

[10] C. D. Feldt, T. Gimm, R. Moreira, W. Riedel and T. Risse, *Phys. Chem. Chem. Phys.*, 2021, **23**, 21599–21605.

[11] C. D. Feldt, T. Kirschbaum, J. L. Low, W. Riedel and T. Risse, *Catal. Sci. Technol.*, 2022, **12**, 1418–1428.

[12] C. Hepburn, E. Adlen, J. Beddington, E. A. Carter, S. Fuss, N. Mac Dowell, J. C. Minx, P. Smith and C. K. Williams, *Nature*, 2019, **575**, 87–97.

[13] D. Astruc, *Chem. Rev.*, 2020, **120**, 461–463.

[14] L.-X. Su, Y. Cao, H.-S. Hao, Q. Zhao and J. Zhi, *Funct. Diam.*, 2022, **1**, 93–109.

[15] V. N. Mochalin, O. Shenderova, D. Ho and Y. Gogotsi, *Nat. Nanotechnol.*, 2012, **7**, 11–23.

[16] D. M. Jang, Y. Myung, H. S. Im, Y. S. Seo, Y. J. Cho, C. W. Lee, J. Park, A.-Y. Jee and M. Lee, *Chem. Commun.*, 2012, **48**, 696–698.

[17] D. Zhu, L. Zhang, R. E. Ruther and R. J. Hamers, *Nat. Mater.*, 2013, **12**, 836–841.

[18] L. Zhang, D. Zhu, G. M. Nathanson and R. J. Hamers, *Angew. Chem. Int. Ed.*, 2014, **53**, 9746–9750.

[19] D. Zhu, J. A. Bandy, S. Li and R. J. Hamers, *Surf. Sci.*, 2016, **650**, 295–301.

[20] J. A. Bandy, D. Zhu and R. J. Hamers, *Diam. Relat. Mater.*, 2016, **64**, 34–41.

[21] L. Zhang and R. J. Hamers, *Diam. Relat. Mater.*, 2017, **78**, 24–30.

[22] L.-X. Su, Q. Lou, C.-X. Shan, D.-L. Chen, J.-H. Zang and L.-J. Liu, *Appl. Surf. Sci.*, 2020, **525**, 146576.

[23] S. Aranifard and A. Shojaei, *Diam. Relat. Mater.*, 2018, **89**, 301–311.

[24] D. J. Bergenstock and J. M. Maskulka, *Bus. Horiz.*, 2001, **44**, 37–44.

[25] M. Vörös, T. Demjén and A. Gali, *MRS Proc.*, 2011, **1370**, mrss11–1370–yy02–07.

[26] Y.-T. Wang, Y.-J. Zhao, J.-H. Liao and X.-B. Yang, *J. Chem. Phys.*, 2018, **148**, 014306.

[27] T. M. Willey, C. Bostedt, T. van Buuren, J. E. Dahl, S. G. Liu, R. M. K. Carlson, L. J. Terminello and T. Möller, *Phys. Rev. Lett.*, 2005, **95**, 113401.

[28] S. Stehlik, M. Varga, M. Ledinsky, V. Jirasek, A. Artemenko, H. Kozak, L. Ondic, V. Skakalova, G. Argentero, T. Pennycook, J. C. Meyer, A. Fejfar, A. Kromka and B. Rezek, *J. Phys. Chem. C*, 2015, **119**, 27708–27720.

[29] S. Park, I. I. Abate, J. Liu, C. Wang, J. E. P. Dahl, R. M. K. Carlson, L. Yang, V. B. Prakapenka, E. Greenberg, T. P. Devereaux, C. Jia, R. C. Ewing, W. L. Mao and Y. Lin, *Sci. Adv.*, 2020, **6**, eaay9405.

[30] T. Berg, E. Marosits, J. Maul, P. Nagel, U. Ott, F. Schertz, S. Schuppler, C. Sudek and G. Schönhense, *J. Appl. Phys*, 2008, **104**, 064303.

[31] U. Ott, *J. Achiev. Mater. Manuf. Eng.*, 2009, **37**, 779–784.

[32] J. E. Dahl, S. G. Liu and R. M. K. Carlson, *Science*, 2003, **299**, 96–99.

[33] S. Stauss and K. Terashima, *Diamondoids: Synthesis, Properties, and Applications*, Jenny Stanford Publishing, New York, 2017.

[34] V. A. Plotnikov, S. V. Makarov, D. G. Bogdanov and A. S. Bogdanov, *AIP Conf. Proc.*, 2016, **1785**, 040045.

[35] Y. Liu, Z. Gu, J. L. Margrave and V. N. Khabashesku, *Chem. Mater.*, 2004, **16**, 3924–3930.

[36] V. Pichot, M. Comet, E. Fousson, C. Baras, A. Senger, F. Le Normand and D. Spitzer, *Diam. Relat. Mater.*, 2008, **17**, 13–22.

[37] J. Ackermann and A. Krueger, *Nanoscale*, 2019, **11**, 8012–8019.

[38] A. N. Hegyi and E. Yablonovitch, 2012 Annual International Conference of the IEEE Engineering in Medicine and Biology Society, 2012, pp. 2639–2642.

[39] E. Perevedentseva, Y.-C. Lin, M. Jani and C.-L. Cheng, *Nanomedicine*, 2013, **8**, 2041–2060.

[40] Y.-Y. Liu, B.-M. Chang and H.-C. Chang, *Nanomedicine*, 2020, **15**, 1599–1616.

[41] H. Huang, E. Pierstorff, E. Osawa and D. Ho, *Nano Lett.*, 2007, **7**, 3305–3314.

[42] M. Chen, E. D. Pierstorff, R. Lam, S.-Y. Li, H. Huang, E. Osawa and D. Ho, *ACS Nano*, 2009, **3**, 2016–2022.

[43] A. Alhaddad, M.-P. Adam, J. Botsoa, G. Dantelle, S. Perruchas, T. Gacoin, C. Mansuy, S. Lavielle, C. Malvy, F. Treussart and J.-R. Bertrand, *Small*, 2011, **7**, 3087–3095.

[44] G. Xi, E. Robinson, B. Mania-Farnell, E. F. Vanin, K.-W. Shim, T. Takao, E. V. Allender, C. S. Mayanil, M. B. Soares, D. Ho and T. Tomita, *Nanomedicine*, 2014, **10**, 381–391.

[45] V. Acosta and P. Hemmer, *MRS Bull.*, 2013, **38**, 127–130.

[46] A. Akther, E. P. Walsh, P. Reineck, B. C. Gibson, T. Ohshima, H. Abe, G. McColl, N. L. Jenkins, L. T. Hall, D. A. Simpson, A. R. Rezk and L. Y. Yeo, *Anal. Chem.*, 2021, **93**, 16133–16141.

[47] Y. Wu and T. Weil, *Adv. Sci.*, 2022, **9**, 2200059.

[48] J.-Y. Lee and D.-S. Lim, *Surf. Coat. Technol.*, 2004, **188-189**, 534–538.

[49] C. C. Chou and S. H. Lee, *J. Mater. Process. Technol.*, 2008, **201**, 542–547.

[50] C.-C. Chou and S.-H. Lee, *Wear*, 2010, **269**, 757–762.

[51] H. Wang and Y. Cui, *Carbon Energy*, 2019, **1**, 13–18.

[52] A. P. Gaiduk, T. A. Pham, M. Govoni, F. Paesani and G. Galli, *Nat. Commun.*, 2018, **9**, 247.

[53] F. Ambrosio, Z. Guo and A. Pasquarello, *J. Phys. Chem. Lett.*, 2018, **9**, 3212–3216.

[54] J. B. Cui, J. Ristein and L. Ley, *Phys. Rev. B*, 1999, **60**, 16135–16142.

[55] F. Buchner, T. Kirschbaum, A. Venerosy, H. Girard, J.-C. Arnault, B. Kiendl, A. Krueger, K. Larsson, A. Bande, T. Petit and C. Merschjann, *Nanoscale*, 2022, **14**, 17188–17195.

[56] W. Zhu, G. P. Kochanski and S. Jin, *Science*, 1998, **282**, 1471–1473.

[57] S. Choudhury, B. Kiendl, J. Ren, F. Gao, P. Knittel, C. Nebel, A. Venerosy, H. Girard, J.-C. Arnault, A. Krueger, K. Larsson and T. Petit, *J. Mater. Chem. A*, 2018, **6**, 16645–16654.

[58] P. Knittel, F. Buchner, E. Hadzifejzovic, C. Giese, P. Quellmalz, R. Seidel, T. Petit, B. Iliev, T. J. S. Schubert, C. E. Nebel and J. S. Foord, *ChemCatChem*, 2020, **12**, 5548–5557.

[59] S. Li, J. A. Bandy and R. J. Hamers, *ACS Appl. Mater. Interfaces*, 2018, **10**, 5395–5403.

[60] J. R. Christianson, D. Zhu, R. J. Hamers and J. R. Schmidt, *J. Phys. Chem. B*, 2014, **118**, 195–203.

[61] S. A. Fischer, W. R. Duncan and O. V. Prezhdo, *J. Am. Chem. Soc.*, 2009, **131**, 15483–15491.

[62] M. Pizzochero, F. Ambrosio and A. Pasquarello, *Chem. Sci.*, 2019, **10**, 7442–7448.

[63] J. Wilhelm, J. VandeVondele and V. V. Rybkin, *Angew. Chem. Int. Ed.*, 2019, **58**, 3890–3893.

[64] O. Marsalek, F. Uhlig, J. VandeVondele and P. Jungwirth, *Acc. Chem. Res.*, 2012, **45**, 23–32.

[65] B. F. Bachman, D. Zhu, J. Bandy, L. Zhang and R. J. Hamers, *ACS Meas. Au*, 2021, 46–56.

[66] Y. Ma, N. Wassdahl, P. Skytt, J. Guo, J. Nordgren, P. D. Johnson, J.-E. Rubensson, T. Boske, W. Eberhardt and S. D. Kevan, *Phys. Rev. Lett.*, 1992, **69**, 2598–2601.

[67] X. Gao, L. Liu, D. Qi, S. Chen, A. T. S. Wee, T. Ouyang, K. P. Loh, X. Yu and H. O. Moser, *J. Phys. Chem. C*, 2008, **112**, 2487–2491.

[68] A. M. Panich, H.-M. Vieth, A. I. Shames, N. Froumin, E. Ôsawa and A. Yao, *J. Phys. Chem. C*, 2010, **114**, 774–782.

[69] O. Shenderova, A. M. Panich, S. Moseenkov, S. C. Hens, V. Kuznetsov and H.-M. Vieth, *J. Phys. Chem. C*, 2011, **115**, 19005–19011.

[70] Y. Ahmad, M. Dubois, K. Guérin, A. Hamwi, Z. Fawal, A. P. Kharitonov, A. V. Generalov, A. Y. Klyushin, K. A. Simonov, N. A. Vinogradov, I. A. Zhdanov, A. B. Preobrajenski and A. S. Vinogradov, *J. Phys. Chem. C*, 2013, **117**, 13564–13572.

[71] J. Yano and V. K. Yachandra, *Photosynth. Res.*, 2009, **102**, 241–254.

[72] P. R. Berman, *Introductory Quantum Mechanics: A Traditional Approach Emphasizing Connections with Classical Physics*, Springer International Publishing, Cham, 2018, pp. 607–629.

[73] A. Augustsson, A. Henningsson, S. M. Butorin, H. Siegbahn, J. Nordgren and J.-H. Guo, *J. Chem. Phys.*, 2003, **119**, 3983–3987.

[74] P. Glatzel and U. Bergmann, *Coord. Chem. Rev.*, 2005, **249**, 65–95.

[75] M. Bauer and C. Gastl, *Phys. Chem. Chem. Phys.*, 2010, **12**, 5575–5584.

[76] G. Vankó, A. Bordage, P. Glatzel, E. Gallo, M. Rovezzi, W. Gawelda, A. Galler, C. Bressler, G. Doumy, A. M. March, E. P. Kanter, L. Young, S. H. Southworth, S. E. Canton, J. Uhlig, G. Smolentsev, V. Sundström, K. Haldrup, T. B. van

Driel, M. M. Nielsen, K. S. Kjaer and H. T. Lemke, *J. Electron Spectros. Relat. Phenomena*, 2013, **188**, 166–171.

[77] L. J. P. Ament, M. van Veenendaal, T. P. Devereaux, J. P. Hill and J. van den Brink, *Rev. Mod. Phys.*, 2011, **83**, 705–767.

[78] J. Ren, L. Lin, K. Lieutenant, C. Schulz, D. Wong, T. Gimm, A. Bande, X. Wang and T. Petit, *Small Methods*, 2021, **5**, 2000707.

[79] C. S. Fadley, *J. Electron Spectros. Relat. Phenomena*, 2010, **178-179**, 2–32.

[80] M. I. Landstrass and K. V. Ravi, *Appl. Phys. Lett.*, 1989, **55**, 975–977.

[81] V. Chakrapani, J. C. Angus, A. B. Anderson, S. D. Wolter, B. R. Stoner and G. U. Sumanasekera, *Science*, 2007, **318**, 1424–1430.

[82] J. A. Garrido, S. Nowy, A. Härtl and M. Stutzmann, *Langmuir*, 2008, **24**, 3897–3904.

[83] J. A. Garrido, A. Härtl, M. Dankerl, A. Reitinger, M. Eickhoff, A. Helwig, G. Müller and M. Stutzmann, *J. Am. Chem. Soc.*, 2008, **130**, 4177–4181.

[84] T. Petit, J.-C. Arnault, H. A. Girard, M. Sennour, T.-Y. Kang, C.-L. Cheng and P. Bergonzo, *Nanoscale*, 2012, **4**, 6792–6799.

[85] T. Petit, H. A. Girard, A. Trouvé, I. Batonneau-Gener, P. Bergonzo and J.-C. Arnault, *Nanoscale*, 2013, **5**, 8958–8962.

[86] T. Petit, M. Pflüger, D. Tolksdorf, J. Xiao and E. F. Aziz, *Nanoscale*, 2015, **7**, 2987–2991.

[87] A. Bolker, C. Saguy and R. Kalish, *Nanotechnology*, 2014, **25**, 385702.

[88] K. Larsson and J. Ristein, *J. Phys. Chem. B*, 2005, **109**, 10304–10311.

[89] D. Petrini and K. Larsson, *J. Phys. Chem. B*, 2005, **109**, 22426–22431.

[90] H. X. Young, Y. Yu, L. F. Xu and C. Z. Gu, *J. Phys.: Conf. Ser.*, 2006, **29**, 145–149.

[91] J. Ristein, *Surf. Sci.*, 2006, **600**, 3677–3689.

[92] D. Petrini and K. Larsson, *J. Phys. Chem. C*, 2007, **111**, 13804–13812.

[93] O. Manelli, S. Corni and M. C. Righi, *J. Phys. Chem. C*, 2010, **114**, 7045–7053.

[94] Y. Takagi, K. Shiraishi, M. Kasu and H. Sato, *Surf. Sci.*, 2013, **609**, 203–206.

[95] M. M. Hassan and K. Larsson, *J. Phys. Chem. C*, 2014, **118**, 22995–23002.

[96] T. Kirschbaum, T. Petit, J. Dzubiella and A. Bande, *J. Comput. Chem.*, 2022, **43**, 923–929.

[97] W. Heisenberg, *Z. Phys.*, 1925, **33**, 879–893.

[98] M. Born, W. Heisenberg and P. Jordan, *Z. Phys.*, 1926, **35**, 557–615.

[99] E. Schrödinger, *Phys. Rev.*, 1926, **37**, 863.

[100] D. R. Hartree, *Math. Proc. Camb. Philos. Soc.*, 1928, **24**, 111–132.

[101] J. C. Slater, *Phys. Rev.*, 1928, **32**, 339–348.

[102] J. A. Gaunt, *Math. Proc. Camb. Philos. Soc.*, 1928, **24**, 328–342.

[103] J. C. Slater, *Phys. Rev.*, 1930, **35**, 210–211.

[104] V. Fock, *Z. Physik*, 1930, **61**, 126–148.

[105] J. C. Slater, *Phys. Rev.*, 1951, **81**, 385–390.

[106] J. C. Slater, *Phys. Rev.*, 1929, **34**, 1293–1322.

[107] A. Szabo and N. S. Ostlund, *Modern Quantum Chemistry : Introduction to Advanced Electronic Structure Theory*, Dover Publications, New York, 1996.

[108] C. Møller and M. S. Plesset, *Phys. Rev.*, 1934, **46**, 618–622.

[109] M. L. Leininger, W. D. Allen, H. F. Schaefer and C. D. Sherrill, *J. Chem. Phys.*, 2000, **112**, 9213–9222.

[110] J. Čížek, *J. Chem. Phys.*, 1966, **45**, 4256–4266.

[111] H. G. Kümmel, *Int. J. Mod. Phys. B*, 2003, **17**, 5311–5325.

[112] B. O. Roos and P. E. M. Siegbahn, *Int. J. Quantum Chem.*, 1980, **17**, 485–500.

[113] W. Kutzelnigg, *J. Mol. Struc. (Theochem)*, 1988, **181**, 33–54.

[114] A. Dreuw and M. Head-Gordon, *Chem. Rev.*, 2005, **105**, 4009–4037.

[115] V. Gupta, *Principles and Applications of Quantum Chemistry*, Elsevier, 2016, pp. 155–194.

[116] L. H. Thomas, *Math. Proc. Camb. Philos. Soc.*, 1927, **23**, 542–548.

[117] E. Fermi, *Z. Phys.*, 1928, **48**, 73–79.

[118] P. Hohenberg and W. Kohn, *Phys. Rev.*, 1964, **136**, B864–B871.

[119] W. Kohn and L. J. Sham, *Phys. Rev.*, 1965, **140**, A1133–A1138.

[120] J. P. Perdew and K. Schmidt, *AIP Conf. Proc.*, 2001, **577**, 1–20.

[121] V. Lutsker, *Range-Separated Hybrid Functionals in the Density Functional-Based Tight-Binding Method (PhD Thesis)*, Universität Regensburg, Germany, 2015.

[122] A. Schäfer, H. Horn and R. Ahlrichs, *J. Chem. Phys.*, 1992, **97**, 2571–2577.

[123] F. Weigend and R. Ahlrichs, *Phys. Chem. Chem. Phys.*, 2005, **7**, 3297–3305.

[124] F. Weigend, *Phys. Chem. Chem. Phys.*, 2006, **8**, 1057–1065.

[125] S. Grimme, *WIREs Comput. Mol. Sci.*, 2011, **1**, 211–228.

[126] S. Grimme, S. Ehrlich and L. Goerigk, *J. Comput. Chem.*, 2011, **32**, 1456–1465.

[127] P. Koskinen and V. Mäkinen, *Comput. Mater. Sci.*, 2009, **47**, 237–253.

[128] C. Bannwarth, S. Ehlert and S. Grimme, *J. Chem. Theory Comput.*, 2019, **15**, 1652–1671.

[129] B. Hourahine, B. Aradi, V. Blum, F. Bonafé, A. Buccheri, C. Camacho, C. Cevallos, M. Y. Deshaye, T. Dumitrică, A. Dominguez, S. Ehlert, M. Elstner, T. van der Heide, J. Hermann, S. Irle, J. J. Kranz, C. Köhler, T. Kowalczyk, T. Kubař, I. S. Lee, V. Lutsker, R. J. Maurer, S. K. Min, I. Mitchell, C. Negre, T. A. Niehaus, A. M. N. Niklasson, A. J. Page, A. Pecchia, G. Penazzi, M. P. Persson, J. Řezáč, C. G. Sánchez, M. Sternberg, M. Stöhr, F. Stuckenberg, A. Tkatchenko, V. W.-z. Yu and T. Frauenheim, *J. Chem. Phys.*, 2020, **152**, 124101.

[130] M. Roemelt and F. Neese, *J. Phys. Chem. A*, 2013, **117**, 3069–3083.

[131] V. Barone and M. Cossi, *J. Phys. Chem. A*, 1998, **102**, 1995–2001.

[132] A. B. Nassif, I. Shahin, I. Attili, M. Azzeh and K. Shaalan, *IEEE Access*, 2019, **7**, 19143–19165.

[133] J. Jumper, R. Evans, A. Pritzel, T. Green, M. Figurnov, O. Ronneberger, K. Tunyasuvunakool, R. Bates, A. Žídek, A. Potapenko, A. Bridgland, C. Meyer, S. A. A. Kohl, A. J. Ballard, A. Cowie, B. Romera-Paredes, S. Nikolov, R. Jain, J. Adler, T. Back, S. Petersen, D. Reiman, E. Clancy, M. Zielinski, M. Steinegger, M. Pacholska, T. Berghammer, S. Bodenstein, D. Silver, O. Vinyals, A. W. Senior, K. Kavukcuoglu, P. Kohli and D. Hassabis, *Nature*, 2021, **596**, 583–589.

[134] J. Hermann, Z. Schätzle and F. Noé, *Nat. Chem.*, 2020, **12**, 891–897.

[135] D. Pfau, J. S. Spencer, A. G. D. G. Matthews and W. M. C. Foulkes, *Phys. Rev. Res.*, 2020, **2**, 033429.

[136] J. S. Smith, B. Nebgen, N. Lubbers, O. Isayev and A. E. Roitberg, *J. Chem. Phys.*, 2018, **148**, 241733.

[137] V. Zaverkin, D. Holzmüller, I. Steinwart and J. Kästner, *Digital Discovery*, 2022, **1**, 605–620.

[138] J. Wang, S. Olsson, C. Wehmeyer, A. Pérez, N. E. Charron, G. de Fabritiis, F. Noé and C. Clementi, *ACS Cent. Sci.*, 2019, **5**, 755–767.

[139] B. E. Husic, N. E. Charron, D. Lemm, J. Wang, A. Pérez, M. Majewski, A. Krämer, Y. Chen, S. Olsson, G. de Fabritiis, F. Noé and C. Clementi, *J. Chem. Phys.*, 2020, **153**, 194101.

[140] R. Ramakrishnan, P. O. Dral, M. Rupp and O. A. von Lilienfeld, *J. Chem. Theory Comput.*, 2015, **11**, 2087–2096.

[141] P. O. Dral, *J. Phys. Chem. Lett.*, 2020, **11**, 2336–2347.

[142] F. Noé, A. Tkatchenko, K.-R. Müller and C. Clementi, *Annu. Rev. Phys. Chem.*, 2020, **71**, 361–390.

[143] J. Westermayr and P. Marquetand, *Chem. Rev.*, 2021, **121**, 9873–9926.

[144] A.-T. Ton, F. Gentile, M. Hsing, F. Ban and A. Cherkasov, *Mol. Inform.*, 2020, **39**, 2000028.

[145] C. Gorgulla, A. Jayaraj, K. Fackeldey and H. Arthanari, *Curr. Opin. Chem. Biol.*, 2022, **69**, 102156.

[146] P. Raccuglia, K. C. Elbert, P. D. F. Adler, C. Falk, M. B. Wenny, A. Mollo, M. Zeller, S. A. Friedler, J. Schrier and A. J. Norquist, *Nature*, 2016, **533**, 73–76.

[147] C. Wen, Y. Zhang, C. Wang, D. Xue, Y. Bai, S. Antonov, L. Dai, T. Lookman and Y. Su, *Acta Materialia*, 2019, **170**, 109–117.

[148] D. Lowe, *Virtual Screening for Coronavirus Protease Inhibitors: A Waste of Good Electrons?*, 2022, `https://www.science.org/content/blog-post/virtual-screening-coronavirus-protease-inhibitors-waste-good-electrons`.

[149] J. Behler and M. Parrinello, *Phys. Rev. Lett.*, 2007, **98**, 146401.

[150] W. Jia, H. Wang, M. Chen, D. Lu, L. Lin, R. Car, E. Weinan and L. Zhang, SC20: International Conference for High Performance Computing, Networking, Storage and Analysis, 2020, pp. 1–14.

[151] O. Wohlfahrt, C. Dellago and M. Sega, *J. Chem. Phys.*, 2020, **153**, 144710.

[152] L. Zhang, H. Wang, R. Car and W. E, *Phys. Rev. Lett.*, 2021, **126**, 236001.

[153] A. Reinhardt and B. Cheng, *Nat. Commun.*, 2021, **12**, 588.

[154] A. Mauri, V. Consonni, M. Pavan and R. Todeschini, *MATCH Commun. Math. Co.*, 2006, **56**, 237–248.

[155] D. Rogers and M. Hahn, *J. Chem. Inf. Model.*, 2010, **50**, 742–754.

[156] M. Rupp, A. Tkatchenko, K.-R. Müller and O. A. von Lilienfeld, *Phys. Rev. Lett.*, 2012, **108**, 058301.

[157] K. Hansen, F. Biegler, R. Ramakrishnan, W. Pronobis, O. A. von Lilienfeld, K.-R. Müller and A. Tkatchenko, *J. Phys. Chem. Lett.*, 2015, **6**, 2326–2331.

[158] F. A. Faber, L. Hutchison, B. Huang, J. Gilmer, S. S. Schoenholz, G. E. Dahl, O. Vinyals, S. Kearnes, P. F. Riley and O. A. von Lilienfeld, *J. Chem. Theory Comput.*, 2017, **13**, 5255–5264.

[159] A. P. Bartók, R. Kondor and G. Csányi, *Phys. Rev. B*, 2013, **87**, 184115.

[160] L. Zhu, M. Amsler, T. Fuhrer, B. Schaefer, S. Faraji, S. Rostami, S. A. Ghasemi, A. Sadeghi, M. Grauzinyte, C. Wolverton and S. Goedecker, *J. Chem. Phys.*, 2016, **144**, 034203.

[161] J. S. Smith, O. Isayev and A. E. Roitberg, *Chem. Sci.*, 2017, **8**, 3192–3203.

[162] F. A. Faber, A. S. Christensen, B. Huang and O. A. von Lilienfeld, *J. Chem. Phys.*, 2018, **148**, 241717.

[163] K. Kwac, H. Freedman and M. Cho, *J. Chem. Theory Comput.*, 2021, **17**, 6353–6365.

[164] J. Behler, *J. Chem. Phys.*, 2011, **134**, 074106.

[165] B. Parsaeifard, D. S. De, A. S. Christensen, F. A. Faber, E. Kocer, S. De, J. Behler, O. A. v. Lilienfeld and S. Goedecker, *Mach. Learn.: Sci. Technol.*, 2021, **2**, 015018.

[166] T. Kirschbaum, B. von Seggern, J. Dzubiella, A. Bande and F. Noé, *J. Chem. Theory Comput.*, 2023, **19**, 4461–4473.

[167] J. P. Darby, J. R. Kermode and G. Csányi, *npj Comput. Mater.*, 2022, **8**, 1–13.

[168] T. N. Kipf and M. Welling, *arXiv*, 2016, arXiv:1609.02907.

[169] J. Gilmer, S. S. Schoenholz, P. F. Riley, O. Vinyals and G. E. Dahl, *arXiv*, 2017, arXiv:1704.01212.

[170] K. Schütt, P.-J. Kindermans, H. E. Sauceda Felix, S. Chmiela, A. Tkatchenko and K.-R. Müller, Advances in Neural Information Processing Systems, 2017.

[171] K. T. Schütt, F. Arbabzadah, S. Chmiela, K. R. Müller and A. Tkatchenko, *Nat. Commun.*, 2017, **8**, 13890.

[172] N. Thomas, T. Smidt, S. Kearnes, L. Yang, L. Li, K. Kohlhoff and P. Riley, *arXiv*, 2018, arXiv:1802.08219.

[173] K. Schütt, O. Unke and M. Gastegger, Proceedings of the 38th International Conference on Machine Learning, 2021, pp. 9377–9388.

[174] B. K. Miller, M. Geiger, T. E. Smidt and F. Noé, *arXiv*, 2020, arXiv:2008.08461.

[175] S. Batzner, A. Musaelian, L. Sun, M. Geiger, J. P. Mailoa, M. Kornbluth, N. Molinari, T. E. Smidt and B. Kozinsky, *Nat. Commun.*, 2022, **13**, 2453.

[176] I. Batatia, D. P. Kovács, G. N. Simm, C. Ortner and G. Csányi, *arXiv*, 2022, arXiv:2206.07697.

[177] M. Geiger and T. Smidt, *arXiv*, 2022, arXiv:2207.09453.

[178] K. Cho, B. Van Merriënboer, D. Bahdanau and Y. Bengio, *arXiv*, 2014, arXiv:1409.1259.

[179] O. Vinyals, S. Bengio and M. Kudlur, *arXiv*, 2015, arXiv:1511.06391.

[180] K. T. Schütt, H. E. Sauceda, P.-J. Kindermans, A. Tkatchenko and K.-R. Müller, *J. Chem. Phys.*, 2018, **148**, 241722.

[181] K. T. Schütt, P. Kessel, M. Gastegger, K. A. Nicoli, A. Tkatchenko and K.-R. Müller, *J. Chem. Theory Comput.*, 2019, **15**, 448–455.

[182] Y. Wang, Z. Li and A. B. Farimani, *arXiv*, 2022, arXiv:2209.05582.

[183] A. Krüger, F. Kataoka, M. Ozawa, T. Fujino, Y. Suzuki, A. E. Aleksenskii, A. Y. Vul' and E. Ōsawa, *Carbon*, 2005, **43**, 1722–1730.

[184] V. N. Khabashesku, W. E. Billups and J. L. Margrave, *Acc. Chem. Res.*, 2002, **35**, 1087–1095.

[185] A. Krueger and D. Lang, *Adv. Funct. Mater.*, 2012, **22**, 890–906.

[186] S. Cui and E. L. Hu, *Appl. Phys. Lett.*, 2013, **103**, 051603.

[187] J. Havlik, H. Raabova, M. Gulka, V. Petrakova, M. Krecmarova, V. Masek, P. Lousa, J. Stursa, H.-G. Boyen, M. Nesladek and P. Cigler, *Adv. Funct. Mater.*, 2016, **26**, 4134–4142.

[188] A. Denisenko, A. Romanyuk, C. Pietzka, J. Scharpf and E. Kohn, *Diam. Relat. Mater.*, 2010, **19**, 423–427.

[189] N. B. Shustova, I. V. Kuvychko, R. D. Bolskar, K. Seppelt, S. H. Strauss, A. A. Popov and O. V. Boltalina, *J. Am. Chem. Soc.*, 2006, **128**, 15793–15798.

[190] T. Szilvási and A. Gali, *J. Phys. Chem. C*, 2014, **118**, 4410–4415.

[191] T. Brandenburg, T. Petit, A. Neubauer, K. Atak, M. Nagasaka, R. Golnak, N. Kosugi and E. F. Aziz, *Phys. Chem. Chem. Phys.*, 2015, **17**, 18337–18343.

[192] S. Ferro and A. De Battisti, *J. Phys. Chem. B*, 2003, **107**, 7567–7573.

[193] S. Ferro and A. De Battisti, *Anal. Chem.*, 2003, **75**, 7040–7042.

[194] T. Kondo, H. Ito, K. Kusakabe, K. Ohkawa, K. Honda, Y. Einaga, A. Fujishima and T. Kawai, *Diam. Relat. Mater.*, 2008, **17**, 48–54.

[195] K. J. Rietwyk, S. L. Wong, L. Cao, K. M. O'Donnell, L. Ley, A. T. S. Wee and C. I. Pakes, *Appl. Phys. Lett.*, 2013, **102**, 091604.

[196] T. Tasaki, Y. Guo, H. Machida, S. Akasaka and A. Fujimori, *Polym. Compos.*, 2019, **40**, E842–E855.

[197] M. Dubois, K. Guérin, J. P. Pinheiro, Z. Fawal, F. Masin and A. Hamwi, *Carbon*, 2004, **42**, 1931–1940.

[198] E. M. Zagrebina, A. V. Generalov, A. Y. Klyushin, K. A. Simonov, N. A. Vinogradov, M. Dubois, L. Frezet, N. Mårtensson, A. B. Preobrajenski and A. S. Vinogradov, *J. Phys. Chem. C*, 2015, **119**, 835–844.

[199] M. Herraiz, N. Batisse, M. Dubois, V. V. Nesvizhevsky, C. Cavallari, M. Brunelli, V. Pischedda and S. Radescu, *J. Phys. Chem. C*, 2020, **124**, 14229–14236.

[200] V. Y. Osipov, N. M. Romanov, K. Kogane, H. Touhara, Y. Hattori and K. Takai, *Mendeleev Commun.*, 2020, **30**, 84–87.

[201] F. Weber, J. Ren, T. Petit and A. Bande, *Phys. Chem. Chem. Phys.*, 2019, **21**, 6999–7008.

[202] P. Glans, R. E. L. Villa, Y. Luo, H. Agren and J. Nordgren, *J. Phys. B: At. Mol. Opt. Phys.*, 1994, **27**, 3399–3414.

[203] T. Brandenburg, M. Agåker, K. Atak, M. Pflüger, C. Schwanke, T. Petit, K. M. Lange, J.-E. Rubensson and E. F. Aziz, *Phys. Chem. Chem. Phys.*, 2014, **16**, 23379–23385.

[204] P. Han, D. Antonov, J. Wrachtrup and G. Bester, *Phys. Rev. B*, 2017, **95**, 195428.

[205] M. Shen, H. F. Schaefer, C. Liang, J. H. Lii, N. L. Allinger and P. v. R. Schleyer, *J. Am. Chem. Soc.*, 1992, **114**, 497–505.

[206] J. Tao, J. P. Perdew, V. N. Staroverov and G. E. Scuseria, *Phys. Rev. Lett.*, 2003, **91**, 146401.

[207] J. P. Perdew, A. Ruzsinszky, G. I. Csonka, L. A. Constantin and J. Sun, *Phys. Rev. Lett.*, 2009, **103**, 026403.

[208] F. Neese, F. Wennmohs, A. Hansen and U. Becker, *Chem. Phys.*, 2009, **356**, 98–109.

[209] J. Stöhr, *NEXAFS Spectroscopy*, Springer Verlag, Berlin, Heidelberg, 1992.

[210] D. Maganas, S. DeBeer and F. Neese, *J. Phys. Chem. A*, 2018, **122**, 1215–1227.

[211] A. D. Becke, *Phys. Rev. A*, 1988, **38**, 3098–3100.

[212] A. D. Becke, *J. Chem. Phys.*, 1993, **98**, 5648–5652.

[213] M. Roemelt, D. Maganas, S. DeBeer and F. Neese, *J. Chem. Phys.*, 2013, **138**, 204101.

[214] K. Ueda, Y. Shimizu, H. Chiba, M. Okunishi, K. Ohmori, Y. Sato, E. Shigemasa and N. Kosugi, *J. Electron Spectros. Relat. Phenomena*, 1996, **79**, 441–444.

[215] F. Neese, F. Wennmohs, U. Becker and C. Riplinger, *J. Chem. Phys.*, 2020, **152**, 224108.

[216] J. F. Morar, F. J. Himpsel, G. Hollinger, J. L. Jordon, G. Hughes and F. R. McFeely, *Phys. Rev. B*, 1986, **33**, 1346–1349.

[217] A. Laikhtman, I. Gouzman, A. Hoffman, G. Comtet, L. Hellner and G. Dujardin, *J. Appl. Phys.*, 1999, **86**, 4192–4198.

[218] Z. Shpilman, I. Gouzman, T. K. Minton, L. Shen, A. Stacey, J. Orwa, S. Prawer, B. C. C. Cowie and A. Hoffman, *Diam. Relat. Mater.*, 2014, **45**, 20–27.

[219] A. Laikhtman and A. Hoffman, *Surf. Sci.*, 2003, **522**, L1–L8.

[220] A. Hoffman, G. Comtet, L. Hellner, G. Dujardin and M. Petravic, *Appl. Phys. Lett.*, 1998, **73**, 1152–1154.

[221] K. C. Prince, R. Richter, M. de Simone, M. Alagia and M. Coreno, *J. Phys. Chem. A*, 2003, **107**, 1955–1963.

[222] T. Gimm, *Structure Determination of Doped Nano Carbons via X-Ray Absorption Spectroscopy (Master's Thesis)*, Freie Universität Berlin, Germany, 2020.

[223] Y. K. Chang, H. H. Hsieh, W. F. Pong, M.-H. Tsai, F. Z. Chien, P. K. Tseng, L. C. Chen, T. Y. Wang, K. H. Chen, D. M. Bhusari, J. R. Yang and S. T. Lin, *Phys. Rev. Lett.*, 1999, **82**, 5377–5380.

[224] Y. Takata, K. Edamatsu, T. Yokoyama, K. Seki, M. Tohnan, T. Okada and T. Ohta, *Jpn. J. Appl. Phys.*, 1989, **28**, L1282.

[225] M. M. García, I. Jiménez, L. Vázquez, C. Gómez-Aleixandre, J. M. Albella, O. Sánchez, L. J. Terminello and F. J. Himpsel, *Appl. Phys. Lett.*, 1998, **72**, 2105–2107.

[226] T. Hamilton, E. Z. Kurmaev, S. N. Shamin, P. Y. Detkov, S. I. Chukhaeva and A. Moewes, *Diam. Relat. Mater.*, 2007, **16**, 350–352.

[227] A. V. Okotrub, L. G. Bulusheva, I. S. Larionova, V. L. Kuznetsov and S. L. Molodtsov, *Diam. Relat. Mater.*, 2007, **16**, 2090–2092.

[228] Q. Yang, S. Yang, Y. S. Li, X. Lu and A. Hirose, *Diam. Relat. Mater.*, 2007, **16**, 730–734.

[229] X. Zhou, T.-K. Sham, Y. Wu, Y.-M. Chong, I. Bello, S.-T. Lee, F. Heigl, T. Regier and R. I. R. Blyth, *J. Am. Chem. Soc.*, 2007, **129**, 1476–1477.

[230] J. Zhou, X. Zhou, R. Li, X. Sun, Z. Ding, J. Cutler and T.-K. Sham, *Chem. Phys. Lett.*, 2009, **474**, 320–324.

[231] C. Z. Zhang, H. Niakan, L. Yang, Y. S. Li, Y. F. Hu and Q. Yang, *Surf. Coat. Technol.*, 2013, **237**, 248–254.

[232] N. D. Drummond, A. J. Williamson, R. J. Needs and G. Galli, *Phys. Rev. Lett.*, 2005, **95**, 096801.

[233] F. Plasser, M. Wormit and A. Dreuw, *J. Chem. Phys.*, 2014, **141**, 024106.

[234] R. J. Hamers, J. A. Bandy, D. Zhu and L. Zhang, *Faraday Discuss.*, 2014, **172**, 397–411.

[235] E. Brun, H. A. Girard, J.-C. Arnault, M. Mermoux and C. Sicard-Roselli, *Carbon*, 2020, **162**, 510–518.

[236] H. Shiomi, Y. Nishibayashi and N. Fujimori, *Jpn. J. Appl. Phys.*, 1991, **30**, 1363.

[237] T. Petit, L. Puskar, T. Dolenko, S. Choudhury, E. Ritter, S. Burikov, K. Laptinskiy, Q. Brzustowski, U. Schade, H. Yuzawa, M. Nagasaka, N. Kosugi, M. Kurzyp, A. Venerosy, H. Girard, J.-C. Arnault, E. Osawa, N. Nunn, O. Shenderova and E. F. Aziz, *J. Phys. Chem. C*, 2017, **121**, 5185–5194.

[238] J. H. T. Luong, K. B. Male and J. D. Glennon, *Analyst*, 2009, **134**, 1965–1979.

[239] J. Bechter, C. Pietzka, C. Petkov, P. Reintanz, U. Siemeling, C. Popov and A. Pasquarelli, *Phys. Status Solidi A*, 2014, **211**, 2333–2338.

[240] A. S. Barnard, *J. Mater. Chem.*, 2008, **18**, 4038–4041.

[241] S. L. Y. Chang, P. Reineck, D. Williams, G. Bryant, G. Opletal, S. A. El-Demrdash, P.-L. Chiu, E. Ōsawa, A. S. Barnard and C. Dwyer, *Nanoscale*, 2020, **12**, 5363–5367.

[242] J. Hernández-Rojas and F. Calvo, *Front. Chem.*, 2019, **7**, 573.

[243] T. M. Willey, C. Bostedt, T. van Buuren, J. E. Dahl, S. G. Liu, R. M. K. Carlson, R. W. Meulenberg, E. J. Nelson and L. J. Terminello, *Phys. Rev. B*, 2006, **74**, 205432.

[244] L. Landt, K. Klunder, J. E. Dahl, R. M. K. Carlson, T. Moller and C. Bostedt, *Phys. Rev. Lett.*, 2009, 4.

[245] M. Vörös and A. Gali, *Phys. Rev. B*, 2009, **80**, 161411.

[246] J. P. Perdew, K. Burke and M. Ernzerhof, *Phys. Rev. Lett.*, 1996, **77**, 3865–3868.

[247] Y. Zhang and W. Yang, *Phys. Rev. Lett.*, 1998, **80**, 890–890.

[248] M. J. Gillan, D. Alfè and A. Michaelides, *J. Chem. Phys.*, 2016, **144**, 130901.

[249] J. P. Perdew, S. Kurth, A. Zupan and P. Blaha, *Phys. Rev. Lett.*, 1999, **82**, 2544–2547.

[250] J. P. Perdew, J. Tao, V. N. Staroverov and G. E. Scuseria, *J. Chem. Phys.*, 2004, **120**, 6898–6911.

[251] S. Grimme and A. Hansen, *Angew. Chem. Int. Ed.*, 2015, **54**, 12308–12313.

[252] F. L. Hirshfeld, *Theoret. Chim. Acta*, 1977, **44**, 129–138.

[253] P. Löwdin, *J. Chem. Phys.*, 1950, **18**, 365–375.

[254] T. Yanai, D. P. Tew and N. C. Handy, *Chem. Phys. Lett.*, 2004, **393**, 51–57.

[255] S. Klinkusch and J. C. Tremblay, *J. Chem. Phys.*, 2016, **144**, 184108.

[256] S. Kümmel, *Adv. Energy Mater.*, 2017, **7**, 1700440.

[257] F. Weber, J. C. Tremblay and A. Bande, *J. Phys. Chem. C*, 2020, **124**, 26688–26698.

[258] P. Han and G. Bester, *New J. Phys.*, 2016, **18**, 113052.

[259] T. Lu and F. Chen, *J. Comput. Chem.*, 2012, **33**, 580–592.

[260] A. S. Barnard and M. Sternberg, *J. Mater. Chem.*, 2007, **17**, 4811–4819.

[261] D. Petrini and K. Larsson, *J. Phys. Chem. C*, 2008, **112**, 3018–3026.

[262] M. De La Pierre, M. Bruno, C. Manfredotti, F. Nestola, M. Prencipe and C. Manfredotti, *Mol. Phys.*, 2014, **112**, 1030–1039.

[263] A. J. Bard and L. R. Faulkner, *Electrochemical Methods. Fundamentals and Applications*, John Wiley & Sons, New York, 3rd edn, 2001.

[264] A. J. Bard, R. Parsons and J. Jordan, *Standard Potentials in Aqueous Solution*, CRC Press, New York, Basel, 1985.

[265] K. F. Nakken and A. Pihl, *Radiat. Res.*, 1965, **26**, 519–526.

[266] E. J. Hart and J. W. Boag, *J. Am. Chem. Soc.*, 1962, **84**, 4090–4095.

[267] R. L. Martin, *J. Chem. Phys.*, 2003, **118**, 4775–4777.

[268] R. N. Barnett, U. Landman, C. L. Cleveland and J. Jortner, *Phys. Rev. Lett.*, 1987, **59**, 811–814.

[269] R. N. Barnett, U. Landman, D. Scharf and J. Jortner, *Acc. Chem. Res.*, 1989, **22**, 350–357.

[270] L. Turi and P. J. Rossky, *Chem. Rev.*, 2012, **112**, 5641–5674.

[271] L. Lai and A. S. Barnard, *J. Mater. Chem.*, 2012, **22**, 16774–16780.

[272] C. A. Feigl, B. Motevalli, A. J. Parker, B. Sun and A. S. Barnard, *Nanoscale Horiz.*, 2019, **4**, 983–990.

[273] M. A. Pinault, J. Barjon, T. Kociniewski, F. Jomard and J. Chevallier, *Physica B Condens. Matter*, 2007, **401-402**, 51–56.

[274] O. A. Williams, M. Nesladek, M. Daenen, S. Michaelson, A. Hoffman, E. Osawa, K. Haenen and R. B. Jackman, *Diam. Relat. Mater.*, 2008, **17**, 1080–1088.

[275] M. Wang, N. Simon, C. Decorse-Pascanut, M. Bouttemy, A. Etcheberry, M. Li, R. Boukherroub and S. Szunerits, *Electrochim. Acta*, 2009, **54**, 5818–5824.

[276] N. Brown and O. Hod, *J. Phys. Chem. C*, 2014, **118**, 5530–5537.

[277] K. Larsson and Y. Tian, *Carbon*, 2018, **134**, 244–254.

[278] K. G. Mikheev, T. N. Mogileva, A. E. Fateev, N. A. Nunn, O. A. Shenderova and G. M. Mikheev, *Appl. Sci.*, 2020, **10**, 3329.

[279] K. D. Behler, A. Stravato, V. Mochalin, G. Korneva, G. Yushin and Y. Gogotsi, *ACS Nano*, 2009, **3**, 363–369.

[280] H. Etemadi, R. Yegani and V. Babaeipour, *J. Appl. Polym. Sci.*, 2017, **134**, 44873.

[281] M. D. Petit-Domínguez, C. Quintana, L. Vázquez, M. del Pozo, I. Cuadrado, A. M. Parra-Alfambra and E. Casero, *Microchim. Acta*, 2018, **185**, 1–10.

[282] W. M. C. Foulkes and R. Haydock, *Phys. Rev. B*, 1989, **39**, 12520.

[283] Z. Li, N. Omidvar, W. S. Chin, E. Robb, A. Morris, L. Achenie and H. Xin, *J. Phys. Chem. A*, 2018, **122**, 4571–4578.

[284] M.-H. Lee, *Adv. Energy Mater.*, 2019, **9**, 1900891.

[285] D. Padula, J. D. Simpson and A. Troisi, *Mater. Horizons*, 2019, **6**, 343–349.

[286] M.-H. Lee, *Adv. Intell. Syst.*, 2020, **2**, 1900108.

[287] N. Meftahi, M. Klymenko, A. J. Christofferson, U. Bach, D. A. Winkler and S. P. Russo, *npj Comput. Mater.*, 2020, **6**, 1–8.

[288] M.-H. Lee, *Solar Energy*, 2022, **234**, 360–367.

[289] Q. Zhang, Y. J. Zheng, W. Sun, Z. Ou, O. Odunmbaku, M. Li, S. Chen, Y. Zhou, J. Li, B. Qin and K. Sun, *Adv. Sci.*, 2022, **9**, 2104742.

[290] F. E. Storm, L. M. Folkmann, T. Hansen and K. V. Mikkelsen, *J. Mol. Model.*, 2022, **28**, 313.

[291] F. Pereira, K. Xiao, D. A. R. S. Latino, C. Wu, Q. Zhang and J. Aires-de Sousa, *J. Chem. Inf. Model.*, 2017, **57**, 11–21.

[292] A. M. Chang, J. G. Freeze and V. S. Batista, *Chem. Sci.*, 2019, **10**, 6844–6854.

[293] B. Olsthoorn, R. M. Geilhufe, S. S. Borysov and A. V. Balatsky, *Adv. Quantum Technol.*, 2019, **2**, 1900023.

[294] O. Rahaman and A. Gagliardi, *J. Chem. Inf. Model.*, 2020, **60**, 5971–5983.

[295] K. L. Woon, Z. X. Chong, A. Ariffin and C. S. Chan, *J. Mol. Graph. Model.*, 2021, **105**, 107891.

[296] Z.-R. Ye, S.-H. Hung, B. Chen and M.-K. Tsai, *ACS Eng. Au*, 2022, **2**, 360–368.

[297] B. Mazouin, A. A. Schöpfer and O. A. v. Lilienfeld, *Mater. Adv.*, 2022, 8306–8316.

[298] C. Duan, S. Chen, M. G. Taylor, F. Liu and H. J. Kulik, *Chem. Sci.*, 2021, **12**, 13021–13036.

[299] K. T. Schütt, M. Gastegger, A. Tkatchenko, K.-R. Müller and R. J. Maurer, *Nat. Commun.*, 2019, **10**, 5024.

[300] O. Unke, M. Bogojeski, M. Gastegger, M. Geiger, T. Smidt and K.-R. Müller, Advances in Neural Information Processing Systems, 2021, pp. 14434–14447.

[301] L. C. Blum and J.-L. Reymond, *J. Am. Chem. Soc.*, 2009, **131**, 8732–8733.

[302] L. Ruddigkeit, R. van Deursen, L. C. Blum and J.-L. Reymond, *J. Chem. Inf. Model.*, 2012, **52**, 2864–2875.

[303] G. Montavon, M. Rupp, V. Gobre, A. Vazquez-Mayagoitia, K. Hansen, A. Tkatchenko, K.-R. Müller and O. Anatole von Lilienfeld, *New J. Phys.*, 2013, **15**, 095003.

[304] R. Ramakrishnan, P. O. Dral, M. Rupp and O. A. von Lilienfeld, *Sci. Data*, 2014, **1**, 140022.

[305] C. Draxl and M. Scheffler, *J. Phys. Mater.*, 2019, **2**, 036001.

[306] A. Stuke, C. Kunkel, D. Golze, M. Todorović, J. T. Margraf, K. Reuter, P. Rinke and H. Oberhofer, *Sci. Data*, 2020, **7**, 58.

[307] M. Fernandez, A. Bilić and A. S. Barnard, *Nanotechnology*, 2017, **28**, 38LT03.

[308] B. Sun, M. Fernandez and A. S. Barnard, *J. Chem. Inf. Model.*, 2017, **57**, 2413–2423.

[309] A. S. Barnard and G. Opletal, *Nanoscale*, 2019, **11**, 23165–23172.

[310] A. S. Barnard, G. Opletal and S. L. Y. Chang, *J. Phys. Chem. C*, 2019, **123**, 11207–11215.

[311] I. Furxhi, F. Murphy, M. Mullins and C. A. Poland, *Toxicol. Lett.*, 2019, **312**, 157–166.

[312] A. J. Parker and A. S. Barnard, *Nanoscale Horiz.*, 2020, **5**, 1394–1399.

[313] C. A. Daly and R. Hernandez, *J. Phys. Chem. C*, 2020, **124**, 13409–13420.

[314] C. Bannwarth, E. Caldeweyher, S. Ehlert, A. Hansen, P. Pracht, J. Seibert, S. Spicher and S. Grimme, *WIREs Comput. Mol. Sci.*, 2021, **11**, e1493.

[315] C. Adamo and V. Barone, *J. Chem. Phys.*, 1999, **110**, 6158–6170.

[316] J. P. Perdew, M. Ernzerhof and K. Burke, *J. Chem. Phys.*, 1996, **105**, 9982–9985.

[317] O. T. Unke, S. Chmiela, H. E. Sauceda, M. Gastegger, I. Poltavsky, K. T. Schütt, A. Tkatchenko and K.-R. Müller, *Chem. Rev.*, 2021, **121**, 10142–10186.

[318] J. Klicpera, J. Groß and S. Günnemann, *arXiv*, 2020, arXiv:2003.03123.

[319] J. Klicpera, S. Giri, J. T. Margraf and S. Günnemann, *arXiv*, 2020, arXiv:2011.14115.

[320] B. von Seggern, *Maschinelles Lernen von Moleküleigenschaften mit Graph Neural Networks und SOAP Fingerprints (Bachelor's Thesis)*, Freie Universität Berlin, Germany, 2022.

[321] H. Abdi and L. J. Williams, *WIREs Comput. Stat.*, 2010, **2**, 433–459.

[322] B. Casier, S. Carniato, T. Miteva, N. Capron and N. Sisourat, *J. Chem. Phys.*, 2020, **152**, 234103.

[323] F. Musil, M. Veit, A. Goscinski, G. Fraux, M. J. Willatt, M. Stricker, T. Junge and M. Ceriotti, *J. Chem. Phys.*, 2021, **154**, 114109.

[324] F. Pedregosa, G. Varoquaux, A. Gramfort, V. Michel, B. Thirion, O. Grisel, M. Blondel, P. Prettenhofer, R. Weiss, V. Dubourg, J. Vanderplas, A. Passos, D. Cournapeau, M. Brucher, M. Perrot and E. Duchesnay, *J. Mach. Learn. Res.*, 2011, **12**, 2825–2830.

[325] A. Paszke, S. Gross, F. Massa, A. Lerer, J. Bradbury, G. Chanan, T. Killeen, Z. Lin, N. Gimelshein, L. Antiga, A. Desmaison, A. Köpf, E. Z. Yang, Z. DeVito, M. Raison, A. Tejani, S. Chilamkurthy, B. Steiner, L. Fang, J. Bai and S. Chintala, *arXiv*, 2019, arXiv:1912.01703.

[326] M. Fey and J. E. Lenssen, ICLR Workshop on Representation Learning on Graphs and Manifolds, 2019.

[327] L. Himanen, M. O. J. Jäger, E. V. Morooka, F. Federici Canova, Y. S. Ranawat, D. Z. Gao, P. Rinke and A. S. Foster, *Comput. Phys. Commun.*, 2020, **247**, 106949.

[328] A. H. Larsen, J. J. Mortensen, J. Blomqvist, I. E. Castelli, R. Christensen, M. Dułak, J. Friis, M. N. Groves, B. Hammer, C. Hargus, E. D. Hermes, P. C. Jennings, P. B. Jensen, J. Kermode, J. R. Kitchin, E. L. Kolsbjerg, J. Kubal, K. Kaasbjerg, S. Lysgaard, J. B. Maronsson, T. Maxson, T. Olsen, L. Pastewka, A. Peterson, C. Rostgaard, J. Schiøtz, O. Schütt, M. Strange, K. S. Thygesen, T. Vegge, L. Vilhelmsen, M. Walter, Z. Zeng and K. W. Jacobsen, *J. Phys. Condens. Mat.*, 2017, **29**, 273002.

[329] S. A. Kajihara, A. Antonelli, J. Bernholc and R. Car, *Phys. Rev. Lett.*, 1991, **66**, 2010–2013.

[330] Y.-x. Cui, J.-g. Zhang, F.-h. Sun and Z.-m. Zhang, *Transactions of Nonferrous Metals Society of China*, 2013, **23**, 2962–2970.

[331] X. Wang, Y. Qiao, B. Zhang and F. Sun, *Diam. Relat. Mater.*, 2020, **109**, 108014.

[332] X. Wei, L. Chen, M. Zhang, Z. Lu and G. Zhang, *Diam. Relat. Mater.*, 2020, **110**, 108102.

[333] T. A. Grotjohn, D. T. Tran, M. K. Yaran, S. N. Demlow and T. Schuelke, *Diam. Relat. Mater.*, 2014, **44**, 129–133.

[334] H. Kato, D. Takeuchi, M. Ogura, T. Yamada, M. Kataoka, Y. Kimura, S. Sobue, C. E. Nebel and S. Yamasaki, *Diam. Relat. Mater.*, 2016, **63**, 165–168.

[335] G. Alfieri, L. Kranz and A. Mihaila, *Phys. Status Solidi Rapid Res. Lett.*, 2018, **12**, 1700409.

[336] M. Yaghoobi and M. Alaei, *Comp. Mater. Sci.*, 2022, **207**, 111284.

[337] A. Bolker, C. Saguy, M. Tordjman and R. Kalish, *Phys. Rev. B*, 2013, **88**, 035442.

[338] H. Groult, D. Devilliers, C. Hinnen and P. Marcus, *J. Fluor. Chem.*, 1992, **58**, 284.

[339] Y. Ma, H. Yang, J. Guo, C. Sathe, A. Agui and J. Nordgren, *Appl. Phys. Lett.*, 1998, **72**, 3353–3355.

[340] F. Neese, *J. Biol. Inorg. Chem.*, 2006, **11**, 702–711.

[341] S. DeBeer George, T. Petrenko and F. Neese, *Inorg. Chim. Acta*, 2008, **361**, 965–972.

[342] N. A. Besley, M. J. G. Peach and D. J. Tozer, *Phys. Chem. Chem. Phys.*, 2009, **11**, 10350–10358.

[343] N. A. Besley and F. A. Asmuruf, *Phys. Chem. Chem. Phys.*, 2010, **12**, 12024–12039.

[344] G. Schaftenaar and J. Noordik, *J. Comput. Aided Mol. Des.*, 2000, **14**, 123–134.

[345] H. Yin, Y. Ma, X. Hao, J. Mu, C. Liu and Z. Yi, *J. Chem. Phys.*, 2014, **140**, 214315.

[346] T. Demján, M. Vörös, M. Palummo and A. Gali, *J. Chem. Phys.*, 2014, **141**, 064308.

[347] B. Adhikari and M. Fyta, *Nanotechnology*, 2014, **26**, 035701.

[348] T. Sasagawa and Z.-X. Shen, *J. Appl. Phys.*, 2008, **104**, 073704.

[349] D. López-Carballeira and T. Polcar, *Diam. Relat. Mater.*, 2020, **108**, 107959.

[350] J. J. P. Stewart, *J. Mol. Model.*, 2013, **19**, 1–32.

[351] M. Frisch, G. Trucks, H. Schlegel, G. Scuseria, M. Robb, J. Cheeseman, G. Scalmani, V. Barone, G. Petersson, H. Nakatsuji *et al.*, *Gaussian 16, revision C. 01*, 2016.

[352] J. L. Teunissen, F. De Proft and F. De Vleeschouwer, *J. Chem. Theory Comput.*, 2017, **13**, 1351–1365.

[353] M. A. Caro, *Phys. Rev. B*, 2019, **100**, 024112.

[354] D. A. Ross, J. Lim, R.-S. Lin and M.-H. Yang, *Int. J. Comput. Vis.*, 2008, **77**, 125–141.